

Incipient Motion Under Shallow Flow Conditions

by

Paul M. Kanellopoulos

Thesis submitted to the Faculty of the
Virginia Polytechnic Institute and State University
in partial fulfillment of the requirements for the degree of
MASTER OF SCIENCE
in
Civil Engineering

Dr. Panayiotis Diplas, Chairman
Dr. Clinton Dancey
Dr. G.V. Loganathan

December, 1998
Blacksburg, Virginia

Keywords: Mountain Rivers, Shallow Flows, Surface Waves, Relative Depth, Threshold
Conditions, Probability of Entrainment, Rough Walls

INCIPIENT MOTION UNDER SHALLOW FLOW CONDITIONS

Paul M. Kanellopoulos

Committee Chairman: Dr. Panayiotis Diplas
Department of Civil and Environmental Engineering

(ABSTRACT)

Laboratory experiments were conducted to investigate the effect of low relative depth and high Froude number on the dimensionless critical shear stress (Shields parameter). Spherical particles of four different densities and an 8mm diameter were used as movable test material. The relative depth ranged from 2 to 12 and the Froude number ranged from 0.36 to 1.29. The results show that the traditional Shields diagram cannot be used to predict the incipient motion of coarse sediment particles when the relative depth is below 10 and the Froude number is above 0.5, approximately. Experiments using glass balls, whose density is almost identical to that of natural gravel, show that the Shields parameter can be twice as large in shallow flows than in deep flows. The results also show that the Shields parameter is dependent on the density of the particles. Data obtained from other studies support the findings of the present work. These findings can result in significant cost savings for riprap.

Additionally, velocity profiles using a laser-Doppler velocimeter (LDV) were taken for the glass ball incipient motion experiments. The purpose of this was to study possible changes in the velocity distribution with decreasing relative depth and increasing Froude number. The results show that the von Karman and integral constants in the law of the wall do not change in the range of relative depths and Froude numbers tested.

Acknowledgements

I would like to thank all the individuals who have assisted me in making this thesis possible.

I am very grateful to my advisor, Dr. Panayiotis Diplas, for all his support at every stage of this thesis and for the opportunity to work with him. I also wish to thank Dr. Clinton Dancey for all the help he provided with the LDV setup, operation, and data analysis and for reviewing this thesis. I am thankful to Dr. G.V Loganathan for reviewing this thesis.

I am very thankful to my mother for her support and encouragement.

I thank Dr. Athanasios Papanicolaou and Dr. Mahalingam Balakrishnan for their advice at the early stages of this thesis.

I thank Mike O'Connor for his help in setting up the LDV.

I thank Dr. Brian Kleiner for providing the movie camera.

Finally, I wish to acknowledge the financial support provided by the National Science Foundation.

Table of Contents

Abstract	ii
Acknowledgements	iii
Table of Contents	iv
List of Figures	vi
List of Tables	xiii
List of Symbols	xvii
Chapter 1:	
Introduction	1
1.1 Brief Definition of Incipient Motion	1
1.2 Threshold Conditions in Mild Sloped Channels	1
1.3 Introduction to Free Surface Effects on Incipient Motion	2
1.4 Analogy to a Submarine Moving Near the Surface of the Ocean	2
1.5 Flow Resistance Equations for Large-scale Roughness	3
1.6 The Influence of the Relative Depth on Incipient Motion	3
1.7 Focus of this Study	4
Chapter 2:	
Literature Review	6
2.1 Initiation of Motion in Steep Channels with Shallow Flows	6
2.1.1 Dimensionless Critical Shear Stress as a Function of Relative Depth	6
2.1.2 Dimensionless Critical Shear Stress as a Function of Froude Number	11
2.2 Velocity Profiles	14
2.2.1 Velocity Distribution in Smooth and Rough Walls	14
2.2.2 Selection of the Roughness Length (k_s) and Datum	16
2.2.3 Velocity Profiles in Steep Channels with High Froude Numbers	17
Chapter 3:	
Equipment	24
3.1 Flume	24
3.2 Spherical Particles	25
3.3 Movie Camera	25
3.4 Plexiglass Lid	26
3.5 The LDV System	26

Chapter 4:	
Methodology	32
4.1 Dimensional Analysis	32
4.2 Criterion for Incipient Motion	32
4.2.1 The Concept of Probability of Entrainment in a Bursting Period	32
4.2.2 Selection of a Critical Probability of Entrainment	34
4.2.3 The Trial-and-Error Procedure	35
4.3 Experimental Setup	36
4.4 Experimental Procedure	37
4.4.1 Running Experiments at Threshold Conditions	37
4.4.2 Velocity Profiles	38
Chapter 5:	
Results and Analysis of Experiments	42
5.1 Summary Tables	42
5.2 Analysis of Results	43
5.2.1 The Modified Shields Diagram	43
5.2.2 Threshold Conditions without Considering the Bursting Period	45
5.2.3 Threshold Conditions with M1 Water Surface Profiles	46
5.2.4 Sensitivity Analysis	46
5.3 Final Remarks	47
Chapter 6:	
Velocity Profiles	64
6.1 Introduction	64
6.2 Velocity Profile Plotting Procedure	65
6.3 Results (Velocity Profiles for Free Surface Flows)	66
6.4 Results (Velocity Profiles for Pressurized Flows)	67
Chapter 7:	
Conclusion	76
References	77
Appendix 1	83
Appendix 2	118
Vita	151

List of Figures

Figure 1.1	The forces acting on a non-cohesive spherical particle in the presence of moving fluid.	5
Figure 2.1	Plot of the dimensionless critical shear stress vs. relative depth using data from several previous investigators.	22
Figure 2.2	Plot of the dimensionless critical shear stress vs. Froude number using data from several previous investigators.	23
Figure 3.1	Schematic of the flume.	29
Figure 3.2	The filming process.	30
Figure 3.3	The lid structure (sketch).	31
Figure 4.1	The 2% packing condition. Test particles on top of the well-packed, 4-layer bed (sketch).	40
Figure 4.2	The test section (sketch).	41
Figure 5.1	Plot of the dimensionless critical shear stress vs. densimetric Froude number and relative depth (modified Shields diagram) for the viton ball data.	54
Figure 5.2	Plot of the dimensionless critical shear stress vs. densimetric Froude number and relative depth (modified Shields diagram) for the teflon ball data.	55
Figure 5.3	Plot of the dimensionless critical shear stress vs. densimetric Froude number and relative depth (modified Shields diagram) for the glass ball data.	56
Figure 5.4	Plot of the dimensionless critical shear stress vs. densimetric Froude number and relative depth (modified Shields diagram) for the ceramic ball data.	57
Figure 5.5	Plot of the dimensionless critical shear stress vs. densimetric Froude number for the 4 particle densities.	58
Figure 5.6	Plot of the dimensionless critical shear stress vs. Froude number for the 4 particle densities.	59
Figure 5.7	Plot of the dimensionless critical shear stress vs. relative depth for the 4 particle densities.	60

Figure 5.8	Plot of the dimensionless critical shear stress vs. densimetric Froude number for the whole range of relative depths ($H/D_{50} = 2-12$).	61
Figure 5.9	Plot of the dimensionless critical shear stress vs. Froude number for the whole range of relative depths ($H/D_{50} = 2-12$).	62
Figure 5.10	The modified Shields diagram for the glass ball experiments when considering the bursting period vs. not considering the bursting period in the criterion for incipient conditions.	63
Figure 6.1a	Velocity profile for experiment F3 ($H/D_{50} = 7$ and $S = 0.135\%$). The datum is at the top of the balls in the channel bed.	72
Figure 6.1b	Logarithmic velocity profile for experiment F3 ($H/D_{50} = 7$ and $S = 0.135\%$) split into two regions. The datum is at the top of the balls in the channel bed.	72
Figure 6.1c	Logarithmic velocity profile for experiment F3 ($H/D_{50} = 7$ and $S = 0.135\%$) split into two regions. The datum is 3.5 mm (0.4375k) below the top of the balls in the channel bed.	73
Figure 6.1d	Logarithmic velocity profile for experiment F3 ($H/D_{50} = 7$ and $S = 0.135\%$): single region. The datum is at the top of the balls in the channel bed.	73
Figure 6.1e	Logarithmic velocity profile for experiment F3 ($H/D_{50} = 7$ and $S = 0.135\%$): single region. The datum is 1 mm below the top of the balls in the bed.	74
Figure 6.2	Velocity profile comparison of $H/D_{50} = 5$ (free surface) vs. 5 pressurized flows with a relative depth range of 3-8.5.	75
Figure A.1a	Velocity profile for experiment C3 ($H/D_{50} = 4$ and $S = 0.28\%$). The datum is at the top of the balls in the channel bed.	123
Figure A.1b	Logarithmic velocity profile for experiment C3 ($H/D_{50} = 4$ and $S = 0.28\%$) split into two regions. The datum is at the top of the balls in the channel bed.	123
Figure A.1c	Logarithmic velocity profile for experiment C3 ($H/D_{50} = 4$ and $S = 0.28\%$): single region. The datum is at the top of the balls in the channel bed.	124
Figure A.1d	Logarithmic velocity profile for experiment C3 ($H/D_{50} = 4$ and $S = 0.28\%$): single region. The datum is 1 mm below the top of the balls in the bed.	124

Figure A.2a	Velocity profile for $H/D_{50} = 4$ (Supercritical flow, $S = 1\%$). The datum is at the top of the balls in the channel bed.	125
Figure A.2b	Logarithmic velocity profile for $H/D_{50} = 4$ (Supercritical flow, $S = 1\%$) split into two regions. The datum is at the top of the balls in the channel bed.	125
Figure A.2c	Logarithmic velocity profile for $H/D_{50} = 4$ (Supercritical flow, $S = 1\%$): single region. The datum is at the top of the balls in the channel bed.	126
Figure A.2d	Logarithmic velocity profile for experiment $H/D_{50} = 4$ (Supercritical flow, $S = 1\%$): single region. The datum is 1mm below the top of the balls in the bed.	126
Figure A.3a	Velocity profile for experiment D3 ($H/D_{50} = 5$ and $S = 0.21\%$). The datum is at the top of the balls in the channel bed.	127
Figure A.3b	Logarithmic velocity profile for experiment D3 ($H/D_{50} = 5$ and $S = 0.21\%$) split into two regions. The datum is at the top of the balls in the channel bed.	127
Figure A.3c	Logarithmic velocity profile for experiment D3 ($H/D_{50} = 5$ and $S = 0.21\%$): single region. The datum is at the top of the balls in the channel bed.	128
Figure A.3d	Logarithmic velocity profile for experiment D3 ($H/D_{50} = 5$ and $S = 0.21\%$): single region. The datum is 1 mm below the top of the balls in the bed.	128
Figure A.4a	Velocity profile for experiment E3 ($H/D_{50} = 6$ and $S = 0.165\%$). The datum is at the top of the balls in the channel bed.	129
Figure A.4b	Logarithmic velocity profile for experiment E3 ($H/D_{50} = 6$ and $S = 0.165\%$) split into two regions. The datum is at the top of the balls in the bed.	129
Figure A.4c	Logarithmic velocity profile for experiment E3 ($H/D_{50} = 6$ and $S = 0.165\%$): single region. The datum is at the top of the balls in the channel bed.	130
Figure A.4d	Logarithmic velocity profile for experiment E3 ($H/D_{50} = 6$ and $S = 0.165\%$): single region. The datum is 1 mm below the top of the balls in the bed.	130

Figure A.5a	Velocity profile for $H/D_{50} = 6$ (Supercritical flow, $S = 0.85\%$). The datum is at the top of the balls in the channel bed.	131
Figure A.5b	Logarithmic velocity profile for $H/D_{50} = 6$ (Supercritical flow, $S = 0.85\%$) split into two regions. The datum is at the top of the balls in the channel bed.	131
Figure A.5c	Logarithmic velocity profile for experiment $H/D_{50} = 6$ (Supercritical flow, $S = 0.85\%$) : single region. The datum is at the top of the balls in the bed.	132
Figure A.5d	Logarithmic velocity profile for experiment $H/D_{50} = 6$ (Supercritical flow, $S = 0.85\%$) : single region. The datum is 1 mm below the top of the balls in the channel bed.	132
Figure A.6a	Velocity profile for experiment F3 ($H/D_{50} = 7$ and $S = 0.135\%$). The datum is at the top of the balls in the channel bed.	133
Figure A.6b	Logarithmic velocity profile for experiment F3 ($H/D_{50} = 7$ and $S = 0.135\%$) split into two regions. The datum is at the top of the balls in the channel bed.	133
Figure A.6c	Logarithmic velocity profile for experiment F3 ($H/D_{50} = 7$ and $S = 0.135\%$) : single region. The datum is at the top of the balls in the channel bed.	134
Figure A.6d	Logarithmic velocity profile for experiment F3 ($H/D_{50} = 7$ and $S = 0.135\%$) : single region. The datum is 1 mm below the top of the balls in the bed.	134
Figure A.7a	Velocity profile for experiment G3 ($H/D_{50} = 8$ and $S = 0.115\%$). The datum is at the top of the balls in the channel bed.	135
Figure A.7b	Logarithmic velocity profile for experiment G3 ($H/D_{50} = 8$ and $S = 0.115\%$) split into two regions. The datum is at the top of the balls in the channel bed.	135
Figure A.7c	Logarithmic velocity profile for experiment G3 ($H/D_{50} = 8$ and $S = 0.115\%$) : single region. The datum is at the top of the balls in the channel bed.	136
Figure A.7d	Logarithmic velocity profile for experiment G3 ($H/D_{50} = 8$ and $S = 0.115\%$) : single region. The datum is 1 mm below the top of the balls in the bed.	136

Figure A.8a	Velocity profile for experiment H3 ($H/D_{50} = 10$ and $S = 0.09\%$). The datum is at the top of the balls in the channel bed.	137
Figure A.8b	Logarithmic velocity profile for experiment H3 ($H/D_{50} = 10$ and $S = 0.09\%$) split into two regions. The datum is at the top of the balls in the channel bed.	137
Figure A.8c	Logarithmic velocity profile for experiment H3 ($H/D_{50} = 10$ and $S = 0.09\%$): single region. The datum is at the top of the balls in the channel bed.	138
Figure A.8d	Logarithmic velocity profile for experiment H3 ($H/D_{50} = 10$ and $S = 0.09\%$): single region. The datum is 1 mm below the top of the balls in the bed.	138
Figure A.9a	Velocity profile for experiment I3 ($H/D_{50} = 12$ and $S = 0.075\%$). The datum is at the top of the balls in the channel bed.	139
Figure A.9b	Logarithmic velocity profile for experiment I3 ($H/D_{50} = 12$ and $S = 0.075\%$) split into two regions. The datum is at the top of the balls in the channel bed.	139
Figure A.9c	Logarithmic velocity profile for experiment I3 ($H/D_{50} = 12$ and $S = 0.075\%$): single region. The datum is at the top of the balls in the channel bed.	140
Figure A.9d	Logarithmic velocity profile for experiment I3 ($H/D_{50} = 12$ and $S = 0.075\%$): single region. The datum is 1 mm below the top of the balls in the bed.	140
Figure A.10a	Velocity profile for $H/D_{50} = 3$ and $S = 0.21\%$ (pressurized). The datum is at the top of the balls in the channel bed.	141
Figure A.10b	Logarithmic velocity profile for $H/D_{50} = 3$ and $S = 0.21\%$ (pressurized) split into two regions. The datum is at the top of the balls in the channel bed.	141
Figure A.10c	Logarithmic velocity profile for $H/D_{50} = 3$ and $S = 0.21\%$ (pressurized): single region. The datum is at the top of the balls in the channel bed.	142
Figure A.10d	Logarithmic velocity profile for $H/D_{50} = 3$ and $S = 0.21\%$ (pressurized): single region. The datum is 1 mm below the top of the balls in the bed.	142

Figure A.11a	Velocity profile for $H/D_{50} = 4.5$ and $S = 0.21\%$ (pressurized). The datum is at the top of the balls in the channel bed.	143
Figure A.11b	Logarithmic velocity profile for $H/D_{50} = 4.5$ and $S = 0.21\%$ (pressurized) split into two regions. The datum is at the top of the balls in the bed.	143
Figure A.11c	Logarithmic velocity profile for $H/D_{50} = 4.5$ and $S = 0.21\%$ (pressurized): single region. The datum is at the top of the balls in the channel bed.	144
Figure A.11d	Logarithmic velocity profile for $H/D_{50} = 4.5$ and $S = 0.21\%$ (pressurized): single region. The datum is 1 mm below the top of the balls in the bed.	144
Figure A.12a	Velocity profile for $H/D_{50} = 5.5$ and $S = 0.21\%$ (pressurized). The datum is at the top of the balls in the channel bed.	145
Figure A.12b	Logarithmic velocity profile for $H/D_{50} = 5.5$ and $S = 0.21\%$ (pressurized) split into two regions. The datum is at the top of the balls in the bed.	145
Figure A.12c	Logarithmic velocity profile for $H/D_{50} = 5.5$ and $S = 0.21\%$ (pressurized): single region. The datum is at the top of the balls in the channel bed.	146
Figure A.12d	Logarithmic velocity profile for $H/D_{50} = 5.5$ and $S = 0.21\%$ (pressurized): single region. The datum is 1 mm below the top of the balls in the bed.	146
Figure A.13a	Velocity profile for $H/D_{50} = 6.5$ and $S = 0.21\%$ (pressurized). The datum is at the top of the balls in the channel bed.	147
Figure A.13b	Logarithmic velocity profile for $H/D_{50} = 6.5$ and $S = 0.21\%$ (pressurized) split into two regions. The datum is at the top of the balls in the bed.	147
Figure A.13c	Logarithmic velocity profile for $H/D_{50} = 6.5$ and $S = 0.21\%$ (pressurized): single region. The datum is at the top of the balls in the channel bed.	148
Figure A.13d	Logarithmic velocity profile for $H/D_{50} = 6.5$ and $S = 0.21\%$ (pressurized): single region. The datum is 1 mm below the top of the balls in the bed.	148

Figure A.14a	Velocity profile for $H/D_{50} = 8.5$ and $S = 0.21\%$ (pressurized). The datum is at the top of the balls in the channel bed.	149
Figure A.14b	Logarithmic velocity profile for $H/D_{50} = 8.5$ and $S = 0.21\%$ (pressurized) split into two regions. The datum is at the top of the balls in the bed.	149
Figure A.14c	Logarithmic velocity profile for $H/D_{50} = 8.5$ and $S = 0.21\%$ (pressurized): single region. The datum is at the top of the balls in the channel bed.	150
Figure A.14d	Logarithmic velocity profile for $H/D_{50} = 8.5$ and $S = 0.21\%$ (pressurized): single region. The datum is 1 mm below the top of the balls in the bed.	150

List of Tables

Table 2.1	Summary of data from previous research in incipient motion under shallow flow conditions.	19
Table 2.2	Summary of equations for threshold conditions in mountain rivers with shallow flows.	21
Table 3.1	Characteristics of the Spherical Particles Used in the Experiments.	28
Table 4.1	Frequency of particle displacements at threshold conditions for experiment B3 (glass balls $H/D_{50} = 3$).	39
Table 5.1	Ranges of values obtained for the different particle types (uniform flow experiments at threshold conditions).	49
Table 5.2	Summary of experiments (uniform flow at threshold conditions).	50
Table 5.3	Summary of parameters related to the criterion for threshold conditions (uniform flow experiments).	51
Table 5.4a	Summary of experiments (uniform flow at threshold conditions without considering the bursting period).	52
Table 5.4b	Summary of parameters related to the criterion for threshold conditions (uniform flow experiments without considering the bursting period).	52
Table 5.4c	Comparison of the dimensionless critical shear stress for experiments that consider the bursting period vs. those that do not.	52
Table 5.5a	Summary of experiments (M1 water surface profile at threshold conditions).	53
Table 5.5b	Summary of parameters related to the criterion for threshold conditions (experiments with M1 profile).	53
Table 5.5c	Comparison of dimensionless critical shear stress for experiments with uniform flow vs. experiments with M1 profile.	53
Table 6.1	Summary of k_s^+ and comparison of the τ_w and u^* values obtained by the LDV vs. the approximations.	69
Table 6.2	Summary of logarithmic velocity profiles for free surface flow: Single region (The datum is at the top of the balls in the channel bed).	70

Table 6.3	Summary of logarithmic velocity profiles for pressurized flow: Single region (The datum is at the top of the balls in the channel bed).	71
Table A.1	Frequency of particle displacements at threshold conditions for experiment A1 (viton balls $H/D_{50} = 2$).	84
Table A.2	Frequency of particle displacements at threshold conditions for experiment A2 (teflon balls $H/D_{50} = 2$).	85
Table A.3	Frequency of particle displacements at threshold conditions for experiment A3 (glass balls $H/D_{50} = 2$).	86
Table A.4	Frequency of particle displacements at threshold conditions for experiment A4 (ceramic balls $H/D_{50} = 2$).	87
Table A.5	Frequency of particle displacements at threshold conditions for experiment B1 (viton balls $H/D_{50} = 3$).	88
Table A.6	Frequency of particle displacements at threshold conditions for experiment B2 (teflon balls $H/D_{50} = 3$).	89
Table A.7	Frequency of particle displacements at threshold conditions for experiment B3 (glass balls $H/D_{50} = 3$).	90
Table A.8	Frequency of particle displacements at threshold conditions for experiment B4 (ceramic balls $H/D_{50} = 3$).	91
Table A.9	Frequency of particle displacements at threshold conditions for experiment C1 (viton balls $H/D_{50} = 4$).	92
Table A.10	Frequency of particle displacements at threshold conditions for experiment C2 (teflon balls $H/D_{50} = 4$).	93
Table A.11	Frequency of particle displacements at threshold conditions for experiment C3 (glass balls $H/D_{50} = 4$).	94
Table A.12	Frequency of particle displacements at threshold conditions for experiment C4 (ceramic balls $H/D_{50} = 4$).	95
Table A.13	Frequency of particle displacements at threshold conditions for experiment D1 (viton balls $H/D_{50} = 5$).	96
Table A.14	Frequency of particle displacements at threshold conditions for experiment D2 (teflon balls $H/D_{50} = 5$).	97

Table A.15	Frequency of particle displacements at threshold conditions for experiment D3 (glass balls $H/D_{50} = 5$).	98
Table A.16	Frequency of particle displacements at threshold conditions for experiment D4 (ceramic balls $H/D_{50} = 5$).	99
Table A.17	Frequency of particle displacements at threshold conditions for experiment E1 (viton balls $H/D_{50} = 6$).	100
Table A.18	Frequency of particle displacements at threshold conditions for experiment E2 (teflon balls $H/D_{50} = 6$).	101
Table A.19	Frequency of particle displacements at threshold conditions for experiment E3 (glass balls $H/D_{50} = 6$).	102
Table A.20	Frequency of particle displacements at threshold conditions for experiment E4 (ceramic balls $H/D_{50} = 6$).	103
Table A.21	Frequency of particle displacements at threshold conditions for experiment F2 (teflon balls $H/D_{50} = 7$).	104
Table A.22	Frequency of particle displacements at threshold conditions for experiment F3 (glass balls $H/D_{50} = 7$).	105
Table A.23	Frequency of particle displacements at threshold conditions for experiment F4 (ceramic balls $H/D_{50} = 7$).	106
Table A.24	Frequency of particle displacements at threshold conditions for experiment G2 (teflon balls $H/D_{50} = 8$).	107
Table A.25	Frequency of particle displacements at threshold conditions for experiment G3 (glass balls $H/D_{50} = 8$).	108
Table A.26	Frequency of particle displacements at threshold conditions for experiment G4 (ceramic balls $H/D_{50} = 8$).	109
Table A.27	Frequency of particle displacements at threshold conditions for experiment H3 (glass balls $H/D_{50} = 10$).	110
Table A.28	Frequency of particle displacements at threshold conditions for experiment H4 (ceramic balls $H/D_{50} = 10$).	111
Table A.29	Frequency of particle displacements at threshold conditions for experiment I3 (glass balls $H/D_{50} = 12$).	112

Table A.30	Frequency of particle displacements at threshold conditions for experiment D3T _B (glass balls $H/D_{50} = 5$ w/o considering the bursting period).	113
Table A.31	Frequency of particle displacements at threshold conditions for experiment E3T _B (glass balls $H/D_{50} = 6$ w/o considering the bursting period).	114
Table A.32	Frequency of particle displacements at threshold conditions for experiment B2M1 (teflon balls $H/D_{50} = 3$ with M1 profile).	115
Table A.33	Frequency of particle displacements at threshold conditions for experiment B3M1 (glass balls $H/D_{50} = 3$ with M1 profile).	116
Table A.34	Frequency of particle displacements at threshold conditions for experiment B4M1 (ceramic balls $H/D_{50} = 3$ with M1 profile).	117
Table A.35	Summary of logarithmic velocity profiles for free surface flow: Split into 2 regions (The datum is at the top of the balls in the channel bed).	119
Table A.36	Summary of logarithmic velocity profiles for free surface flow: Single region (The datum is 1 mm below the top of the balls in the channel bed).	120
Table A.37	Summary of logarithmic velocity profiles for pressurized flow: Split into 2 regions (The datum is at the top of the balls in the channel bed).	121
Table A.38	Summary of logarithmic velocity profiles for pressurized flow: Single region (The datum is 1 mm below the top of the balls in the channel bed).	122

List of Symbols

A = inverse of the von Karman constant

B = integral constant

C = Chezy friction factor

C_D = drag force coefficient

D_{50} = median particle diameter, [L]

D_{65} = particle diameter for which 65% of particles are finer, [L]

D_{84} = particle diameter for which 84% of particles are finer, [L]

D_{90} = particle diameter for which 90% of particles are finer, [L]

f = Darcy-Weisbach friction factor

f_{avg} = average frequency of particle displacement, [L^{-1}]

$f_{\text{avg,crit}}$ = critical average frequency of particle displacement, [L^{-1}]

f_i = frequency of particle displacement in a time period, [L^{-1}]

F_D = drag force, [ML/T^2]

F_G = submerged weight of the sphere, [ML/T^2]

F_L = lift force, [ML/T^2]

F_N = normal force, [ML/T^2]

F_T = tangential force, [ML/T^2]

Fr = Froude number

Fr_c = critical Froude number

Fr_D = densimetric Froude number

g = acceleration due to gravity, [L/T^2]

H = flow depth, [L]

k = the physical height of a typical roughness element, [L]

k_e = relative roughness of a vessel

k_s = a representative length of the roughness elements, [L]

k_s^+ = dimensionless roughness length

l = length, [L]

n = Manning's number

N_E = the number of particles entrained in a time period

N_T = the total number of particles in a viewing area at the beginning of a time period

P_E = probability of particle entrainment

P_{Ecrit} = critical probability of entrainment

Q = discharge, $[L^3/T]$

R = submerged specific gravity

R^2 = correlation coefficient

Re = Reynolds number

Re_p^* = particle Reynolds number

R_h = hydraulic radius, $[L]$

S = slope

SG = specific gravity

T_B = bursting period, $[T]$

u^* = friction velocity, $[L/T]$

u_{cr}^* = friction velocity at critical conditions, $[L/T]$

u' = fluctuating component of the velocity in the x direction, $[L/T]$

v' = fluctuating component of the velocity in the z direction, $[L/T]$

V = depth-averaged velocity, $[L/T]$

V_c = depth-averaged velocity corresponding to critical conditions, $[L/T]$

V_{max} = mean velocity at the outer edge of the boundary layer, $[L/T]$

y = distance above the bed, $[L]$

y_+ = dimensionless distance from bed

z = distance above the datum, $[L]$

z_o = depth of submergence, $[L]$

δ = boundary layer thickness, $[L]$

Δh = head differential, $[L]$

Δt_i = time period, $[T]$

γ_f = specific weight of the fluid, $[M/L^2 T^2]$

γ_s = specific weight of the sediment particle, $[M/L^2 T^2]$

κ = the von Karman constant

μ = dynamic viscosity, $[M/LT]$

ν = kinematic viscosity, $[L^2/T]$

Π = wake-strength coefficient

ρ_f = density of the fluid, [M/L³]

ρ_s = density of the sediment particles, [M/L³]

σ = standard deviation

τ_{cr} = critical boundary shear stress, [M/LT²]

τ_{cr}^* = dimensionless critical shear stress

τ_w = shear stress at the wall, [M/LT²]

Chapter 1. Introduction

1.1 Brief Definition of Incipient Motion

The present study focuses on the incipient motion of sediment particles under shallow flow conditions. Incipient, or threshold conditions are established when the flow intensity in a channel is barely enough to entrain the particles in a movable bed. The hydrodynamic forces of the fluid, acting on the particles, are responsible for their motion. During the decades of research in this area, numerous investigators have defined incipient motion in different ways. For a detailed review of some definitions, the reader is referred to Papanicolaou (1997).

1.2 Threshold Conditions in Mild Sloped Channels

Research in the area of incipient motion is dominated by work in mild sloped channels or lowland rivers. In these channels, flow depths are usually high relative to the diameter of the particles in the bed. The Shields (1936) diagram is typically used to show the conditions for the beginning of sediment motion in mild channel beds. It relates the dimensionless shear stress necessary to cause sediment movement with the particle Reynolds number. This relationship is deduced from dimensional analysis $f(\tau_{cr}, \rho_f, \mu, D_{50}, \gamma_s - \gamma_f) = 0$, reducing the number of variables to only two:

$$f\left(\frac{\tau_{cr}}{D_{50}(\gamma_s - \gamma_f)}, \frac{u_{cr}^* D_{50}}{\nu}\right) = 0 \quad (1.1)$$

where τ_{cr} = critical boundary shear stress; ρ_f = density of the fluid; μ = dynamic viscosity; ν = kinematic viscosity; D_{50} = median particle diameter; γ_s = specific weight of the sediment particle; γ_f = specific weight of the fluid; and u_{cr}^* = friction velocity at critical conditions. The friction velocity is expressed as

$$u_{cr}^* = \sqrt{\frac{\tau_{cr}}{\rho_f}} \quad (1.2).$$

The first term in equation 1.1 is the dimensionless critical shear stress (τ_{cr}^*) and the second term is the particle Reynolds number (Re_p^*). Equation 1.1 can also be obtained by taking moments about the pivot point when a sediment particle is just starting to rotate. Figure 1.1 (Ling 1995) shows the forces acting on a non-cohesive spherical particle in the

presence of moving fluid. The pivot point in this case is point A and F_L = lift force, F_D = drag force, F_G = submerged weight of the sphere, F_N = normal force from sphere O_3 , and F_T = tangential force from sphere O_3 . The reactional forces from sphere O_2 are zero when sphere O_1 is about to move to the right.

Experiments have shown that at about $Re_p^* > 200$, the dimensionless critical shear stress, or Shields parameter, becomes independent of the particle Reynolds number. This region is commonly referred to as the Reynolds number independent region of the Shields diagram. Typical values of this constant Shields parameter vary between 0.03 and 0.06, depending on the criterion for critical conditions used. Sediment particles with a median diameter greater than 2 mm usually lie in this region.

1.3 Introduction to Free Surface Effects on Incipient Motion

The main focus of the present research is in mountain rivers, where the velocities are high, the bed material is coarse and the flow depths are low relative to the diameter of the particles in the bed. Due to the presence of surface waves and the proximity of the sediment particles to the free surface, the applicability of the traditional Shields diagram to predict the initiation of motion becomes questionable. Objects moving near a liquid-gas or liquid-liquid interface are not only affected by skin friction drag and form drag, but also by gravitational forces, or wave drag. Therefore, in addition to the Reynolds number, the Froude number must be considered as a factor affecting the initiation of motion of sediment particles interacting with the free surface. The influence of the wave drag can be seen by simple experiments such as towing a model sperm whale. Lab experiments have shown that for a certain towing line tension, the model whale's velocity is higher when well submerged than when near the surface. The difference in velocity is more pronounced at higher towing tensions.

1.4 Analogy to a Submarine Moving Near the Surface of the Ocean

Sediment particles under shallow flow experience similar conditions as submarines moving near the surface of the ocean. In both cases, the objects are interacting with the free surface. Due to the generation of interfacial waves by the vessel,

the Froude number is considered as an additional parameter affecting the drag force coefficient because gravity affects the flow field. Therefore,

$$C_D = f(\text{geometry}, k_e, \text{Re}, \text{Fr}) \quad (1.3)$$

where C_D = drag force coefficient; k_e = relative roughness of the vessel; Re = Reynolds number; and Fr = Froude number. The gravitational effect decreases as the depth of submergence relative to the interface increases. Eventually, the drag coefficient becomes a function of only geometry, relative roughness and Reynolds number. Theoretical values of wave drag for different relative submergences have been obtained for slender ellipsoidal bodies (Wigley 1953). The relative submergence in this case is defined as z_o/l , where z_o = depth of submergence and l = length of the ellipsoid. These values show that the wave drag becomes unimportant when the relative submergence exceeds 0.5.

1.5 Flow Resistance Equations for Large-scale Roughness

Since the hydraulic conditions in mountain rivers are different to the conditions in lowland rivers, Thorne and Zevenbergen (1985) suggested that flow-resistance equations valid in lowland rivers should not be applied to mountain rivers. These equations are expressions for friction factors such as Manning's n , Chezy C , and Darcy-Weisbach f . Several semi-analytical and purely empirical flow resistance equations specifically intended for large-scale roughness have been proposed. Large-scale roughness is the type of bed roughness associated with mountain rivers, where the flow depth is low relative to the size of the bed material. Using data from a mountain river, Thorne and Zevenbergen tested three equations developed for large-scale roughness. For relative roughness $(R_h/D_{84}) < 1$ they recommended either an equation developed by Bathurst (1978) or an equation developed by Thompson and Campbell (1979). For $(R_h/D_{84}) > 1$ they recommended an expression derived by Hey (1979). In the relative roughness ratio, R_h = hydraulic radius and D_{84} = particle diameter for which 84% of particles are finer.

1.6 The Influence of the Relative Depth on Incipient Motion

Several researchers (Ashida and Bayazit 1973, Mizuyama 1977, Bathurst et al. 1982, Suszka 1991) studied the effect of decreasing relative depth on the incipient motion of sediment particles. The relative depth is defined as H/D_{50} , where H = flow depth. Most

of these tests used coarse natural gravel, so the results are in the Reynolds number independent region of the Shields diagram. Their data, shown in Figure 2.1, reveal that for $H/D_{50} < 10$, approximately, the dimensionless critical shear stress is not a constant as the traditional Shields diagram predicts, but increases with decreasing relative depth. A modified version of the Shields diagram showing the relationship between the dimensionless critical shear stress and H/D_{50} was developed. At high relative depths (>10 , approximately) the Shields parameter becomes constant as the original Shields diagram predicts. The results obtained by the investigators mentioned will be discussed in greater detail in Section 2.1.

1.7 Focus of this Study

The focus of this study is to examine the dependence of threshold conditions on parameters other than those included in the traditional Shields diagram, such as Froude number and relative depth. First, this dependence will be examined via dimensional analysis and subsequently by a variety of experiments that were run at the Kelso Baker Laboratory in the Virginia Polytechnic Institute. Data available in the literature will be reanalyzed as well.

Experiments with shallow flows are important due to the increasing water resource development of mountain regions worldwide. The results presented in this work can be used in applications such as the design of stable riprap to protect river beds from erosion. However, with the analogy to the submarine and the model sperm whale example, it was shown that this work is of relevance to other fields as well.

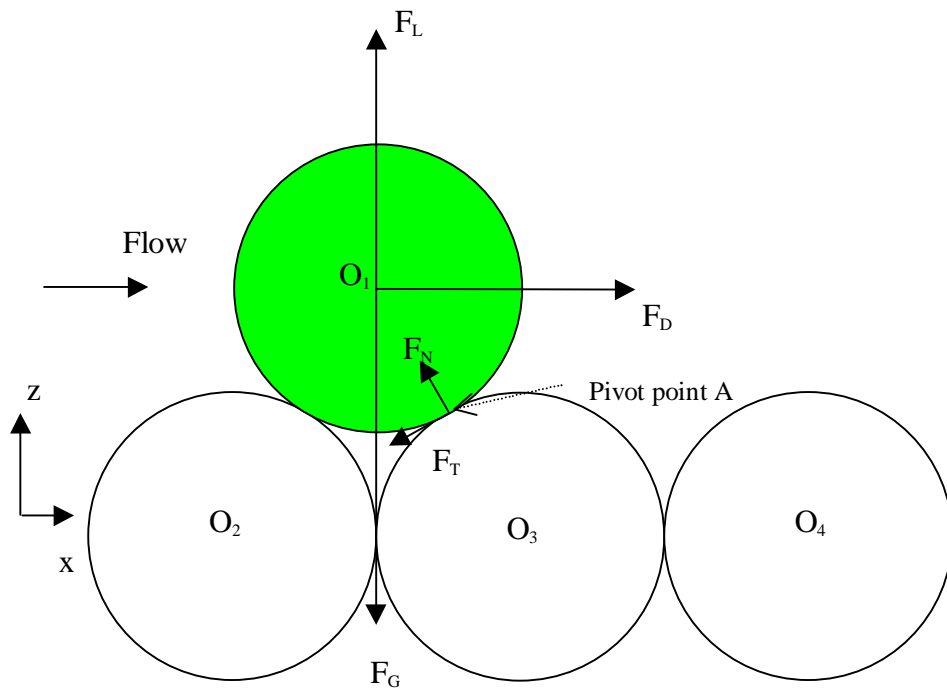


Figure 1.1 The forces acting on a non-cohesive spherical particle in the presence of moving fluid.

Chapter 2. Literature Review

2.1 Initiation of Motion in Steep Channels with Shallow Flows

2.1.1 Dimensionless Critical Shear Stress as a Function of Relative Depth

Several approaches have been presented for predicting the initiation of sediment motion in steep channels with shallow flows. The most common approach is to relate the dimensionless critical shear stress to the relative depth, H/D_{50} . Realizing a need for data at low relative depths, Ashida and Bayazit (1973) ran a set of experiments in a tilting flume using natural gravel. The results are summarized in Table 2.1. The relative depth in this set of experiments ranges from 0.6 to 8.5. Shields' approach of extrapolation to zero transport was used as a criterion for threshold conditions. The results show that the dimensionless critical shear stress increases considerably as the flow becomes shallower. In fact, τ_{cr}^* for the lowest relative depth in the range turns out to be over 3 times higher than the τ_{cr}^* corresponding to the highest relative depth. Mizuyama (1977) used this data as well as data from Tabata and Ichinose (1971) to develop an empirical expression for the dimensionless critical shear stress as a function of relative depth. It was suggested that for $H/D_{50} \geq 4.55$, $\tau_{cr}^* = 0.04$. This might indicate that the traditional Shields diagram can be used to predict the initiation of sediment motion at relative depths greater than 4.55. However, caution must be exercised because the data show some scatter. For $H/D_{50} \leq 4.55$, the empirical expression is

$$\tau_{cr}^* = 0.034 \times 10^{0.32(D_{50}/H)} \quad (2.1).$$

Although Ashida and Bayazit attempted to explain the causes for this behavior by analyzing velocity profiles, they pointed out that more research is needed to come up with an explanation. Suszka (1991) studied the same type of relationship using gravel-bed flume data from 5 sources (USWES 1935, Ho Pang-Yung 1939, Meyer-Peter and Muller 1948, Cao 1985, and Suszka 1987). This data is summarized in Table 2.1. The Paxis and Graf (1977) probability concept was used as the criterion for incipient conditions. The range of relative depths in this data set ($H/D_{50} = 1.2-50$) is considerably wider than the Ashida and Bayazit range. The relationship between τ_{cr}^* and H/D_{50} for both data sets is plotted in Figure 2.1. The two data sets follow the same general trend. Slight differences can be explained by the different criterion for threshold conditions

used. Suszka's data points indicate that the traditional Shields diagram can be used for relative depths greater than 10, approximately. Figure 2.1 shows that $\tau_{cr}^* \approx 0.04$ in this region. Suszka used the data to express τ_{cr}^* as a power function of relative depth as follows

$$\tau_{cr}^* = 0.0851 \left(\frac{H}{D_{50}} \right)^{-0.266} \quad (2.2).$$

Four additional gravel-bed flume data points by Bathurst, Graf and Cao (1982) were added to Figure 2.1 and are summarized in Table 2.1. Their data follow the same trend and blend in well with the rest of the points. Bathurst et al. did a similar analysis using their incipient motion data as well as that of several other investigators (Gilbert 1914, Meyer-Peter and Muller 1948, Ashida and Bayazit 1973). In addition, they looked further into the effect of slope, S . Their analysis indicated that for flows with $S \leq 1\%$, the dimensionless critical shear stress varies gradually and remains between 0.04-0.06 as in the Reynolds number independent region of the traditional Shields diagram. In a similar approach, Graf and Suszka (1987) used their own data as well as data from Cao (1985) and Mizuyama (1977) to study the effect of slope on the dimensionless critical shear stress. The highest slope in this data is about 20%. Based on this study it is evident that for particle Reynolds numbers greater than about 500, the Shields parameter is dependent on the slope. The relation fitted to the data is

$$\tau_{cr}^* = 0.042(10^{2.2S}) \quad (2.3).$$

This data also shows that for $0.005 < S < 0.025$ the average value of τ_{cr}^* is 0.045. The upper limit of the slope ($S = 2.5\%$) for obtaining this constant Shields parameter is considerably higher than that given by Bathurst et al. ($S = 1\%$). The value of τ_{cr}^* given by Graf and Suszka is also within the bounds usually obtained in the Reynolds number independent region of the Shields diagram. It must be pointed out that τ_{cr}^* in this region is considerably lower when dealing with fully exposed spherical particles. Fenton and Abbott (1977) and Coleman (1967) obtained values close to 0.01 for this case.

In another set of steep slope experiments with coarse particles, Abt et al. (1988) report τ_{cr}^* values as high as 0.12. The range of relative depth in this set is 0.48-2.01. It was reported that the flow in these experiments was highly aerated. Wittler and Abt

(1995) commented that the values of the Shields parameter obtained were entirely due to air entrainment and ruled out a relative depth effect. The presence of aeration was not reported in the investigations mentioned earlier. Therefore, it is not adequate to compare the Abt et al. data to the data in Figure 2.1.

Bettess (1984) suggested incorporating results similar to those in Figure 2.1 to the Shields diagram. The idea is to have a family of parallel curves in the Reynolds number independent region of the Shields diagram. Each curve represents a particular H/k_s , where k_s = a representative length of the roughness elements. The dimensionless critical shear stress increases as H/k_s decreases. Bettess did not plot actual data to create such a family of parallel curves, but suggested that the initiation of motion in steep gravel-bed streams be described by an equation in the form

$$\tau_{cr}^* = (\text{constant}) \times f\left(\frac{H}{k_s}\right) \quad (2.4)$$

where $f(H/k_s) \rightarrow 1$ as H/k_s becomes large. Using the data he analyzed, Suszka plotted this relationship, but used H/D_{50} instead of H/k_s . The results were mixed. Scatter is sometimes significant, causing points to be out of place. For instance, one point at $H/D_{50} = 3$ lies between the curves corresponding to relative depths of 7 and 10. Therefore, creating this family of parallel curves might not be trivial. Also, a large amount of experiments may be required to create a curve corresponding to a single relative depth.

Cheng (1969) and Neill's (1967) dimensional analysis for the initiation of sediment motion is slightly different than that obtained by Shields. The equation is

$$\frac{\rho_f V_c^2}{(\gamma_s - \gamma_f) D_{50}} = f\left(\frac{V_c D_{50}}{\nu}, \frac{D_{50}}{H}, \frac{\rho_s}{\rho_f}\right) \quad (2.5)$$

where V_c = depth averaged velocity corresponding to critical conditions. The term in the left-hand side of the equation is the Shields parameter expressed in a different form and using V_c instead of u_{cr}^* . The 3 terms in the right hand side of the equation from left to right are, the particle Reynolds number, the relative roughness, which serves the same purpose as the relative depth, and the density ratio. The particle Reynolds number is irrelevant when using coarse bed material greater than about 2 or 3 mm in median diameter. Equation 2.5 shows that the relative density is of importance in this problem. Cheng (1969) ran experiments in a narrow range of relative depths ($H/D_{50} = 0.3-1.7$) to

study the effects on the dimensionless critical shear stress. Again, the trend is similar to that seen in Figure 2.1. However, the changes are more dramatic. Although the range of relative depths is very narrow, the Shields parameter for the shallower flows is over 4 times greater than that for the deeper flows. The state of incipient motion for this study is described by the following expression:

$$\frac{\rho V_c^2}{(\gamma_s - \gamma_f) D_{50}} = 2.0 \left(\frac{D_{50}}{H} \right)^{2/3} \quad (2.6).$$

These results cannot be fairly compared to those in Figure 2.1 because the tests were conducted differently. A gravel bed was not used. Instead, the bed was made up of well-packed spheres 1 ft in diameter. Only one ball, the test particle, was allowed to move. This ball was part of the well-packed bed. Different discharges were applied until the test particle barely started moving out of the bed. Although the main focus of the analysis involved the relative depth (or relative roughness), Cheng also looked further into the effect of the density ratio. The range of densities used was very narrow ($SG = 1.1-1.5$), but the results showed that the density ratio is a factor affecting incipient motion. Aguirre-Pe (1975) ran experiments at threshold conditions using a wider range of particle densities ($SG = 1.04-6.9$) and also noticed that the particle density has an effect on the Shields parameter. The functional relationship obtained from his data is

$$\tau_{cr}^* \left(\frac{\gamma_s - \gamma_f}{\gamma_f} \right)^{1.17} = (5.6 \times 10^{-11}) (\text{Re}_p^*)^{2.30} \quad (2.7).$$

These experiments were run at slopes as high as 9.5% and at τ_{cr}^* as high as 0.092. Although he mentioned that this work is applicable to mountain rivers, the analysis did not take into account the effect of the relative depth. In any case, the τ_{cr}^* values from the Aguirre-Pe study cannot be compared to the other results mentioned in this section because cubical particles, 5cm high, were used. Their packing density (concentration) was 16% and only one was movable. The findings concerning the effect of particle density on incipient motion are relevant to the present study because 4 different particle densities are used.

The results discussed so far are based on experimental data. To the author's knowledge, theoretical studies on the relationship between τ_{cr}^* and H/D_{50} are not

common. Aksoy (1973) conducted a theoretical study. Using the forces acting on a sediment particle, as shown in Figure 1.1, a balance of moments was taken about the pivot point. After several rearrangements and substitutions, the functional relationship for threshold conditions is

$$\left(\frac{\rho_f}{\rho_s - \rho_f} \right) S = f \left[\left(\frac{D_{50}^{3/2}}{\nu} \sqrt{g \frac{\rho_s - \rho_f}{\rho_f}} \right) \frac{R_h}{D_{50}} \right] \quad (2.8).$$

In wide channels the hydraulic radius is approximately equal to the flow depth. Equation 2.8 is a different method of showing that the relative depth is a factor to consider at threshold conditions. For simplicity, the term on the left hand side of the equation will be called Y and the first term on the right will be called X. Although this relationship does not include τ_{cr}^* , it can easily be obtained by multiplying Y by R_h/D_{50} . Referring to the functional relationship (Eq. 2.8), Aksoy plotted a family of parallel curves, each representing a particular relative depth (R_h/D_{50}) in a graph with the Y and X terms on the axes. This study did not make use of new experimental data. Instead, Aksoy used selected values in combination with the traditional Shields diagram to develop the family of curves. Each curve is shaped like the traditional Shields curve. The disadvantage of equation 2.8 is the spurious correlation of the submerged specific weight.

So far in this discussion, data from a variety of sources have shown that τ_{cr}^* increases with decreasing relative depth in shallow flows. Data obtained from a Chinese river by Li (1965) show the opposite effect. This limited set of data has a relative depth range of 6.5-9.25. Interestingly enough, $\tau_{cr}^* = 0.153$ at $H/D_{50} = 6.5$ and $\tau_{cr}^* = 0.326$ at $H/D_{50} = 9.25$. Wang and Shen (1985) analyzed this data along with another set of data from Chinese rivers reported by Wang (1975). The relative depth for all the Wang data is around 10 and a best-fit line shows that $\tau_{cr}^* = 0.062$. According to Wang and Shen, the cause for the dramatic increase of τ_{cr}^* in Li's data is caused by the significant reduction in the drag coefficient, C_D , that occurs at Reynolds numbers between 10^4 and 10^5 . Li's data has very high particle Reynolds numbers ($> 10^5$) and particle sizes much larger than those used by most of the other authors mentioned. For example, the coarsest particle in the Ashida and Bayazit study is 2.25 cm while in Li's study the median diameter of the particles is 40 cm. The main drawback of Li's data is that it is very limited. Also, it is

more difficult to have a clear definition of incipient conditions in the field than it is in a laboratory flume. Finally, Wittler and Abt (1995) commented that the experiments analyzed by Wang and Shen were affected by aeration just like the Abt et al. (1988) tests.

Table 2.2 summarizes the research mentioned in this as well as the next section. The various formulae and expressions should be applied with caution when designing riprap. Before using one of them, one must look into how that particular relationship was developed. The preference of the author is to use the information in Figure 2.1 for several reasons. First, natural gravel was used and this most closely resembles riprap. Second, the data comes from a variety of sources and seem to agree well with each other. Finally, the fact that $\tau_{cr}^* \approx 0.04$ in the Reynolds number independent region shows that these results agree well with those in well-known publications. A safety factor must always be applied because scatter is present when dealing with incipient motion data.

The relationship between τ_{cr}^* and H/D_{50} in mountain rivers with shallow flows has been shown through experiments and limited theory by the investigators mentioned and a few others. However, to the author's knowledge, no serious attempt has been made to attribute this phenomenon to physical causes. Velocity profiles obtained by Ashida and Bayazit (1973) showed that the non-dimensional velocity (V/u^*) at a certain distance from the bed decreases as the flow depth decreases and the friction factor increases as relative depth decreases. Therefore, one possible explanation is that a higher shear stress is required to entrain the sediment as a result of this velocity drop. It was further commented that this may only be a partial explanation.

2.1.2 Dimensionless Critical Shear Stress as a Function of Froude Number

Another approach for predicting the initiation of motion in mountain rivers with shallow flows is by relating the Shields parameter (τ_{cr}^*) to the Froude number. This relationship is not as common as the one discussed in Section 2.1.1 and has been brought to attention only in the recent years. Kilgore and Young (1993) collected data from a variety of sources (GKY & Associates 1993, Parola 1991, Neill 1967, Wang and Shen 1985) and plotted τ_{cr}^* vs. Froude number. This plot shows that a strong correlation exists between the dimensionless critical shear stress and the Froude number. For flows with Froude number less than about 0.4, τ_{cr}^* is approximately equal to 0.05, which is in

between the values of 0.04-0.06 typically obtained in the Reynolds number independent region of the traditional Shields diagram. At $Fr > 0.4$, τ_{cr}^* increases as the Froude number increases. Kilgore and Young suggest that the traditional Shields diagram should not be used to design riprap for flows with Froude number greater than 0.8. The following empirical expression, which is valid for any Froude number, was developed:

$$\tau_{cr}^* = 0.052(Fr)^{2.7} + 0.05 \quad (2.9).$$

The advantage of this expression is that it is based on data from several well-known sources and the scatter is not significant. However, some values of τ_{cr}^* in this data set might be too high. More than 10 points have a dimensionless critical shear stress that exceeds 0.15. In comparison, the highest values of τ_{cr}^* obtained by Ashida and Bayazit (1973), Suszka (1991), and Bathurst et al. (1982) are 0.1178, 0.098, 0.108, respectively. The Kilgore and Young equation tends to over-predict the dimensionless critical shear stress. For example, a data point from the Bathurst et al. (1982) data with a Froude number of 1.23 has a τ_{cr}^* value of 0.108. According to equation 2.9, the shear stress is 0.141. The high values of τ_{cr}^* obtained by Kilgore and Young can be explained in part by the use of Wang and Shen's (1985) data, which has raised some questions as mentioned earlier. Figure 2.2 shows a comparison of equation 2.9 and the data points from Bathurst et al. and Ashida and Bayazit. Suszka's data is not included because he provides no information on velocity. The data points from the Bathurst et al. and Ashida and Bayazit analyses have a significant amount of scatter. One possible explanation is that the Froude numbers from the Ashida and Bayazit study were calculated using a depth averaged velocity based on the flow rate. This might not be an accurate velocity because the slopes and Froude numbers were very high and the flow depths very low. The presence of surface waves and possible aeration make the velocity difficult to measure accurately.

Grant (1997) developed an analytical equation that gives the Froude number at incipient conditions for a specified slope and dimensionless critical shear stress. This equation is

$$Fr = 2.18 \left[\ln \left(1.65 \frac{\tau_{cr}^*}{S} \right) + 1.35 \right] \sqrt{S} \quad (2.10).$$

Equation 2.10 is based on the assumption of steady, one-dimensional, uniform flow and does not take into account the increased flow resistance created by free surface instabilities and hydraulic jumps at low relative depths. It was created using an experimental logarithmic velocity equation developed by Bayazit (1982) for steep, hydraulically rough channels. This logarithmic equation is

$$\frac{V}{u^*} = 2.18 \left[\ln \left(\frac{H}{D_{84}} \right) + 1.35 \right] \quad (2.11)$$

where V = depth-averaged velocity; u^* = friction velocity; and D_{84} = 84th percentile grain size in the channel bed. Table 2.1 shows a comparison of the actual Froude numbers obtained by Ashida and Bayazit (1973) and Bathurst et al. (1982) vs. those predicted by equation 2.10. This equation predicts most of the experiments at $Fr < 1.3$ within 20%. However, experiments at the higher Froude numbers are not predicted well. One possible explanation is that some of the Ashida and Bayazit tests were taken at very steep slopes (15-20%) and might not meet the assumptions of equation 2.10. Grant also mentioned that flow resistance varies with Froude number and this might not be accounted for in the equation. Therefore, caution must be exercised when using equation 2.10 for very high Froude numbers.

Bartnik (1991) realized the importance of both the Froude number and the relative depth for incipient motion in mountain rivers. Using data from four Polish rivers he obtained a relationship relating the critical Froude number (Fr_c) to the relative depth. This equation is

$$Fr_c = 1.35 \left(\frac{H}{D_{50}} \right)^{-0.35} \quad (2.12).$$

Although Bartnik stressed the importance of both parameters, equation 2.12 suffers from a major disadvantage, which is the fact that τ_{cr}^* is not incorporated. Riprap cannot be sized properly without knowledge of the dimensionless critical shear stress.

This section will end with a short discussion on the highest Froude numbers that are to be expected in natural channels. Based on personal communication with other modelers and years of experience, Trieste (1992) commented that few situations arise where supercritical flow exists along a channel reach longer than 7.6 m. Bathurst (1978)

noted supercritical flow in a very limited areal extent. Field data collected by Jarrett (1984) with slopes as steep as 5.2% indicate that all flows were sub-critical. After reviewing data from 433 gaging stations in Colorado, Wahl (1993) indicated that very few flows were supercritical. These authors agree that supercritical flow appears in small reaches of high-gradient channels, but quickly changes back to sub-critical because of extreme energy dissipation and turbulence due to obstructions. Bathurst et al. (1979) also showed that additional energy is consumed when bed material is transported. Even though few situations revealed supercritical flow, Jarrett and Wahl's data indicate that a significant number of flows in natural channels have Froude numbers between 0.7 and 1.0. As shown by Kilgore and Young's data, there is a strong relationship between τ_{cr}^* and the Froude number in that range.

From the discussion in Sections 2.1.1 and 2.1.2 it is obvious that a strong correlation exists between the dimensionless critical shear stress and both relative depth and the Froude number. However, to the author's knowledge, a single plot or equation showing this relationship has not been developed. The present study intends to fill this gap.

2.2 Velocity Profiles

2.2.1 Velocity Distribution in Smooth and Rough Walls

Turbulent flows in open channels are split into an inner and an outer region. In the inner region, the nature of the wall imposes a direct effect upon the flow, whereas in the outer region it does not. The velocity distribution in the inner region is typically described by the law of the wall, while in the outer region it is described by the velocity-defect law. No sharp dividing line exists between the two regions. Nezu and Nakagawa (1993) gave a rough estimate of the extent each region, suggesting that the inner region is at $y/H < 0.2$ and the outer region is at $y/H > 0.2$, where y = distance above the bed. The expression used to describe the inner region depends whether the bed is hydraulically smooth or rough. The effects of the roughness elements are usually classified in three categories using the ratio $k_s^+ \equiv k_s/(v/u^*)$, where k_s = a representative length of the roughness elements. The three categories are (1) hydraulically smooth bed ($k_s^+ < 5$), (2) incompletely rough bed ($5 \leq k_s^+ \leq 70$), and (3) completely rough bed ($k_s^+ > 70$).

In hydraulically smooth boundaries, the roughness elements are submerged in the viscous sublayer, where viscous stresses dominate and Reynolds stresses are negligible. The resistance depends on the Reynolds number of the flow and therefore the velocity distribution, $V/u^* = f(u^*y/\nu)$. The extent of the viscous sublayer is $y^+ < 6$, approximately, where $y^+ =$ the dimensionless distance from the bed, or u^*y/ν . The expression for the velocity distribution in the viscous sublayer is

$$\frac{V}{u^*} = \frac{u^* y}{\nu} \quad (2.13).$$

The other part of the inner region is fully turbulent. The velocity distribution in this part of the inner region is described by a logarithmic equation of the following form:

$$\frac{V}{u^*} = A \ln \frac{u^* y}{\nu} + B \quad (2.14)$$

where $A = 1/\kappa$ (κ is the universal von Karman constant), and $B =$ an integral constant. The constants obtained by Nezu and Rodi (1986) are $\kappa = 0.412$ and $B = 5.29$. Their velocity profiles were taken using a laser-Doppler anemometer (LDA). These values are comparable to other authors' results. Kirkgoz (1989) obtained $\kappa = 0.41$ and $B = 5.5$ for open-channel flow, while Dean (1978) obtained $\kappa = 0.41$ and $B = 5.17$ in rectangular ducts and Nikuradse (1932) obtained $\kappa = 0.4$ and $B = 5.5$ for hydraulically smooth pipe flows. A range where neither equation 2.13 or 2.14 applies is called the buffer zone.

In completely rough boundaries, the form drag of the roughness elements plays a very important role and therefore the velocity distribution, $V/u^* = f(z/k_s)$, where $z =$ distance above the datum. The viscous sublayer disappears. The logarithmic equation for the inner region of fully rough boundaries is

$$\frac{V}{u^*} = \frac{1}{\kappa} \ln \frac{z}{k_s} + B \quad (2.15).$$

A typical value of the integral constant B is 8.5 (Nikuradse 1933, Monin and Yaglom 1975). Kirkgoz (1989) used equation 2.14 instead of 2.15 for hydraulically rough surfaces and obtained $B = -0.8$. However, due to the significant influence of the roughness elements in fully rough flow, equation 2.15 is more appropriate.

For practical purposes, it has been common to use the logarithmic law to approximate the velocity distribution of the entire flow depth in open channels.

However, results obtained by Nezu and Rodi (1986) show that data in the outer region can deviate from the logarithmic velocity equation. Nezu and Nakagawa (1993) pointed out that this deviation cannot be neglected near the free surface ($y/H > 0.6$) at sufficiently high Reynolds numbers. The expression for the velocity profile in the outer region is

$$\frac{V_{\max} - V}{u^*} = -\frac{1}{\kappa} \ln \frac{z}{\delta} + 2 \frac{\Pi}{\kappa} \quad (2.16)$$

where V_{\max} = mean velocity at the outer edge of the boundary layer; δ = boundary layer thickness (in open-channel flows it coincides with the flow depth, H); and Π = wake-strength coefficient, which describes the deviation from the logarithmic law in the outer region. A typical value for the wake-strength coefficient is that obtained by Nezu and Rodi, $\Pi = 0.2$. Traditionally, the constants A and B in the log-law were adjusted to account for the deviation. However, Nezu and Nakagawa advised against that procedure.

2.2.2 Selection of the Roughness Length (k_s) and Datum

Equation 2.15 requires the selection of a representative roughness length and a datum. This section will review typical values of k_s suggested as well as a common approach of selecting the datum.

The equivalent roughness in a plane bed is usually related to the largest particles of the bed material (i.e D_{65} , D_{84} , D_{90}). Van Rijn (1982) analyzed 120 sets of flume and field data (Ackers 1964, Kamphuis 1974, Nordin 1964, Peterson and Howells 1973) with movable plane bed conditions. The data shows a significant amount of scatter with equivalent roughness varying between 1-10 D_{90} of the bed material, where $D_{90} = 90^{\text{th}}$ percentile grain size in the channel bed. Van Rijn recommended an average value of $k_s = 3D_{90}$. This value is close to those obtained by Kamphuis (1974), $k_s = 2.5D_{90}$, and Hey (1979), $k_s = 3.5D_{84}$. Lower values were obtained by Diplas (1990), $k_s = 2D_{90}$, Einstein and Barbarossa (1953), $k_s = D_{65}$, and Ackers and White (1973), $k_s = 1.25D_{35}$. Nezu and Nakagawa (1993) stated that the value obtained for k_s depends on the method used to determine it. Typically, it is determined using either a friction law or the law of the wall.

In flows with large-scale roughness, it is typical to use a hypothetical bed as the datum. The hypothetical bed is where it is assumed that the mean velocity along the wall is zero. Bayazit (1982) reviewed the work of several authors and found that the

theoretical bed level varies between $0.15-0.35k$ below the top of the roughness elements in the bed, where k = the physical height of a typical roughness element. Einstein and El-Samni (1949) found their datum to be at $0.2k$ below the top of the spheres making up the bed. A widely used approach for locating the hypothetical bed level is that proposed by Perry and Joubert (1963), Clauser (1954) and others. According to this method, the datum is the level below the roughness elements that gives the best-fit straight line in the logarithmic inner region.

2.2.3 Velocity Profiles in Steep Channels with High Froude Numbers

As mentioned earlier, Nezu and Rodi (1986) obtained values of $\kappa = 0.412$ and $B = 5.29$ for the logarithmic velocity equation of hydraulically smooth open-channel flows. According to their results, these constants do not vary with the Reynolds or Froude numbers. However, the Froude number in their set of experiments did not exceed 1.24. Studies in open channels with steep slopes and shallow flows are limited due to the difficulties encountered in making measurements. Recently, Tominaga and Nezu (1992) examined the von Karman and integral constants in flows with Froude number as high as 3. Experiments were carried out in both smooth and rough beds. The smooth beds consisted of acrylic resin and vinyl chloride plates, while in the case of the rough bed sandpaper was pasted over the smooth plates. Their data are reliable because a 2D LDA was used for the measurements. Equation 2.14 was used for both the rough and smooth walls, but it is more appropriate to use equation 2.15 for rough walls. For the wide range of Froude numbers (0.32-3.05), the von Karman κ is 0.41 using linear regression. This shows that κ is a universal constant, even in steep and shallow flows. On the other hand, the integral constant B varies with the Froude number. In subcritical flows, the integral constant B obtained by Tominaga and Nezu coincides fairly well with the 5.29 value obtained by Nezu and Rodi. The scatter is large, but a decrease in B can be noted in supercritical flows. For most of the rough wall data points, B drops to between 2 and 3 at Froude numbers between 1.5 and 2.0. At Froude numbers above 2, B drops to values below 2 and is negative in some cases. The drops in B are less dramatic for the smooth walls. For the acrylic resin bed, B varies between 2 and 4 at Froude numbers between 2 and 3. For the vinyl chloride bed, the scatter is very large. B varies from about 1 to 4 in

that same Froude number range. Prinos and Zeris (1995) ran similar experiments, but without a roughened surface. The bed was composed of thick aluminum plates. The velocity and boundary shear stress measurements were carried out by the use of a Preston tube, which is not as accurate as an LDA because it is intrusive. In subcritical flows, the integral constant agrees fairly well with the value obtained by Nezu and Rodi. It drops at high Froude numbers, but less dramatically than it does in the Tominaga and Nezu data. The integral constant B varies between 3.6 and 4.2 at Froude numbers between 2 and 3. The results show that the drop of B with respect to the Froude number might depend on the roughness of the bed.

Table 2.1 Summary of data from previous research in incipient motion under shallow flow conditions.

Author (Year)	D ₅₀ (mm)	H/D ₅₀	τ_{cr}^*	Actual Froude Number	Froude Number Eq. 2.10	% Error
Ashida & Bayazit (1973)	22.5	4.07	0.0431	1.29	0.81	-37.2
Ashida & Bayazit (1973)	22.5	1.58	0.0527	1.77	0.93	-47.5
Ashida & Bayazit (1973)	22.5	1.11	0.0607	1.98	0.98	-50.5
Ashida & Bayazit (1973)	22.5	0.96	0.0743	-	-	-
Ashida & Bayazit (1973)	22.5	0.68	0.0894	2.57	1.13	-56.0
Ashida & Bayazit (1973)	22.5	0.58	0.1178	1.83	1.29	-29.5
Ashida & Bayazit (1973)	12	8.13	0.0402	0.71	0.71	0
Ashida & Bayazit (1973)	12	3.04	0.0427	1.14	0.82	-28.1
Ashida & Bayazit (1973)	12	1.71	0.0535	-	-	-
Ashida & Bayazit (1973)	12	1.21	0.0608	-	-	-
Ashida & Bayazit (1973)	12	1.00	0.0691	1.03	1.02	-0.97
Ashida & Bayazit (1973)	12	0.96	0.0846	0.91	1.13	+24.2
Ashida & Bayazit (1973)	6.4	8.52	0.0386	0.82	0.70	-14.6
Ashida & Bayazit (1973)	6.4	3.75	0.0461	1.03	0.85	-17.5
Ashida & Bayazit (1973)	6.4	2.03	0.0546	0.92	0.95	+3.26
Bathurst et al. (1982)	22	3.64	0.076	1.31	1.05	-19.8
Bathurst et al. (1982)	22	2.64	0.096	1.29	1.22	-5.43
Bathurst et al. (1982)	22	2.05	0.108	1.10	1.32	+20.0
Bathurst et al. (1982)	22	1.55	0.108	1.23	1.33	+8.13

Table 2.1 Summary of data from previous research in incipient motion under shallow flow conditions (continued).

Author (Year)	D ₅₀ (mm)	H/D ₅₀	τ_{cr}^*	Actual Froude Number	Froude Number Eq. 2.10	% Diff.
Suszka (1987)	12.2	13.5	0.0335	-	-	-
Suszka (1987)	12.2	11.0	0.044	-	-	-
Suszka (1987)	12.2	8.65	0.043	-	-	-
Suszka (1987)	12.2	8.20	0.045	-	-	-
Suszka (1987)	23.5	6.50	0.0525	-	-	-
Suszka (1987)	23.5	5.00	0.057	-	-	-
Suszka (1987)	23.5	4.10	0.062	-	-	-
Cao (1985)	22.2	8.60	0.051	-	-	-
Cao (1985)	22.2	3.50	0.069	-	-	-
Cao (1985)	22.2	2.40	0.076	-	-	-
Cao (1985)	22.2	1.80	0.096	-	-	-
Cao (1985)	22.2	1.40	0.098	-	-	-
Cao (1985)	44.5	3.00	0.049	-	-	-
Cao (1985)	44.5	1.90	0.064	-	-	-
Cao (1985)	44.5	1.30	0.070	-	-	-
Cao (1985)	44.5	1.20	0.090	-	-	-
Meyer-P and M (1948)	3.3	30.0	0.030	-	-	-
Meyer-P and M (1948)	28.6	17.0	0.046	-	-	-
Meyer-P and M (1948)	28.6	30.0	0.041	-	-	-
Meyer-P and M (1948)	28.6	40.0	0.050	-	-	-
USWES (1935)	4.1	19.0	0.0315	-	-	-
USWES (1935)	4.1	15.0	0.0360	-	-	-
USWES (1935)	4.1	15.0	0.041	-	-	-
Ho Pang Yung (1939)	4.1	50.0	0.034	-	-	-
Ho Pang Yung (1939)	4.1	20.0	0.032	-	-	-
Ho Pang Yung (1939)	6.1	15.0	0.040	-	-	-
Ho Pang Yung (1939)	6.1	19.0	0.0325	-	-	-

Table 2.2 Summary of equations for threshold conditions in mountain rivers with shallow flows.

Author (Year)	Range of D_{50} (mm)	Range of H/D_{50}	Range of Slopes (%)	Equation
Ashida and Bayazit (1973) Mizuyama (1977)	6.4-22.5 natural gravel	0.58-8.5	1-20	For $H/D_{50} \leq 4.55$: $\tau_{cr}^* = 0.034 \times 10^{0.32(D_{50}/H)}$ For $H/D_{50} \geq 4.55$: $\tau_{cr}^* = 0.04$
Suszka (1991)	3.3-44.5 natural gravel	1.2-50	0.17-9	$\tau_{cr}^* = 0.0851 \left(\frac{H}{D_{50}} \right)^{-0.266}$
Bathurst et al. (1982)	22 natural gravel	1.55-3.64	3-9	None
Graf and Suszka (1987)	5.5-44.5 natural gravel	0.58-13.5	0.5-20	For $S \leq 2.5\%$: $\tau_{cr}^* = 0.045$ For $S \geq 2.5\%$: $\tau_{cr}^* = 0.042(10^{2.2S})$
Abt et al. (1988)	25.4-152.4	0.48-2.01	1-20	None
Bettess (1984)	N/A*	N/A	N/A	$\tau_{cr}^* = (\text{constant}) \times f \left(\frac{H}{k_s} \right)$ where $f(H/k_s) \rightarrow 1$ as H/k_s increases
Cheng (1969)	305 spheres	0.3-1.7	0-3.85	$\frac{\rho V_c^2}{(\gamma_s - \gamma_f) D_{50}} = 2.0 \left(\frac{D_{50}}{H} \right)^{2/3}$
Aguirre-Pe (1975)	50 mm cubes	not reported	up to 9.5%	$\tau_{cr}^* \left(\frac{\gamma_s - \gamma_f}{\gamma_f} \right)^{1.17} = (5.6 \times 10^{-11}) (\text{Re}_p^*)^{2.30}$
Aksoy (1973)	N/A	N/A	N/A	$\left(\frac{\rho_f}{\rho_s - \rho_f} \right) S = f \left[\left(\frac{D_{50}^{3/2}}{v} \sqrt{g \frac{\rho_s - \rho_f}{\rho_f}} \right) \frac{R_h}{D_{50}} \right]$
Wang and Shen (1985)	73.7-400 boulders	6.5-10.85	0.81-6	For $100 < \text{Re}_p^* < 1 \times 10^5$ $\tau_{cr}^* = 0.062$ For $\text{Re}_p^* > 10^5$ $\tau_{cr}^* = 0.25$
Kilgore & Young (1993)	4.1-400	not reported	not reported	$\tau_{cr}^* = 0.052(\text{Fr})^{2.7} + 0.05$
Grant (1997)	N/A	N/A	N/A	$Fr = 2.18 \left[\ln \left(1.65 \frac{\tau_{cr}^*}{S} \right) + 1.35 \right] \sqrt{S}$
Bartnik (1991)	3.1-70 natural gravel	7.86-322.6	0.2-3.5	$Fr_c = 1.35 \left(\frac{H}{D_{50}} \right)^{-0.35}$

* N/A (Not applicable)

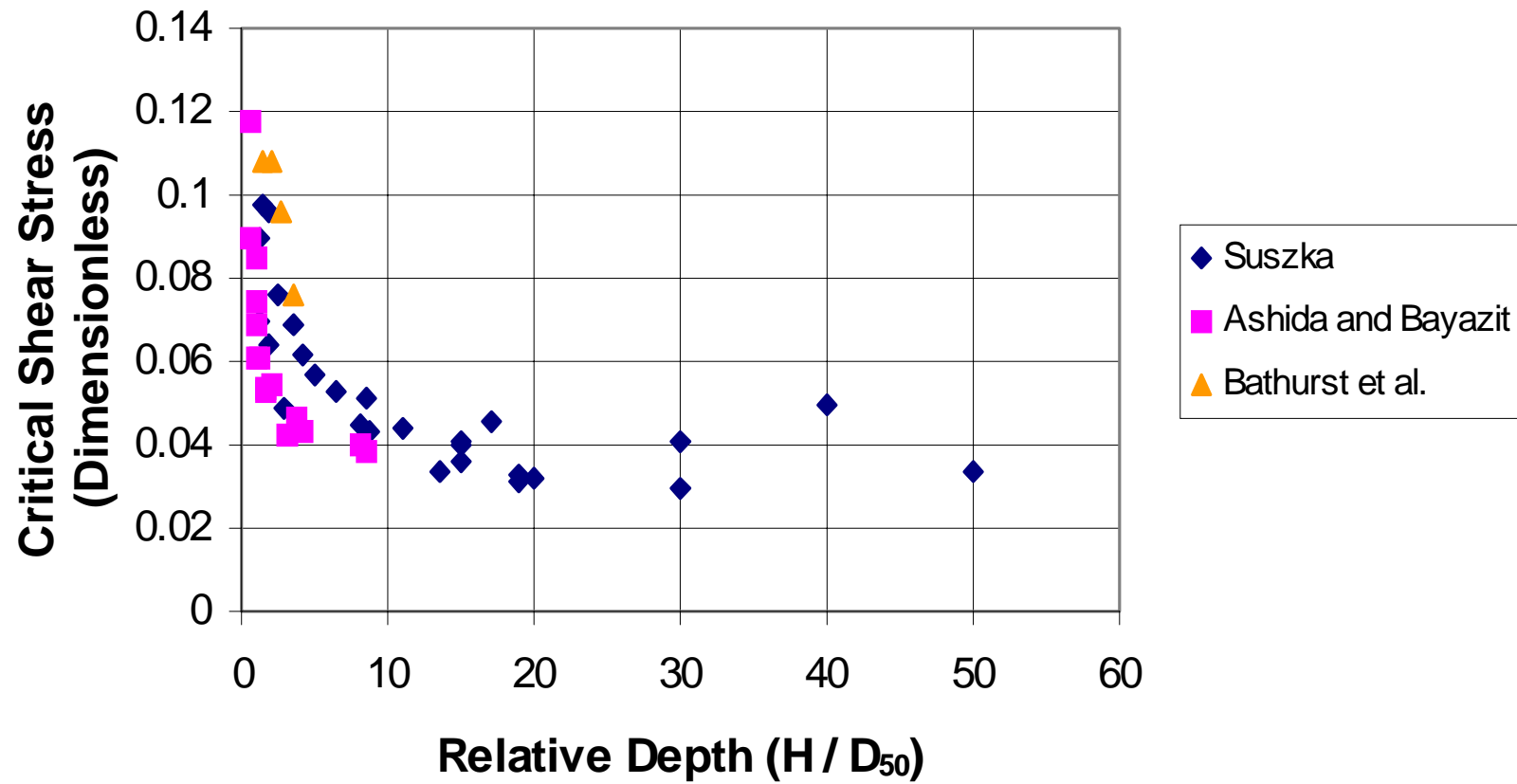


Figure 2.1 Plot of the dimensionless critical shear stress vs. relative depth using data from several previous investigators.

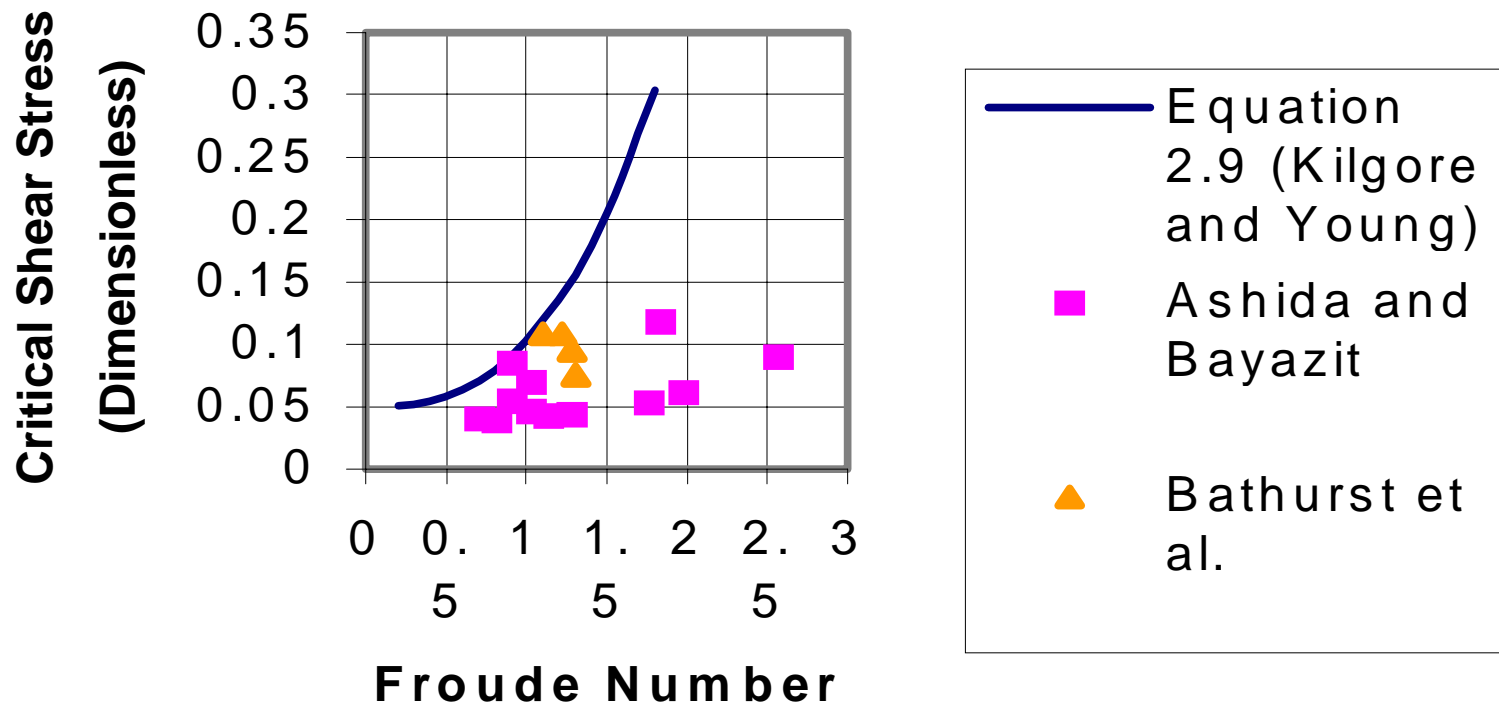


Figure 2.2 Plot of the dimensionless critical shear stress vs. Froude number using data from several previous investigators.

Chapter 3. Equipment

The experiments took place in the Kelso Baker Environmental Hydraulics Laboratory at the Virginia Polytechnic Institute and State University in Blacksburg, Virginia, USA. The main pieces of equipment used are the tilting flume, the spherical particles, the camcorder (movie camera), the plexiglass lid, and the laser-Doppler velocimeter (LDV) with all its associated peripherals. Each will be described in detail in this chapter.

3.1 Flume

The tilting flume, sketched in Figure 3.1, is of rectangular cross-section with plexiglass walls. It is 20.1 meters long, 0.6 m wide, and 0.3 m deep. The useful length, or main channel length, is 14.4 m long. This useful length has two sections, the natural gravel section and the glass bead section. The former is located at the upstream portion of the flume and is 10.4 m long. It consists of coarse natural gravel. The latter is located at the downstream portion of the flume and is 4 m long. It consists of 4 layers of well-packed, 8 mm diameter glass beads. The water enters the flume through a honeycomb structure whose purpose is to provide rectilinear flow. At the downstream end of the flume, it is discharged into an 11.3 m³ reservoir and is re-circulated by two centrifugal pumps. These pumps are of the closed impeller type and are rated at 7.5 hp. Pump No.1 is equipped with a transistor inverter variable frequency speed controller (Toshiba, Tosvert-130H1) for adjusting the water flow. Pump No.2 runs at a fixed speed. The outlet pipes from both pumps join an 8 inch diameter water supply line that runs underneath the main body of the flume and ends at the entrance. This water supply line includes a Venturi tube with a 3.6 in diameter throat. The Venturi tube is connected to a water/air and a mercury/water manometer for the calculation of flow rate. The calibration equations provided by the flume manufacturer are $Q = 0.00306\sqrt{\Delta h}$ for the water/air manometer and $Q = 0.0109\sqrt{\Delta h}$ for the mercury/water manometer, where Q = discharge in m³/s and Δh = head differential in cm. A knife-edge gate valve is located downstream of the Venturi tube. It serves as an additional flow-control device. Next to Pump No.1's frequency speed controller is the slope motor controller, which is used to adjust the flume's slope. The slope range is 0.0%-5.0%.

At the downstream end of the flume is a sediment trap. This trap collects the eroded sediment as the water enters the reservoir. A 0.5 hp sediment return pump that feeds sediment back upstream is available, but was not used for these experiments. Also available, but not used in this study, is a tail gate near the downstream end. A different method, discussed in Section 4.4.1, was used to maintain uniform flow conditions.

The flume is also equipped with rails upon which a trolley can slide. The trolley is convenient for placing a halogen light, which is useful because it improves the clarity of the image while filming an experiment. A bucket with water mixed with seeding material for the laser can also be mounted on this trolley. Yet another use for the trolley is to attach a pressure transducer and a Prandtl tube, but these devices were not used in this study.

3.2 Spherical Particles

The test particles used in this study are balls, 8 mm in diameter. Four types of particles of different density are used in order to obtain a wide range of Froude number values. These are viton (Specific Gravity, $SG = 1.83$), which is a type of rubber, teflon ($SG = 2.11$), glass ($SG = 2.59$), and aluminum oxide ($SG = 3.80$), a ceramic. Of the 4 types, the aluminum oxide (Al_2O_3) particles are by far the most expensive and hardest to find. They were purchased from Hoover Precision Products, Inc. in Marie, Michigan. Additionally, lead balls ($SG = 11$) are used upstream and downstream of the test section. Table 3.1 summarizes general information about the particles. This summary table includes the color of each ball. The teflon and ceramic balls come in white from the manufacturer and are easily recognizable in the experiment videos. However, the glass balls are transparent and the test particles cannot be distinguished from the bed, which is composed of the same type of material. Also, viton is black and does not look very good in the movies. Therefore, the glass and viton balls are painted using a special water-resistant paint manufactured by Dykem Co. of St. Louis, Missouri.

3.3 Movie Camera

It is necessary to keep a recording of each experiment as part of the procedure for the incipient motion criterion described in Section 4.2, as well as for future reference.

Each experiment at threshold conditions is taped using a General Electric 9-9806 camcorder. The camcorder is mounted on a tripod directly above the test section. The lens of the camera faces directly down and is approximately 0.75 m above the bed. The area of view captured is 0.4 m by 0.4 m. A halogen light facing the test section is placed about 0.6 m upstream of the movie camera. A sketch of this setup is shown in Figure 3.2.

3.4 Plexiglass Lid

Although the focus of this study is in free surface flows, several of the experiments are performed under pressurized flow conditions. A plexiglass lid is used to pressurize the flow. The lid is 2.44 m long, 0.594 m wide, and 1.27 cm thick. The length was chosen to be at least 20 times greater than the deepest planned flow, to allow for fully developed turbulent flow conditions. Although the flume is 0.6 m wide, a clearance of 0.003 m was given on each side of the lid to allow it to slide up and down smoothly. This clearance is tight enough to prevent water from seeping through the sides during the experiments. The lid structure, sketched in Figure 3.3, contains 8 threaded rods that allow the lid to move vertically. Each threaded rod contains a wing nut used to lock the lid at the desired position above the bed. It is desirable to always keep the lid parallel to the channel bed. The structure is supported by four wooden boards, which sit on the flume wall's rails. Attached to the lid's upstream end is an 8.5 cm diameter half-pipe, which allows the water to enter the pressurized area smoothly without separation.

3.5 The LDV System

Laser-Doppler velocimetry is a non-intrusive technique used to measure flow velocities. The non-intrusive nature of the LDV is beneficial when taking measurements at threshold conditions. The system used was modified for 2 components using the two strongest beams, green (514.5 nm) and blue (488 nm). A prism splits the main laser beam into the two colors. Each of the two color beams is split in two by a beam splitter resulting in a total of 4 beams. The two pairs of beams are orthogonal. The orientation of the beams relative to the test section is shown in Figure 3.3. The system was operating in a direct back-scatter mode. A refractive index correction factor was used due to the air gap that the beams go through before entering the flow. The entire laser system is

mounted on a traverse table (TSI, Model 9500) that can move in three directions. The table is rotated 4.8° to allow measurements very close to the bed. Therefore, the fluctuating component of the velocity in the vertical direction, v' , is measured at an orientation of 4.8° from the z-axis. The flow was seeded with four-micron diameter silicon carbide (SiC) seed. Balakrishnan (1997) investigated a wide range of seed sizes and found the $4\ \mu\text{m}$ seed to produce the highest quality signal and data rate. Frequency shifters were used on both channels to avoid angular bias. The frequency shift was kept 2-4 times the Doppler signal frequency. The processing consisted of counters. The count was made on 8 fringes with 1 % comparison. The TSI Find software package was used for the signal analysis.

Table 3.1 Characteristics of the Spherical Particles Used in the Experiments.

Ball Material	Color	Diameter (mm)	Specific Gravity
Viton	Yellow	8	1.83
Teflon	White	8	2.11
Glass	Green	8	2.59
Ceramic (Al_2O_3)	White	8	3.80
Lead	-	8	11

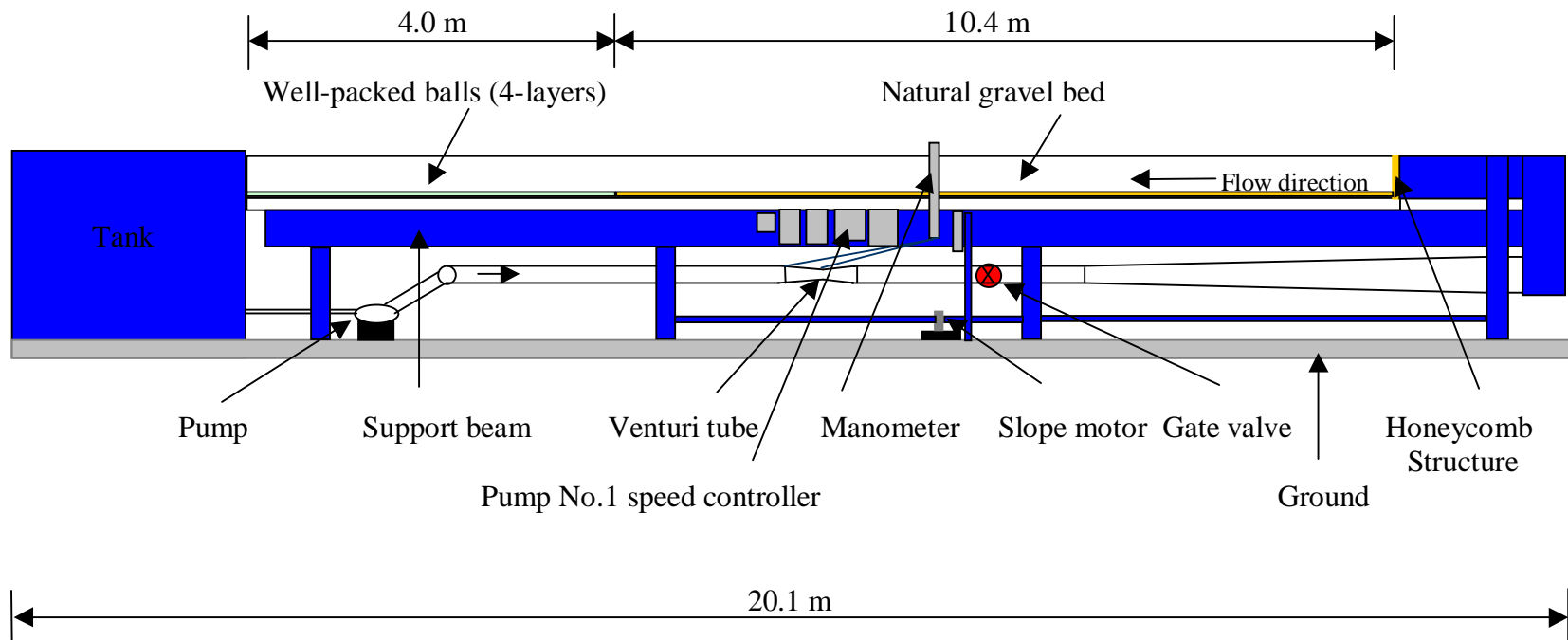


Figure 3.1 Schematic of the flume.

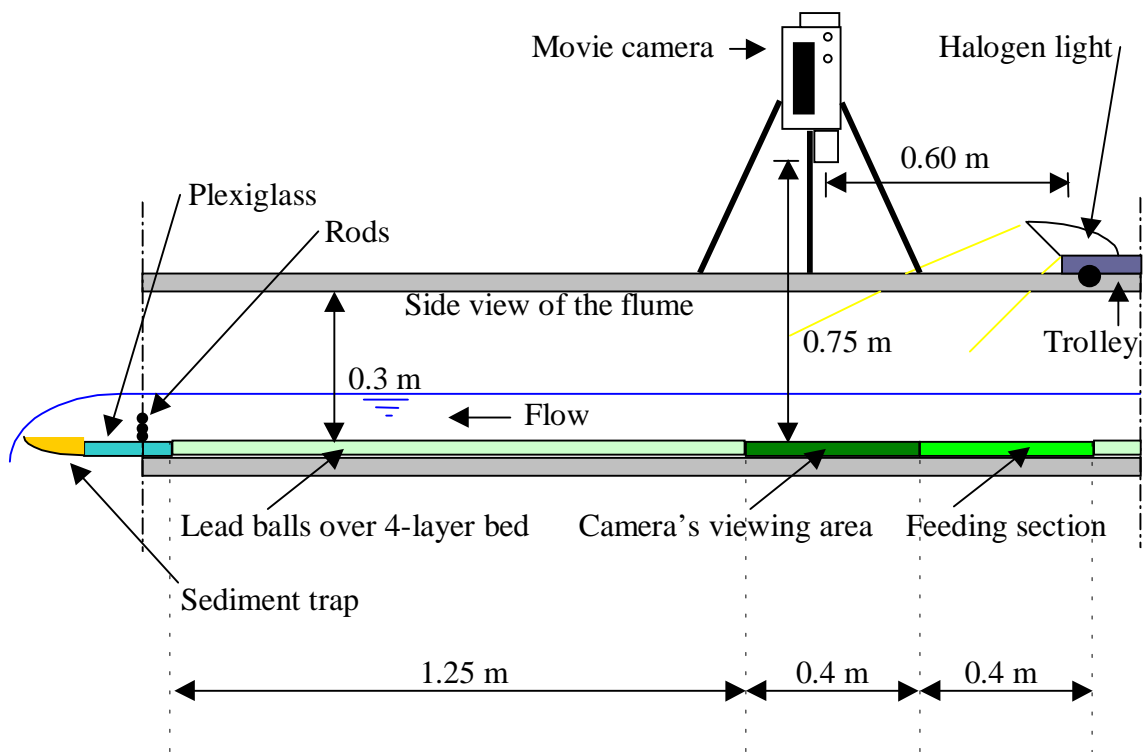
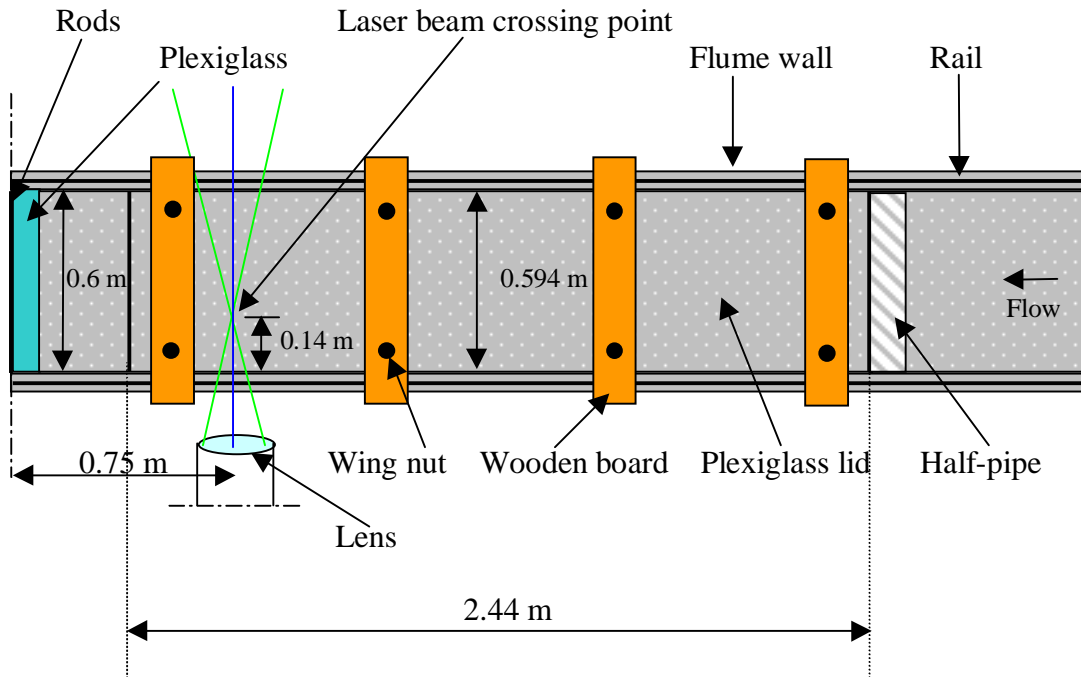


Figure 3.2 The filming process.

Plan View



Side View

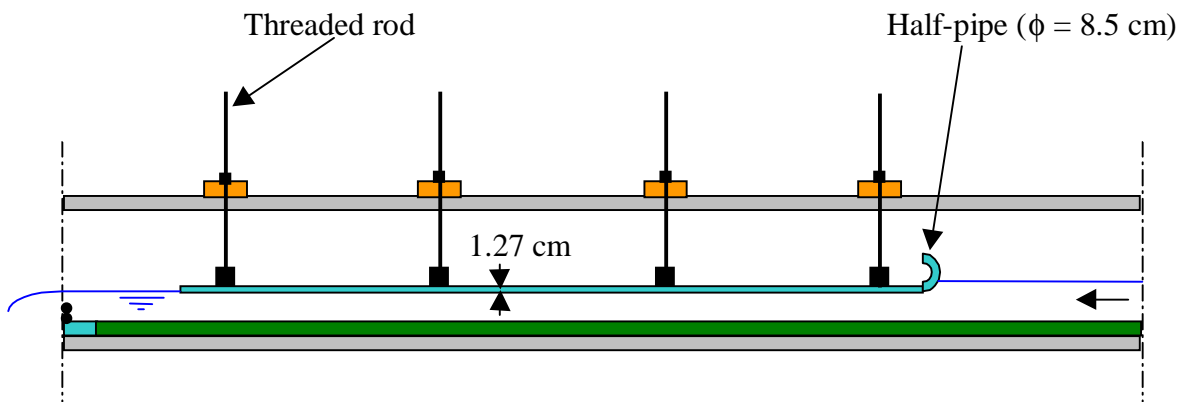


Figure 3.3 The lid structure (sketch).

Chapter 4. Methodology

4.1 Dimensional Analysis

As stated in Section 1.6, a modified version of the Shields diagram shows the dimensionless critical shear stress as a function of relative depth. In Section 1.4 it was stated that the Froude number is important when an object is near the free surface. The relationship between τ_{cr}^* and these additional dimensionless terms can be shown by dimensional analysis. Adding the depth-averaged velocity, V , and flow depth, H , to the 5 terms in the dimensional analysis used as the basis for the traditional Shields diagram we have $f(\tau_{cr}, \rho, \mu, D_{50}, \gamma_s - \gamma_f, H, V) = 0$. The addition of the flow depth is especially important because of the degree of interaction with the free surface. By applying the Buckingham Π (Pi) theorem with ρ , H , and V as repeating variables and with some rearrangements, 4 dimensionless terms are obtained:

$$f \left(\frac{\tau_{cr}}{D_{50}(\gamma_s - \gamma_f)}, \frac{u_{cr}^* D_{50}}{v}, \frac{H}{D_{50}}, \frac{V^2}{gH \left(\frac{\rho_s}{\rho_f} - 1 \right)} \right) = 0 \quad (4.1)$$

where g = acceleration due to gravity and ρ_s = density of the sediment particles. The first 2 dimensionless terms are the ones seen in the traditional Shields diagram. The third term is the relative depth mentioned in Section 1.6 and the last term is the densimetric Froude number, Fr_D . This term is commonly used when the flow involves two densities, as is the case with massive bedload or high sediment suspension. The regular Froude number might be more appropriate in this study. The actual functional relationship between the dimensionless parameters is determined by running experiments. As mentioned earlier, the particles used in this study are coarse, so the dimensionless critical shear stress is independent of the particle Reynolds number.

4.2 Criterion for Incipient Motion

4.2.1 The Concept of Probability of Entrainment in a Bursting Period

In order to run experiments at incipient conditions, a well-defined criterion must be established and applied consistently throughout the experimental phase. A common

approach of measuring the dimensionless threshold stress is by applying different fluid stresses to a bed and measuring the corresponding bed-load discharges by collecting the sediment removed by entrainment. Subsequently, the critical shear stress is obtained by extrapolation to zero transport. Several researchers (Shields 1936 ; Paintal 1971 ; Taylor and Vanoni 1972) have used this approach. Observations of incipient motion experiments have shown that in some cases the amount of sediment collected in a trap can be relatively small while the motion of sediment particles over an area is significant and occurs sporadically at different spots of the bed. Papanicolaou (1997) proposed a method which accounts for the “first displacement” of particles over an area rather than the number of balls crossing a line. Fenton and Abbott (1977) defined the “first displacement” as a dislodgment of a particle from its original position. The method developed by Papanicolaou is used in this study and will be described in the remaining paragraphs of Section 4.2.

The main goal of this method is to find the probability of particle entrainment, P_E , in an area of view during a bursting cycle, since it is suggested that bursting is the mechanism responsible for the beginning of sediment motion. The bursting cycle is sporadic in nature. A camcorder set directly above the test section is used to obtain P_E . The fraction of particles displaced is equal to the ratio N_E/N_T , where N_E = the number of particles entrained in a period Δt_i and N_T = the total number of particles in the camera’s viewing area at the beginning of the time period Δt_i . The frequency of particle displacement, f_i , is equal to the fraction of particle displacement per unit time or

$$f_i = \frac{N_E}{N_T} \frac{1}{\Delta t_i} \quad (4.2).$$

Each time period Δt_i in this study is one minute and most experiments have a total duration of 20 minutes. The total duration of an experiment can be chosen to be any amount of time as long as the packing conditions in the test section at the end of the experiment are not too different from the conditions in the beginning of the test. The reason for this is that the dimensionless critical shear stress is strongly dependent on packing conditions, so the tests must be consistent. The average frequency of particle displacement, f_{avg} , for k subsequent time periods Δt_i , is given by

$$f_{avg} = \frac{\sum_{i=1}^k f_i}{k \times \Delta t_i} \quad (4.3).$$

During a bursting period, T_B , the probability of particle entrainment, P_E , in the area of view is computed as

$$P_E = f_{avg} T_B \quad (4.4).$$

A widely used expression for the mean bursting period is that defined by Cantwell (1981) as,

$$T_B = 6 \frac{H}{V} \quad (4.5).$$

For the experiments to be equivalent in terms of incipient conditions, a consistent probability of entrainment must be maintained. In this study, most of the experiments are within $\pm 20\%$ of the probability of entrainment selected as the critical one, P_{Ecrit} .

4.2.2 Selection of a Critical Probability of Entrainment

For the deeper flows, values of T_B are high while for shallow flows they are low. Therefore, to maintain consistent values of P_E , the average frequency of particle displacement for the shallow flows is significantly higher than the frequency for the deeper flows. Thus, a very stringent P_{Ecrit} was chosen in order to avoid massive motion in the experiments with steep slopes and shallow flows. In the steeper flows, the particles are extremely sensitive and highly unstable. When higher values of P_{Ecrit} were tried, most of the particles in the test section were eroded within a few minutes. Such experiments were extremely sloppy and could not be considered for use. After a trial-and-error procedure the criterion for threshold conditions was chosen to be $P_{Ecrit} = 1.014 \times 10^{-4}$. This is the probability of entrainment for experiment A1 (viton balls at $H/D_{50} = 2$), which happens to be the most sensitive case, because it involves the lightest ball and the lowest relative depth. In all the experiments that were within $\pm 20\%$ of P_{Ecrit} , both deep and shallow, the motion of the particles was sporadic and the packing conditions after 15-20 minutes were similar to the packing conditions at the beginning of the test.

4.2.3 The Trial-and-Error Procedure

Table 4.1 is an example of the method discussed in this section. This type of table is created for every run of a trial-and-error procedure. It shows the fraction of particles being displaced every minute during the 15 or 20 minutes of the test and also shows the average frequency of particle displacement. A displacement can be as small as less than a particle diameter or can be large enough for the particle to roll far beyond the area of view. When particles roll beyond or into the area of view, N_T is adjusted accordingly. In this study, displacements are observed by carefully watching the 15-20 minute video of each experiment. Sophisticated image processing software that accurately counts the displacements has been recently developed (Papanicolaou 1997), but is not used here.

Several guidelines were established for counting particle displacements. First, if a particle moves twice, it is counted twice only if 10 seconds have elapsed between motions. This is done to allow the particle plenty of time to stabilize. Second, if a particle moves into the viewing screen and then moves again after 10 seconds, it is counted only if the second motion occurs in the next time period, Δt_i . This is done because a particle counts as part of the total, N_T , only if it was present in the viewing area in the beginning of that one-minute time period. Third, only the particles that were entrained by the fluid forces are counted. If a particle is entrained because it was hit by another particle, it is not counted. Finally, a particle is only counted as part of the total if it is fully inside the viewing screen. Although some of these guidelines might be different than those followed by image processing software, they were applied consistently throughout the experimental phase.

After P_E is computed for that particular run, it is compared to P_{Ecrit} . The test is repeated with the same relative depth, but a different slope if P_E is not within $\pm 20\%$ of P_{Ecrit} . This approach is independent of the availability of particles in the test section because it is based on the fraction of particles displaced rather than the number of particles displaced. Tables similar to Table 4.1 are available in Appendix 1 for all the incipient motion experiments in this study.

4.3 Experimental Setup

The shallow flow data mentioned in Chapters 1 & 2 (Ashida and Bayazit 1973; Mizuyama 1977; Bathurst et al. 1982; Suszka 1991) come from experiments using natural gravel beds. In this study, the bed is composed of 4 layers of well-packed, 8 mm diameter, transparent glass beads. The test particles lie on top of these 4 layers and have a different color in order to be recognized when viewed in the video. These particles are loosely packed making up only 2% of the total area in the test section. This is typically known as the 2% packing condition. The average lateral distance between balls in this case is about 6 ball diameters. The diagonal distance is shorter. Figure 4.1 shows a sketch of the plan view and side view of this setup.

Spherical grains are not common in natural streams. However, the use of natural gravel for these experiments would complicate the situation because incipient motion is strongly dependent on protrusion effects (Fenton and Abbott 1977), packing conditions (Papanicolaou 1997), and shape of the particles (Moore 1994). Here, the angle of repose, shape, and packing conditions of the test particles do not vary from experiment to experiment. These well-controlled conditions allow for the isolation of the free surface effects on the incipient motion of the particles.

The test section is located near the downstream end of the flume where fully developed turbulent flow conditions exist. It is 0.8 m long and 0.4 m wide. The area of view captured by the camera is 0.4 m by 0.4 m. A feeding area of the same dimensions is located upstream of the camera's viewing area. For 2% packing conditions 128 spherical particles are placed in the test section and 64 should appear in the camera's viewing area before the test starts. During an experiment at threshold conditions, that number may not be 64, since particles can move into and out of the area of view.

In Section 3.1, it was mentioned that the section of the flume's bed that is composed of well-packed glass balls is 4 m long. The test section is 0.8 m long. As shown in Figure 4.2, the rest of the 4 m stretch contains non-movable lead balls also spread at a 2% packing density. The presence of the lead balls helps maintain similar conditions upstream and downstream of the test section. The whole 4 m stretch can be filled with movable particles, but this would add to the tedious task of fixing the movable bed after each experiment. The camera must be placed at the downstream end of the test

section. This is done in order to have a feeding section upstream that replaces particles that have moved downstream, away from the camera's area of view. Lead balls are also placed on the sides of the test section, in a 0.1 m wide strip near the wall of the flume on both sides. The region close to the wall should not be used as part of the test section because the particles in that area experience the effects of the side wall.

4.4 Experimental Procedure

4.4.1 Running Experiments at Threshold Conditions

The loosely packed movable spherical particles are extremely sensitive in the presence of the flowing water, especially in the steeper slopes. Therefore, the pump speed must be increased slowly. If not, the test particles could be wiped out before incipient conditions are reached. If done too slowly, the particles will be exposed to the turbulent fluctuations for too long and the number of test particles can also be significantly reduced before incipient conditions are reached. The right speed is gained through experience. The main goal is to have conditions similar to the ones shown in Figure 4.1 when threshold conditions are reached. Another issue concerning the sensitivity of the particles is the uniformity of the flow. Some preliminary experiments showed that massive motion occurs at shear stresses below critical under M2 water-surface profiles. On the other hand, very little motion occurs at shear stresses above critical under M1 profiles. This issue will be discussed further in Section 5.2.3. With this sensitivity issue in mind, it is very important to maintain uniform flow in all the runs. This is achieved by placing rods at the downstream end of the flume, as shown in Figure 3.2, and by providing similar roughness downstream of the test section via the lead balls. The number of rods used in each experiment is provided in Appendix 1.

Initially, the goal was to run experiments at incipient conditions at relative depths ranging from $H/D_{50} = 2$ through 12 for all 4 types of test particles mentioned in Section 3.2. However, this proved to be impossible for the two lighter balls, viton and teflon. For instance, when running an experiment with viton balls at $H/D_{50} = 7$, the motion exceeded that required by critical conditions no matter how low the slope. The main cause for this is that balls of such a low density ($SG = 1.83$) are very sensitive. The slow and deep flows they are exposed to produce long bursting periods. Referring back to Eq. 4.4 it can

be seen that if the bursting period is too high, then a low average frequency of particle displacement, f_{avg} , is needed to meet the required P_{Ecrit} . A low requirement for f_{avg} can prevent some cases from running successfully.

After successfully running a test at threshold conditions, the Shields parameter or dimensionless critical shear stress can be calculated. It is the first term in Eq. 1.1 and is expressed as

$$\tau_{cr}^* = \frac{\tau_{cr}}{D_{50}(\gamma_s - \gamma_f)} \quad (4.6).$$

Substituting with the expression for shear stress in the bed of open channels, $\tau_{cr} = \gamma_f HS$, and the expression for the submerged specific gravity of a particle, $R = (\gamma_s - \gamma_f)/\gamma_f$, Eq. 4-6 is simplified. Thus

$$\tau_{cr}^* = \frac{HS}{RD_{50}} \quad (4.7).$$

This is the expression used in this study, although τ_{cr} can also be obtained from the Reynolds stresses provided by the laser-Doppler velocimeter (LDV). However, the LDV was used for only a portion of the experiments, so Eq. 4.7 is preferred. It will be shown in Section 6.1 that equation 4.7 is a very good approximation of equation 4.6. For the same reason, the continuity equation is used to obtain the depth-averaged velocity instead of integrating the velocity profile. The incipient motion results are discussed in detail in Chapter 5.

4.4.2 Velocity Profiles

The velocity profiles are taken separately after the parameters for threshold conditions are known. Lead balls are used in the test section in place of the movable test particles. In a movable bed, balls can roll into and block the laser beams. Also, a high-quality velocity profile can take a few hours. By the time the profile is complete, the bed can be partly eroded. Therefore, it is advantageous to use non-movable balls when using the LDV. This study includes the velocity profiles for most of the glass ball experiments, for two supercritical flows, and for five pressurized flows. The results and analysis of the laser experiments are discussed in detail in Chapter 6.

Table 4.1 Frequency of particle displacements at threshold conditions for experiment B3 (glass balls $H/D_{50} = 3$).

Time Period, Δt_i (minutes)	Fraction Displaced N_E/N_T	Fraction Displaced N_E/N_T (decimal)	Frequency of Displacement, f_i (1/s)
0-1	2/68	0.029411765	0.000490196
1-2	2/68	0.029411765	0.000490196
2-3	5/67	0.074626866	0.001243781
3-4	0/67	0	0
4-5	0/67	0	0
5-6	2/67	0.029850746	0.000497512
6-7	0/67	0	0
7-8	0/67	0	0
8-9	3/67	0.044776119	0.000746269
9-10	0/66	0	0
10-11	2/66	0.03030303	0.000505051
11-12	0/66	0	0
12-13	0/66	0	0
13-14	0/66	0	0
14-15	0/66	0	0
15-16	1/66	0.015151515	0.000252525
16-17	0/66	0	0
17-18	2/66	0.03030303	0.000505051
18-19	1/66	0.015151515	0.000252525
19-20	3/66	0.045454545	0.000757576

$$f_{\text{avg}} = 2.87 \times 10^{-4}$$

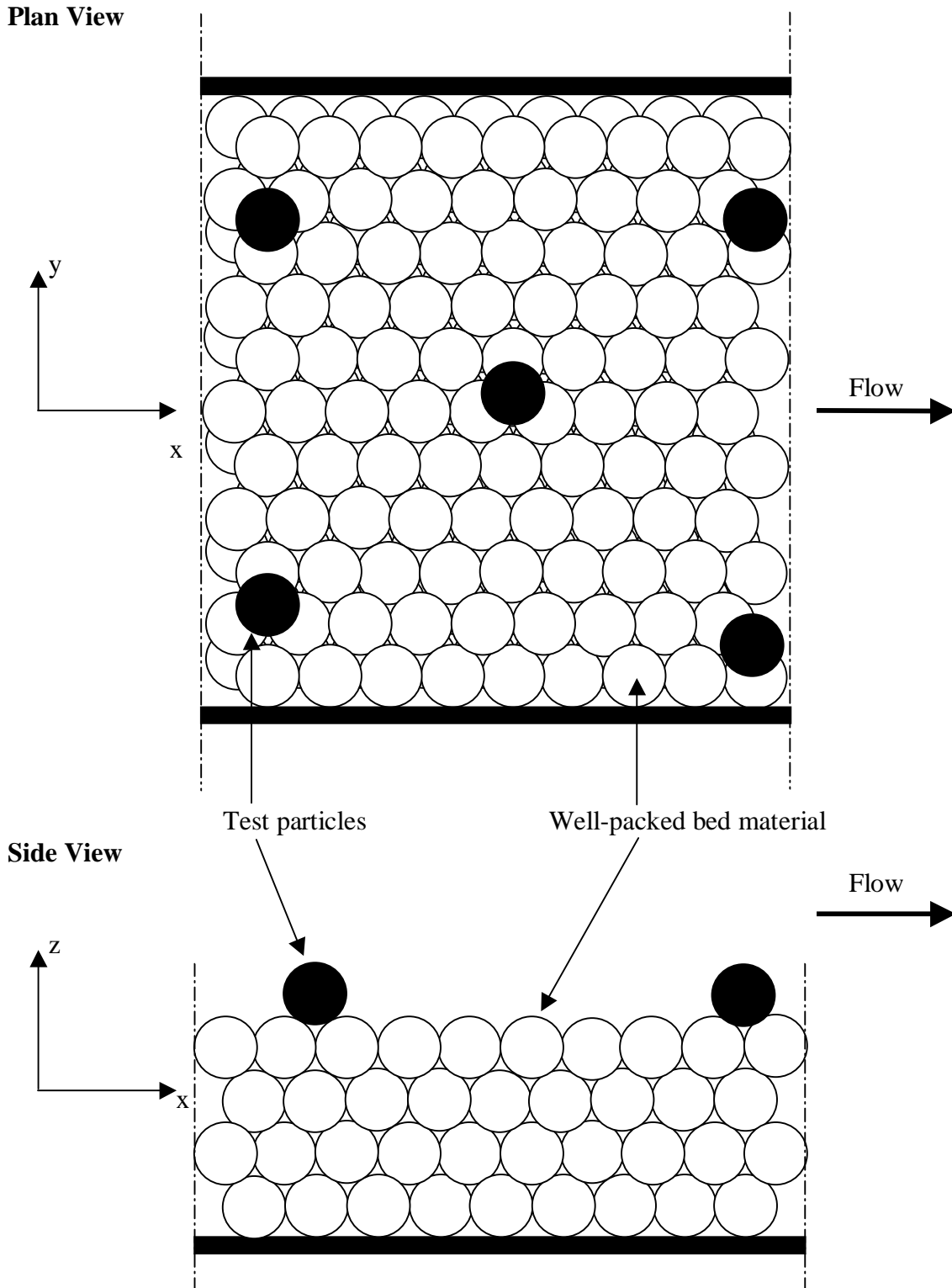


Figure 4.1 The 2% packing condition. Test particles on top of the well-packed, 4-layer bed (sketch).

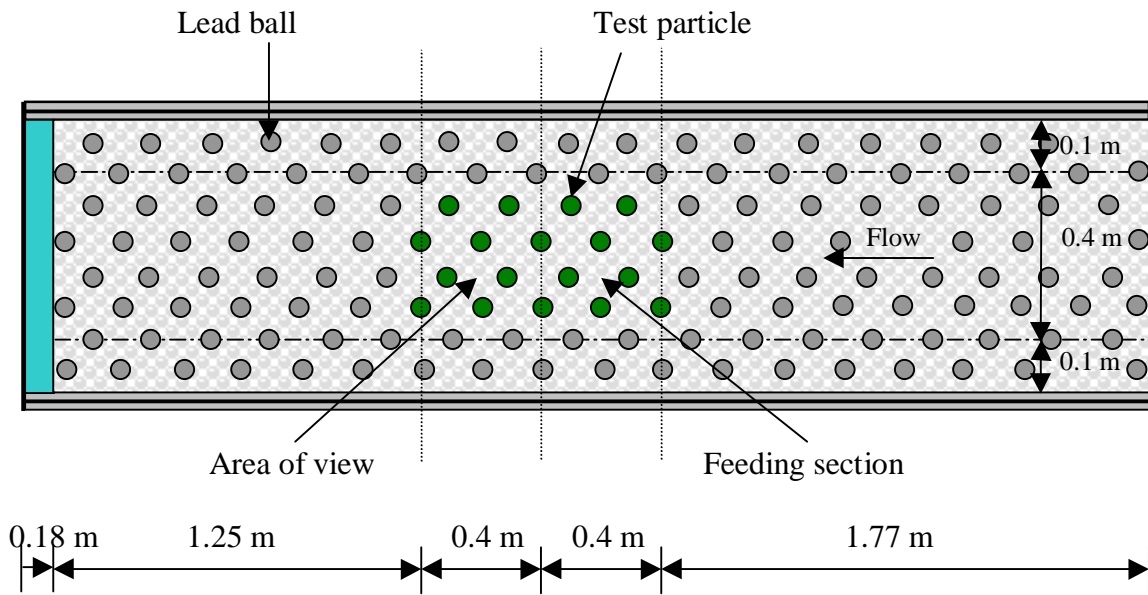


Figure 4.2 The test section (sketch).

Chapter 5. Results and Analysis of Experiments

5.1 Summary Tables

A total of 34 experiments were run at threshold conditions. Of this total, 29 are at uniform flow and most of the time within $\pm 20\%$ of P_{Ecrit} , 3 are with an M1 water-surface profile and within $\pm 20\%$ of P_{Ecrit} , and 2 are at uniform flow, but the bursting period is not considered in the criterion for incipient conditions. This section will focus on the 29 experiments at uniform flow. The 2 experiments that don't consider T_B and the 3 with the M1 curve will be discussed in detail in Sections 5.2.2 and 5.2.3, respectively.

In Section 4.4, it was mentioned that it is not possible to have very high relative depths for the two lightest particles. Table 5.1 summarizes the range of relative depths tested for each of the 4 types of particles as well as the range of slopes, Froude numbers, densimetric Froude numbers, and dimensionless critical shear stresses. Table 5.2 summarizes the results for all 29 uniform flow experiments. As shown in this table, several experiments have high Froude numbers, but only 2 are supercritical. Table 5.3 summarizes the information related to threshold conditions, such as the number of balls displaced in the 20 minute testing period, the average frequency of particle displacement, f_{avg} , the bursting period, T_B , and the probability of entrainment in a bursting period, P_E . The values of T_B for the $H/D_{50} = 2$ case, ranging from 0.19-0.35 seconds, are considerably lower than the values for the $H/D_{50} = 10$ case, which range from 0.95-1.32 seconds. This is due to the fact that at low relative depths the velocities are higher and obviously, depths are lower. This table also includes how f_{avg} and P_E for each experiment compare to the critical values of f_{avg} and P_E . As mentioned in Section 4.2.2, $P_{\text{Ecrit}} = 1.014 \times 10^{-4}$. The value for the critical frequency of particle displacement is $f_{\text{avg_crit}} = 2.89 \times 10^{-4}$ 1/s. Earlier, it was mentioned that these critical values come from the viton ball experiment at $H/D_{50} = 2$. Since the bursting period increases with increasing relative depth, the average frequency of particle displacement must decrease so that P_E can stay within $\pm 20\%$ of P_{Ecrit} . This explains why the number of particles displaced varies from 6-26 at threshold conditions.

Finally, as mentioned in Section 4.2.3, a table similar to Table 4.1 is provided in Appendix 1 for all the experiments. This table includes the fraction of particles displaced for every minute during the experiment. Appendix 1 also contains other useful

information for each experiment such as the head differential, Δh , obtained from the manometer, the water discharge, Q , the amount of rods used to maintain uniform flow conditions, the pump speed, the water depth, and the information in Tables 5.1-5.3. Each experiment is labeled by a letter and number. The letter A corresponds to $H/D_{50} = 2$, B corresponds to $H/D_{50} = 3$, and so on. The number 1 corresponds to teflon balls, 2 corresponds to viton balls, 3 corresponds to glass balls, and 4 corresponds to ceramic balls. For example, experiment E4 corresponds to ceramic balls at $H/D_{50} = 6$. The experiments that don't consider T_B and those with M1 profiles are labeled the same way but with "T_B" or "M1" next to the label, accordingly.

5.2 Analysis of Results

5.2.1 The Modified Shields Diagram

Figure 2.1 in Chapter 2 showed the relationship between the dimensionless critical shear stress and the relative depth, H/D_{50} , using the data of Ashida and Bayazit (1973), Bathurst et al. (1982), and Suszka (1991). Figures 5.1-5.4 show the same relationship, but include the effects of the densimetric Froude number as well. The curves shown were created using the 29 experiments discussed in Section 5.1 and tabulated in Table 5.2. Figures 5.1, 5.2, 5.3, and 5.4 are plots for the viton, teflon, glass, and ceramic balls, respectively. The most complete set is Figure 5.3 (glass balls) because it covers the widest range of relative depth, $H/D_{50} = 2-12$. The dimensionless critical shear stresses for the $H/D_{50} = 10$ and 12 cases are identical. However, a slightly higher dimensionless critical shear stress corresponds to the $H/D_{50} = 8$ case. Thus, the dimensionless critical shear stress is dependent on the relative depth at approximately $H/D_{50} < 10$. This result is similar to what was predicted by the data of the previous researchers shown in Figure 2.1. In the relative depth dependence region, the dimensionless critical shear stress increases as H/D_{50} decreases. In the region which is independent of the relative depth, the dimensionless critical shear stress is $\tau_{cr}^* = 0.00566$. This value is considerably lower than that seen in the Reynolds number independent region of the traditional Shields diagram or in Figure 2.1. This is due to the stringent criterion for incipient motion used and the fact that the particles stand above the bed and are fully exposed to the flow.

Figure 5.3 also shows a strong densimetric Froude number dependence. The dimensionless critical shear stress is dependent on the densimetric Froude number at approximately $Fr_D > 0.40$. In the densimetric Froude number dependence region, the dimensionless critical shear stress increases as Fr_D increases. Similar results can be seen in Figure 5.4 for the ceramic ball data. Figures 5.1 (viton) and 5.2 (teflon) do not have the wide range of relative depths that Figures 5.3 (glass) and 5.4 (ceramic) have. Therefore, exactly where the H/D_{50} and Fr_D dependence begins is somewhat questionable. However, the trends are similar. All 4 figures show that the most dramatic increase in dimensionless critical shear stress is between $H/D_{50} = 4$ and $H/D_{50} = 2$. Above $H/D_{50} = 4$ it starts leveling off. Although the data for viton and teflon balls is limited, it can be seen that the densimetric Froude number dependence begins somewhere between 0.35 and 0.4.

The four curves presented in Figures 5.1-5.4 are shown in one single plot in Figure 5.5. For the glass and ceramic balls, the constant dimensionless critical shear stress in the H/D_{50} and Fr_D independent region is about the same, in the vicinity of $\tau_{cr}^* = 0.006$. However, this value is considerably lower for the other two types of balls. It appears that it will be in the vicinity of $\tau_{cr}^* = 0.001$ for the viton balls. This contradicts the original Shields diagram, which shows that the data follow a constant dimensionless critical shear stress in the Reynolds number independent region regardless of the density of the particle used. The criterion for incipient motion used in this study may offer an explanation for this behavior. Also, as discussed in Section 2.1.1, a few researchers have noticed a dependence of τ_{cr}^* with particle density. Knowledge of the critical conditions of particles with a wide variety of densities is important in river beds with some unusual deposits.

Figure 5.6 is similar to 5.5, but has the Froude number in the x-axis instead of the densimetric Froude number. The curves in Figure 5.5 are distinct whereas in Figure 5.6 they tend to cross into one another a few times. However, the trends are similar. For shallow flows, or the Froude number dependent region, the dimensionless critical shear stress increases as the Froude number increases. These results are similar to those obtained by Kilgore and Young (1993). In Figure 5.6 it appears that the Froude number dependence is at about $Fr > 0.4$ for the viton and teflon balls, and at about $Fr > 0.5$ for the glass and ceramic balls. According to the Kilgore and Young data, the dependence occurs

at $Fr > 0.4$. Figure 5.7 shows the 4 curves for τ_{cr}^* as a function of relative depth. The H/D_{50} and Froude number dependent regions discussed in this section are due to the presence of the free surface.

Figure 5.8 contains the same data as in Figure 5.5. Curves of constant H/D_{50} are plotted instead of curves of constant particle density, as is the case in Figure 5.5. The obvious trend is that the curves tend to line up. For the most part, curves of a particular relative depth have a nearly constant densimetric Froude number at threshold conditions. Also, the curves start spreading out significantly below a relative depth of about 5, and they tend to come close to each other above this value. The same plot was attempted in Figure 5.9, using the Froude number instead. As can be seen, no useful information can be extracted from this plot. As a reminder, the dimensional analysis in Section 4.1 yielded the densimetric Froude number, not the Froude number as one of the 4 dimensionless terms.

5.2.2 Threshold Conditions without Considering the Bursting Period

In Section 4.2.1, it was suggested that the bursting cycle is the mechanism responsible for the beginning of sediment motion. This led to the expression for the probability of entrainment (Eq. 4.4), in which the average frequency of particle displacement is multiplied by the bursting period. A different approach is to not consider the bursting period. In this approach threshold conditions are reached when f_{avg} is within $\pm 20\%$ of $f_{avg,crit}$ rather than P_E being within $\pm 20\%$ of $P_{E,crit}$.

Figure 5.10 is the modified Shields diagram for the glass ball data using both approaches. One curve is the one already seen in Figure 5.3, where the bursting period is considered. The other one is developed using experiments within $\pm 20\%$ of $f_{avg,crit}$. Of the four experiments used for this curve, two are from the previous set summarized in Tables 5.1-5.3, namely A3 and B3. The other two are additional experiments and are summarized in Tables 5.4a-b and Appendix 1. They are identified as D3T_B and E3T_B. The two curves in Figure 5.10 follow the same general trend. However, the points at $H/D_{50} = 5$ and 6 for the runs that do not consider T_B have a higher dimensionless critical shear stress than their counterparts. For instance, in the $H/D_{50} = 6$ case, the dimensionless critical shear stress is 0.00623 when considering the bursting period and 0.00679 when

not. In the latter case, $f_{\text{avg}}/f_{\text{avg_crit}} = 1.17$ while $P_E/P_{E_{\text{crit}}} = 2.53$. To satisfy the criterion for threshold conditions ($\pm 20\%$ of $f_{\text{avg_crit}}$), the P_E has to be much higher than $P_{E_{\text{crit}}}$. This explains the increase in dimensionless critical shear stress. The critical stresses obtained by the two methods are compared in Table 5.4c.

5.2.3 Threshold Conditions with M1 Water Surface Profiles

In Section 4.4.1, it was emphasized how important it is to maintain uniform flow conditions in order to get reliable results. Any deviation from uniform flow conditions can have significant effects on the dimensionless critical shear stress. This section will present 3 experiments run under M1 profiles. Tables 5.5a and b summarize the general information of these 3 experiments. Table 5.5b shows that these tests are within $\pm 20\%$ of $P_{E_{\text{crit}}}$. Table 5.5c compares the dimensionless critical shear stress of the uniform flow case with the M1 case for teflon, glass, and ceramic particles at $H/D_{50} = 3$. For the teflon and glass ball experiments the dimensionless critical shear stress jumped by 38% and 36%, respectively. The jump for the ceramic balls was less dramatic, at 13%. The main cause of these differences is that velocities in the M1 case tend to be lower and therefore steeper slopes are required for particles to be entrained.

For flows with M2 surface profiles, velocities are higher and therefore milder slopes are required to avoid massive motion. In this case, dimensionless critical shear stresses are significantly lower than their counterparts at uniform flow. No results are available for presentation here because the motion was too massive and within a few minutes, the test section no longer resembled an evenly spread 2% packed bed.

5.2.4 Sensitivity Analysis

Minor changes in the flow conditions or slope can have a significant effect on the number of particles entrained. This type of sensitivity is especially true when particles are fully exposed to the flow, as is the case in the 2% packing condition, and when the angle of repose of the particles is relatively low. This section will focus on the effect of minor slope changes on the probability of particle entrainment. It will also be shown that the probability of particle entrainment can vary from run to run without changing the slope. The discussion will be dominated by examples, which include a few of the 29

experiments from Tables 5.1-5.3 and some preliminary runs from the trial-and-error procedure. No detailed information about the preliminary runs is provided in Appendix 1.

Due to the stochastic nature of turbulent flow, it is impossible to predict the exact number of particles that will be entrained in a particular test. When several identical runs are compared, P_E/P_{Ecrit} ratios can be found to vary. For example, after a few trial-and-error runs, the P_E/P_{Ecrit} ratio for experiment F3 was 1.00, a perfect ratio for the incipient criterion used. However, during one of the preliminary runs using the same slope, relative depth, and all other conditions, the P_E/P_{Ecrit} ratio was 1.41. Similarly, the P_E/P_{Ecrit} ratio for experiment D3 was 0.92 and 1.41 for two identical runs. This type of behavior was consistent for all the experiments.

Some experiments are very sensitive to slight changes in slope. This is especially true at steeper slopes where sediment particles can be highly unstable. The P_E/P_{Ecrit} ratio for experiment F4 was 0.84 when run at a slope of 0.26% but jumped to 1.41 when the slope was slightly increased to 0.27%. Similarly, the P_E/P_{Ecrit} ratio for experiment G2 was 1.14 at a slope of 0.035% and 1.69 at a slope of 0.04%. A more dramatic change occurred with experiment F3. The P_E/P_{Ecrit} ratios of 1.00 and 1.41 mentioned in the previous paragraph occurred when the slope was set at 0.135%. A slight increase to 0.14% caused the P_E/P_{Ecrit} ratio to jump to 2.34.

In a few cases, the opposite effect took place. During a preliminary run of experiment D1, the P_E/P_{Ecrit} ratio was 1.23 at a slope of 0.02% and increased to 1.36 when the slope was dropped to 0.015%. This behavior was not frequent, but can be expected in turbulent flows where the movement of sediment is stochastic.

5.3 Final Remarks

The experiments in this study are highly reliable for the observation of trends like those in Figures 5.1-5.10. The criterion for incipient conditions used is very well defined and strict. However, several factors can create some scatter. For instance, the experiments are observed by eye, making it possible to miss some barely detectable particle displacements. To remedy this situation, each 20-minute test was observed at least twice. The most efficient and accurate method to count particle displacements is by image processing software such as Khoros.

Another factor that can contribute to some scatter in the data is the condition of the bed during the experiments. At threshold conditions, the sediment particles move and the conditions of the bed are not quite the same as when the experiment started. A major effort was made to minimize this, but sometimes it proved impossible to maintain conditions in which each test particle is exactly 6 ball diameters away from the next particle. This was especially difficult for the experiments with a relative depth of 2.

Section 5.2.4 showed that 2 runs with the same relative depth and particle type, but slightly different slopes, can produce a similar probability of entrainment. This stochastic behavior can create scatter in the modified Shields diagram because the dimensionless shear stress is a function of slope.

Finally, some particle displacements can be pseudo-displacements. These pseudo-displacements are motions that are due to the effects of increasing the pump speed. To avoid these, about 5 minutes were allowed to elapse after the final pump speed increase before starting the 15-20 minute test.

The four factors mentioned in this section can create some scatter in the plots. However, this scatter is very minimal and a major effort was made to minimize it. In fact, scatter is present in the traditional Shields diagram as well as in Figure 2.1, which is based on the research of several investigators. Scatter is very common when dealing with experiments at critical conditions and in sediment transport in general. In conclusion, the experiments in this study were very carefully conducted and the data is highly reliable.

Table 5.1 Ranges of values obtained for the different particle types (uniform flow experiments at threshold conditions).

Type of Particle	H/D ₅₀	Slope (%)	Froude Number	Densimetric Froude Number	τ_{cr}^*
Viton (SG = 1.83)	2-6	0.015-0.3	0.38-0.69	0.41-0.76	0.00108- 0.00723
Teflon (SG = 2.11)	2-8	0.035-0.6	0.39-0.80	0.37-0.76	0.00252- 0.0108
Glass (SG = 2.59)	2-12	0.075-0.9	0.36-0.86	0.29-0.68	0.00566- 0.0113
Ceramic (SG = 3.80)	2-10	0.17-1.65	0.57-1.29	0.34-0.77	0.00607- 0.0118

Table 5.2 Summary of experiments (uniform flow at threshold conditions).

H / D ₅₀	SG of Ball	Slope (%)	Depth Averaged Velocity (m/s)	Froude Number	Densimetric Froude Number	τ_{cr}^*
2	1.83	0.3	0.27	0.69	0.76	0.00723
2	2.11	0.6	0.32	0.80	0.76	0.0108
2	2.59	0.9	0.34	0.86	0.68	0.0113
2	3.80	1.65	0.51	1.29	0.77	0.0118
3	1.83	0.15	0.27	0.55	0.60	0.00542
3	2.11	0.29	0.32	0.67	0.63	0.00784
3	2.59	0.44	0.37	0.77	0.61	0.0083
3	3.80	0.97	0.53	1.09	0.65	0.0104
4	1.83	0.06	0.27	0.49	0.53	0.00289
4	2.11	0.1	0.30	0.54	0.51	0.0036
4	2.59	0.28	0.35	0.62	0.49	0.00704
4	3.80	0.62	0.50	0.89	0.53	0.00886
5	1.83	0.025	0.27	0.43	0.47	0.00151
5	2.11	0.08	0.31	0.50	0.47	0.0036
5	2.59	0.21	0.35	0.56	0.44	0.0066
5	3.80	0.43	0.50	0.80	0.48	0.00768
6	1.83	0.015	0.26	0.38	0.41	0.00108
6	2.11	0.06	0.31	0.45	0.43	0.00324
6	2.59	0.165	0.34	0.50	0.40	0.00623
6	3.80	0.32	0.51	0.74	0.44	0.00686
7	2.11	0.045	0.31	0.41	0.39	0.00284
7	2.59	0.135	0.35	0.47	0.38	0.00594
7	3.80	0.26	0.52	0.70	0.42	0.0065
8	2.11	0.035	0.31	0.39	0.37	0.00252
8	2.59	0.115	0.36	0.46	0.36	0.00579
8	3.80	0.22	0.50	0.64	0.38	0.00629
10	2.59	0.09	0.36	0.41	0.33	0.00566
10	3.80	0.17	0.50	0.57	0.34	0.00607
12	2.59	0.075	0.35	0.36	0.29	0.00566

Table 5.3 Summary of parameters related to the criterion for threshold conditions (uniform flow experiments).

H / D ₅₀	SG of Ball	# Balls Moving (20 min)	f_{avg} (1 / s)	f_{avg}/f_{avg_crit}	T _B (s)	P _E	P _E /P _{Ecrit}
2	1.83	21	2.89E-4	1.00	0.35	1.01E-4	1.00
2	2.11	19	2.67E-4	0.92	0.30	8.12E-5	0.80
2	2.59	22	2.96E-4	1.02	0.28	8.39E-5	0.83
2	3.80	20*	4.05E-4	1.40	0.19	7.62E-5	0.75
3	1.83	13	1.91E-4	0.66	0.54	1.03E-4	1.02
3	2.11	17	2.14E-4	0.74	0.45	9.52E-5	0.94
3	2.59	23	2.87E-4	0.99	0.39	1.11E-4	1.09
3	3.80	26	3.59E-4	1.24	0.27	9.74E-5	0.96
4	1.83	11	1.46E-4	0.51	0.71	1.03E-4	1.01
4	2.11	12	1.54E-4	0.53	0.64	9.78E-5	0.96
4	2.59	15	1.92E-4	0.66	0.55	1.06E-4	1.05
4	3.80	19	2.59E-4	0.90	0.38	9.95E-5	0.98
5	1.83	9	1.12E-4	0.39	0.90	1.00E-4	0.99
5	2.11	10	1.29E-4	0.45	0.77	9.90E-5	0.98
5	2.59	11	1.36E-4	0.47	0.69	9.34E-5	0.92
5	3.80	15	2.04E-4	0.71	0.48	9.75E-5	0.96
6	1.83	6	7.67E-5	0.27	1.12	8.60E-5	0.85
6	2.11	9	1.14E-4	0.39	0.94	1.07E-4	1.05
6	2.59	8	1.06E-4	0.37	0.84	8.93E-5	0.88
6	3.80	15	1.96E-4	0.68	0.57	1.11E-4	1.09
7	2.11	8	1.04E-4	0.36	1.10	1.15E-4	1.13
7	2.59	8	1.06E-4	0.37	0.96	1.01E-4	1.00
7	3.80	10	1.30E-4	0.45	0.65	8.48E-5	0.84
8	2.11	7	9.37E-5	0.32	1.24	1.16E-4	1.14
8	2.59	9	1.09E-4	0.38	1.06	1.15E-4	1.14
8	3.80	10	1.37E-4	0.47	0.76	1.04E-4	1.03
10	2.59	7	8.58E-5	0.30	1.32	1.14E-4	1.12
10	3.80	8	1.03E-4	0.36	0.95	9.87E-5	0.97
12	2.59	6	6.85E-5	0.24	1.64	1.13E-4	1.11

* Based on a 15 minute experiment

Table 5.4a Summary of experiments (uniform flow at threshold conditions without considering the bursting period).

H / D ₅₀	SG of Ball	Slope (%)	Depth Averaged Velocity (m/s)	Froude Number	Densimetric Froude Number	τ_{cr}^*
5	2.59	0.235	0.38	0.60	0.47	0.00739
6	2.59	0.18	0.38	0.55	0.44	0.00679

Table 5.4b Summary of parameters related to the criterion for threshold conditions (uniform flow experiments without considering the bursting period).

H / D ₅₀	SG of Ball	# Balls Moving (20 min)	f_{avg} (1 / s)	f_{avg}/f_{avg_crit}	T _B (s)	P _E	P _E /P _{Ecrit}
5	2.59	21	2.70E-4	0.93	0.64	1.73E-4	1.71
6	2.59	29	3.39E-4	1.17	0.76	2.57E-4	2.53

Table 5.4c Comparison of the dimensionless critical shear stress for experiments that consider the bursting period vs. those that do not.

H / D ₅₀	SG of Ball	τ_{cr}^* (Considering T _B)	τ_{cr}^* (w/o Considering T _B)	% Increase in τ_{cr}^*
5	2.59	0.00660	0.00739	12
6	2.59	0.00623	0.00679	9

Table 5.5a Summary of experiments (M1 water surface profile at threshold conditions).

H / D ₅₀	SG of Ball	Slope (%)	Depth Averaged Velocity (m/s)	Froude Number	Densimetric Froude Number	τ_{cr}^*
3	2.11	0.4	0.31	0.64	0.60	0.0108
3	2.59	0.6	0.36	0.75	0.59	0.0113
3	3.80	1.1	0.49	1.02	0.61	0.0118

Table 5.5b Summary of parameters related to the criterion for threshold conditions (experiments with M1 profile).

H / D ₅₀	SG of Ball	# Balls Moving (20 min)	f_{avg} (1 / s)	f_{avg}/f_{avg_crit}	T _B (s)	P _E	P _E /P _{Ecrit}
3	2.11	16	2.31E-4	0.80	0.47	1.08E-4	1.06
3	2.59	21	2.60E-4	0.90	0.40	1.03E-4	1.02
3	3.80	25	2.92E-4	1.01	0.29	8.52E-5	0.84

Table 5.5c Comparison of dimensionless critical shear stress for experiments with uniform flow vs. experiments with M1 profile.

H / D ₅₀	SG of Ball	τ_{cr}^* (Uniform Flow)	τ_{cr}^* (M1 Curve)	% Increase in τ_{cr}^*
3	2.11	0.00784	0.0108	38
3	2.59	0.0083	0.0113	36
3	3.80	0.0104	0.0118	13

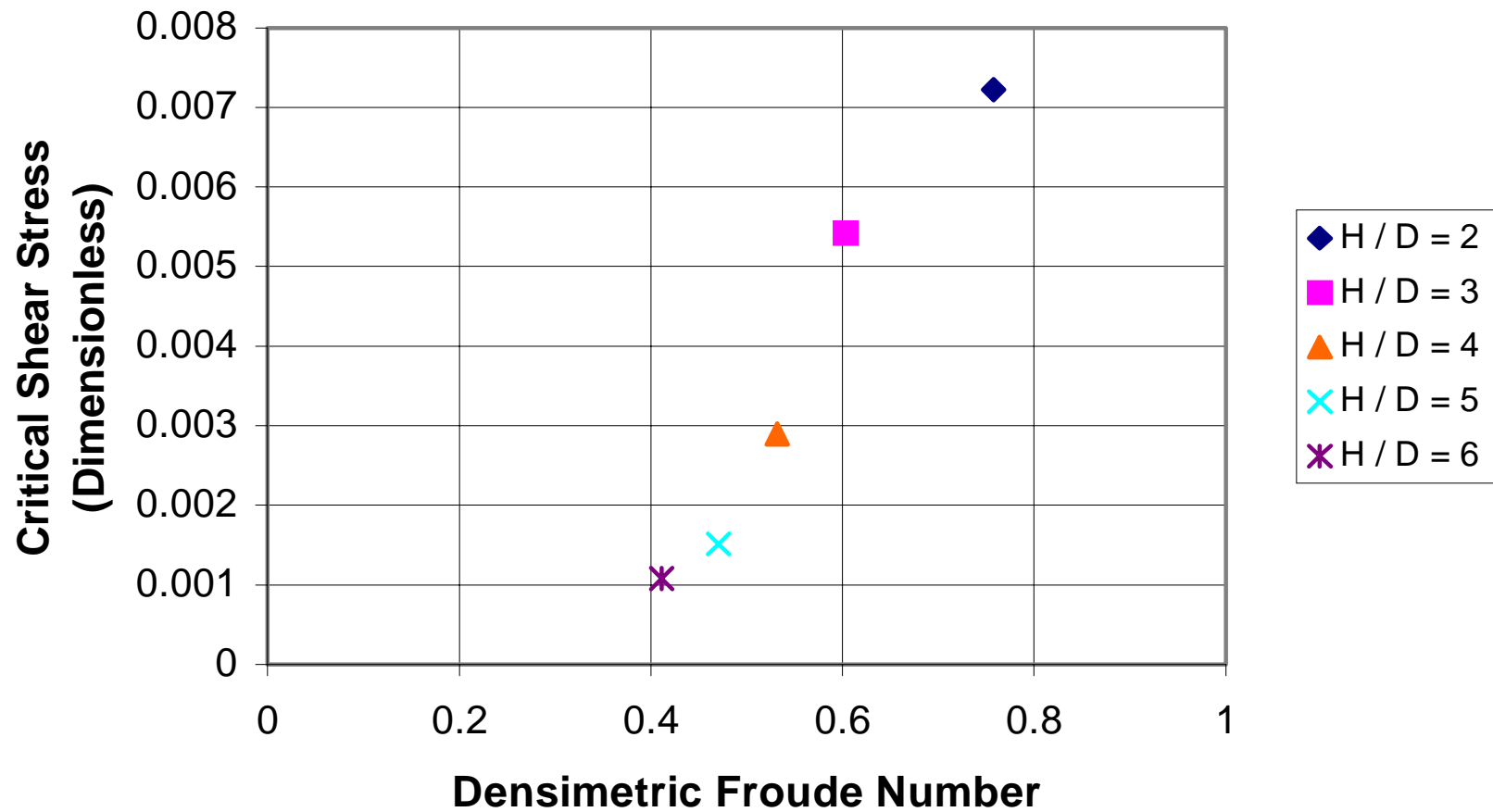


Figure 5.1 Plot of the dimensionless critical shear stress vs. densimetric Froude number and relative depth (modified Shields diagram) for the viton ball data.

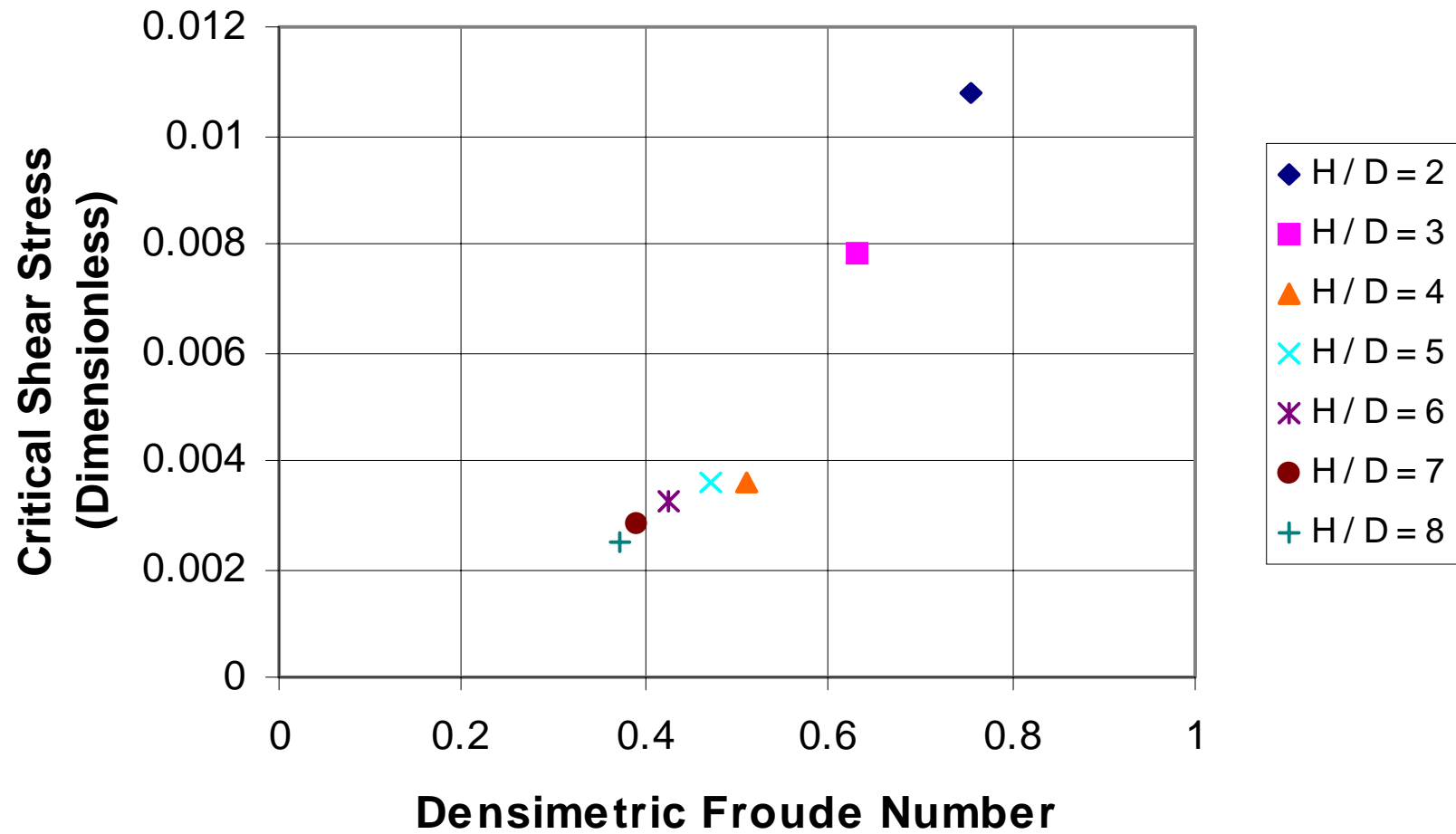


Figure 5.2 Plot of the dimensionless critical shear stress vs. densimetric Froude number and relative depth (modified Shields diagram) for the teflon ball data.

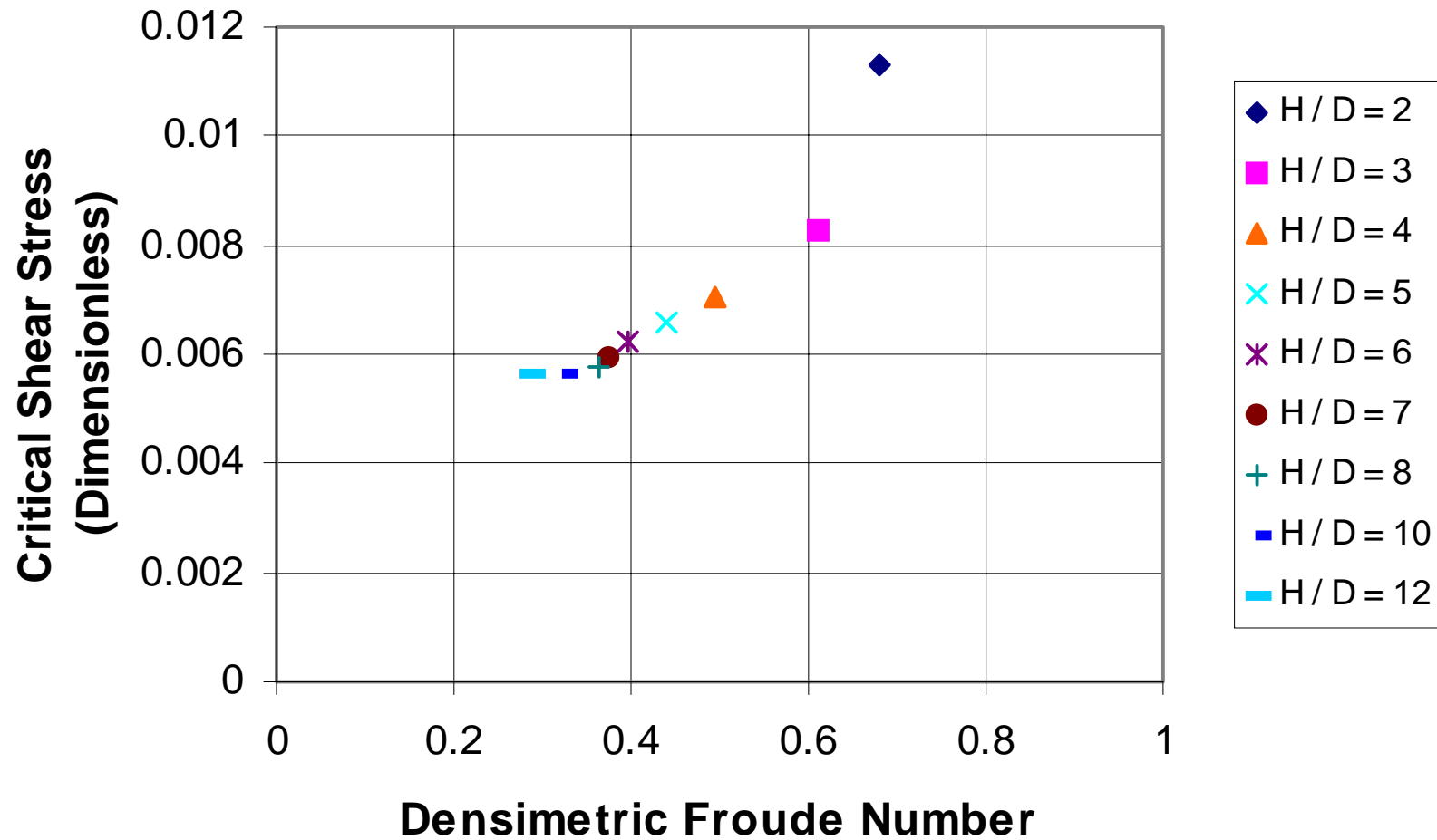


Figure 5.3 Plot of the dimensionless critical shear stress vs. densimetric Froude number and relative depth (modified Shields diagram) for the glass ball data.

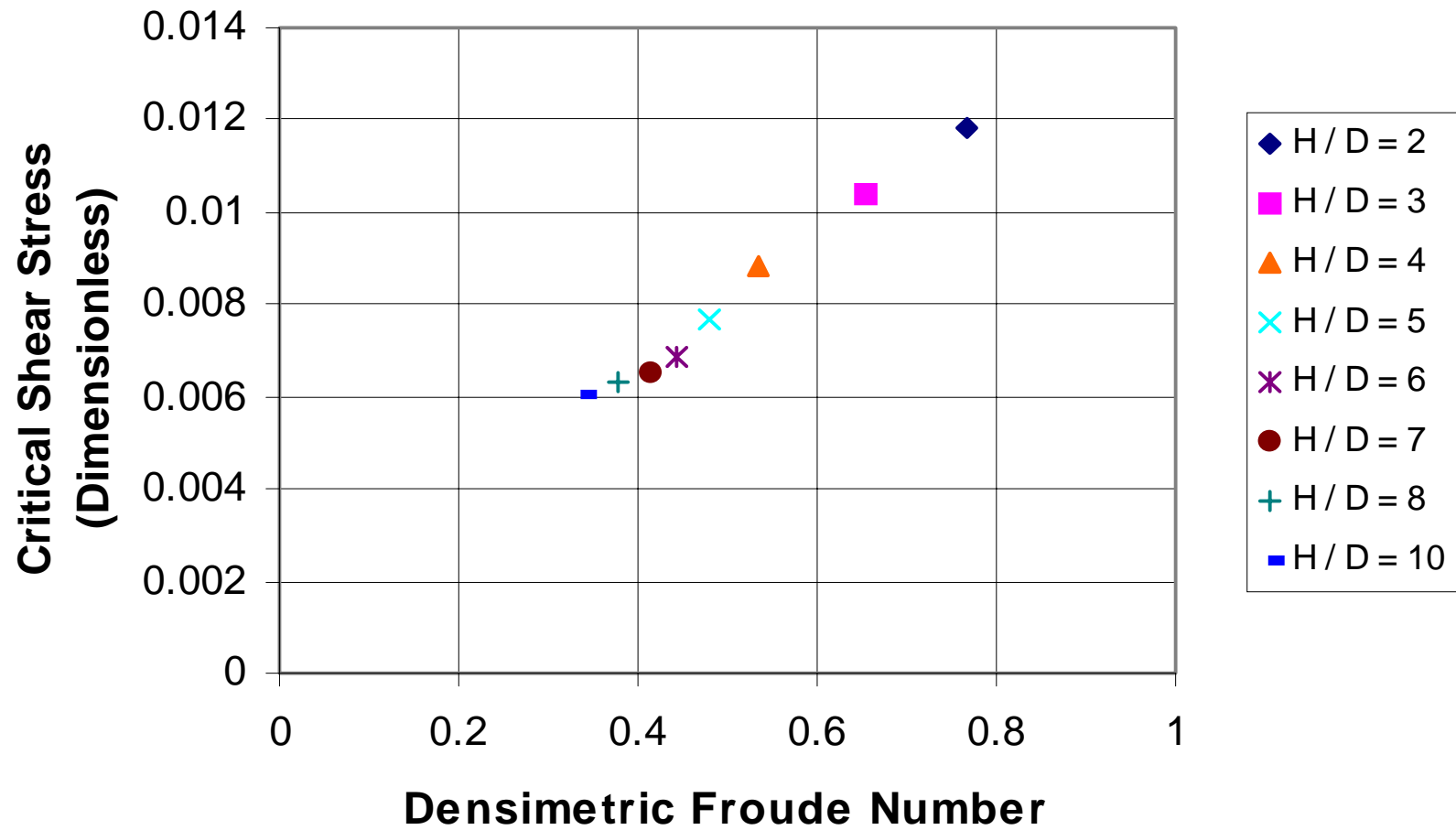


Figure 5.4 Plot of the dimensionless critical shear stress vs. densimetric Froude number and relative depth (modified Shields diagram) for the ceramic ball data.

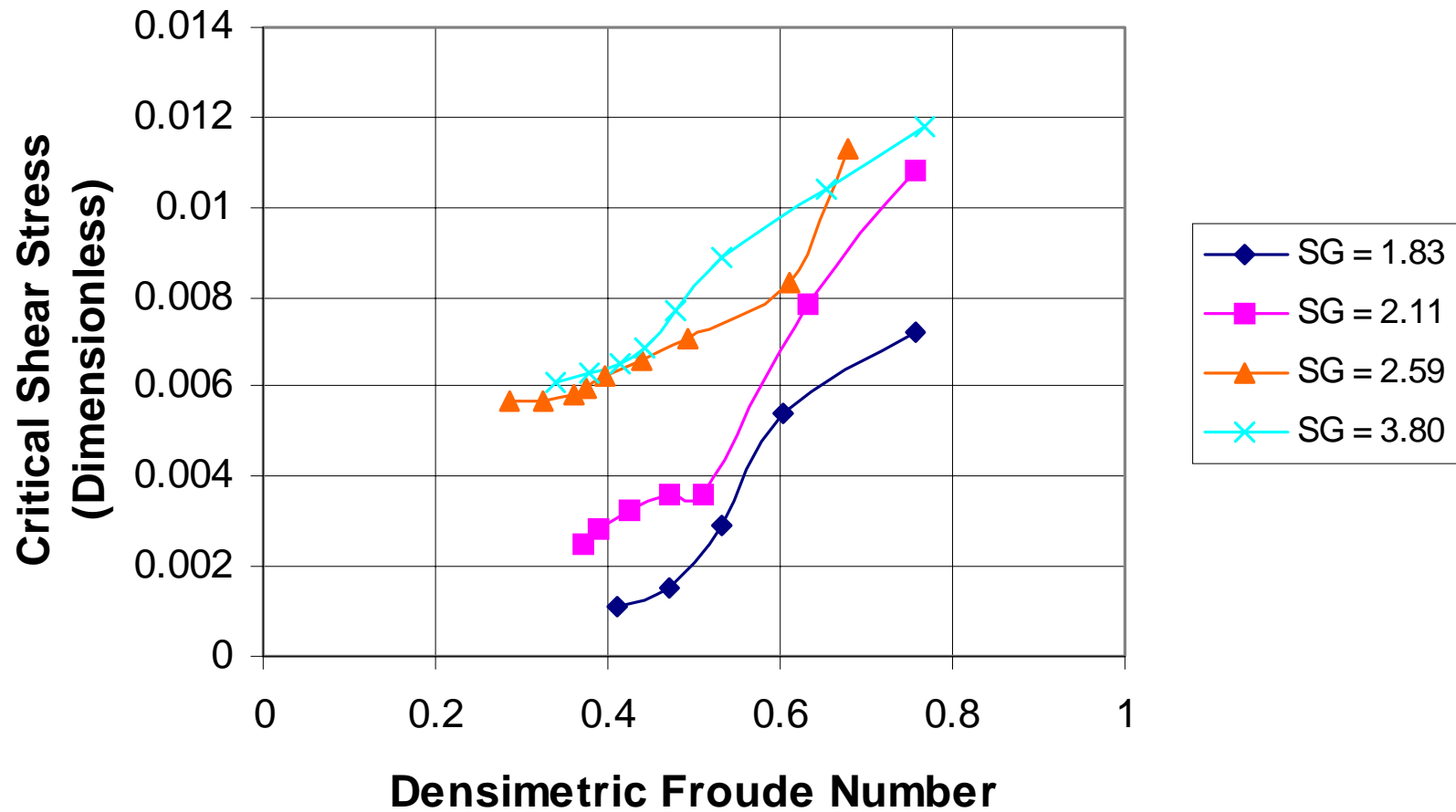


Figure 5.5 Plot of the dimensionless critical shear stress vs. densimetric Froude number for the 4 particle densities.

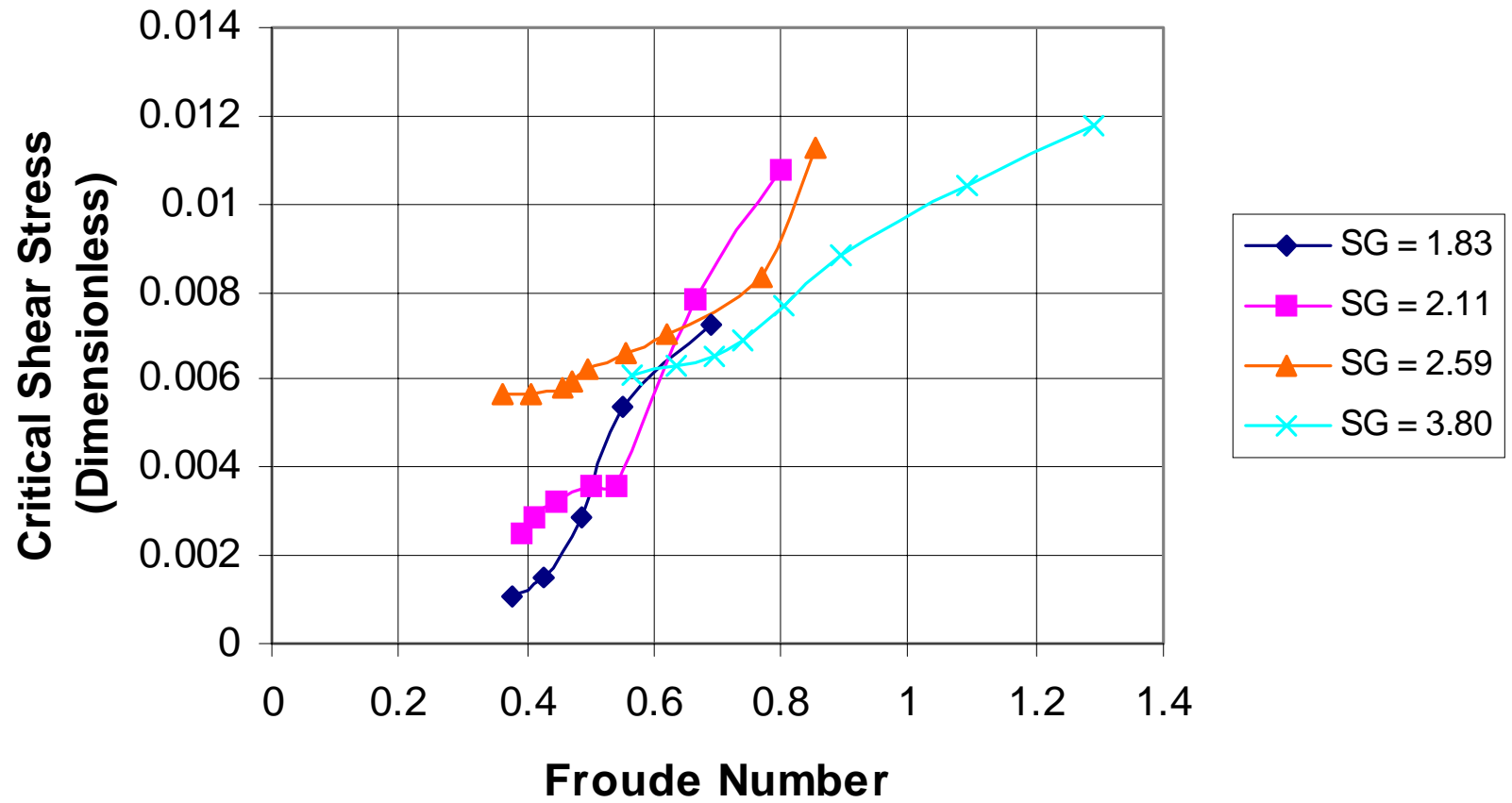


Figure 5.6 Plot of the dimensionless critical shear stress vs. Froude number for the 4 particle densities.

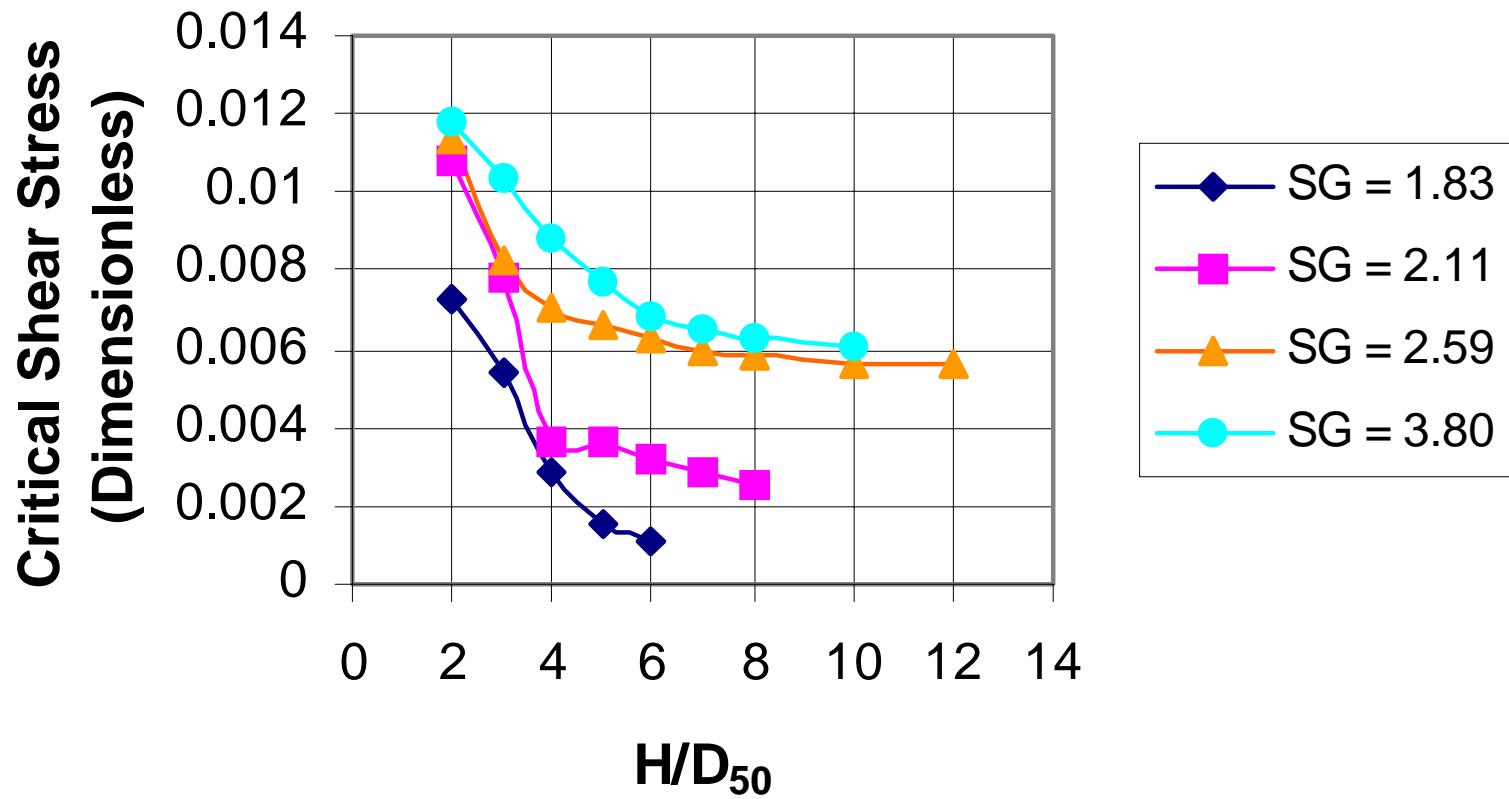


Figure 5.7 Plot of the dimensionless critical shear stress vs. relative depth for the 4 particle densities.

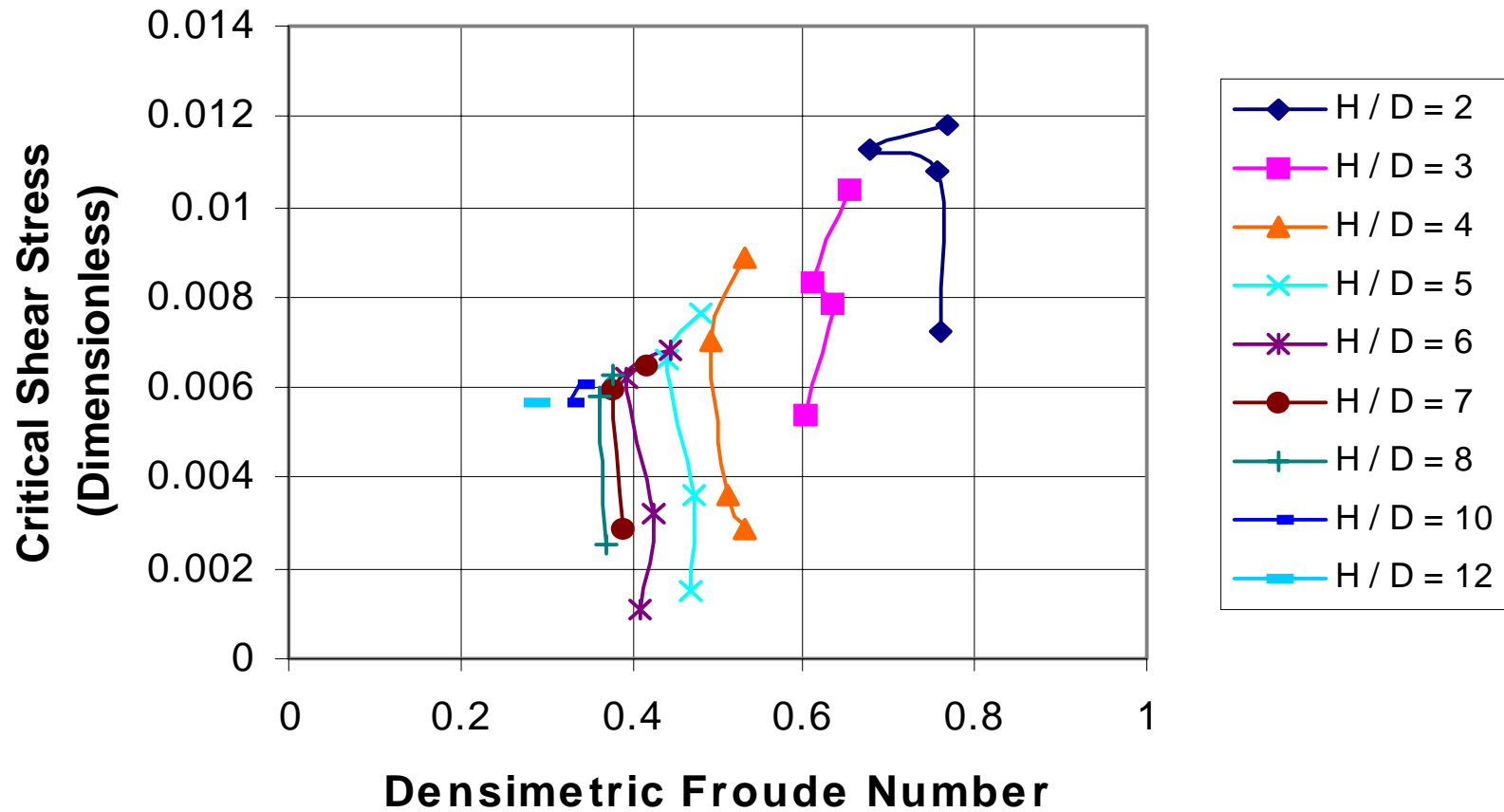


Figure 5.8 Plot of the dimensionless critical shear stress vs. densimetric Froude number for the whole range of relative depths ($H/D_{50} = 2-12$).

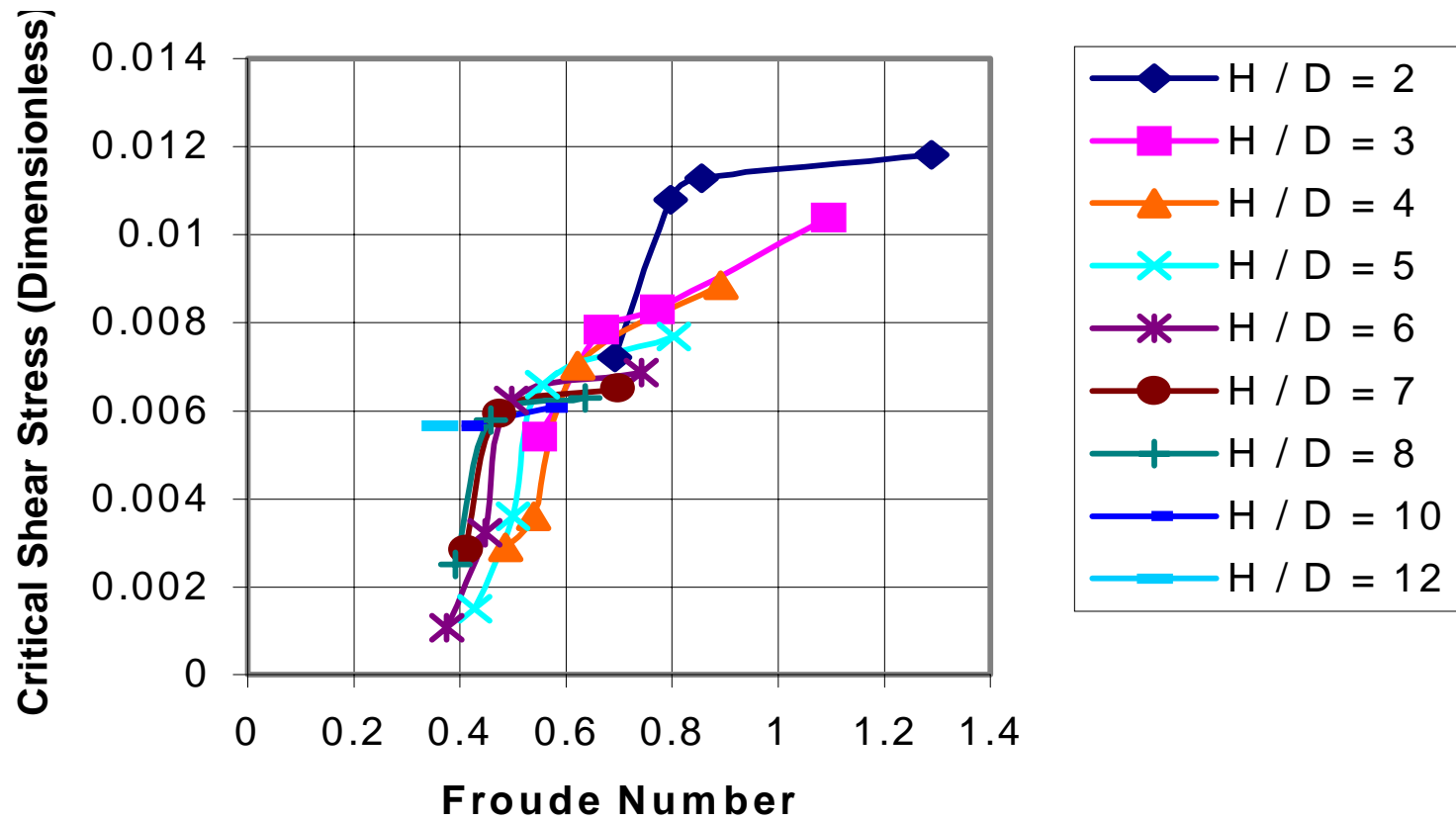


Figure 5.9 Plot of the dimensionless critical shear stress vs. Froude number for the whole range of relative depths ($H/D_{50} = 2-12$).

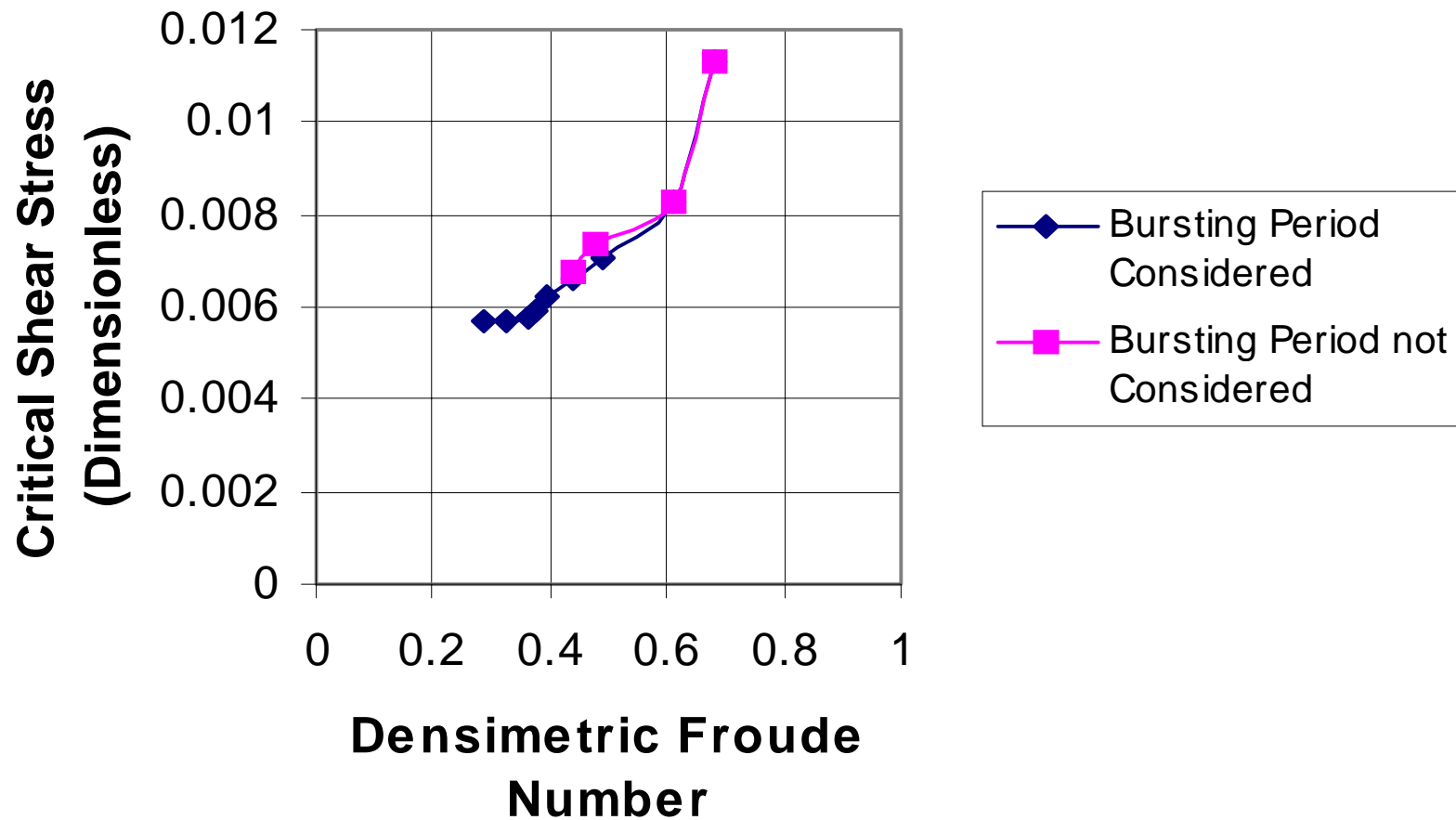


Figure 5.10 The modified Shields diagram for the glass ball experiments when considering the bursting period vs. not considering the bursting period in the criterion for incipient conditions.

Chapter 6. Velocity Profiles

6.1 Introduction

Velocity profiles were taken for 14 different cases, namely experiments C-I3 (glass balls, $H/D_{50} = 4-12$), 2 supercritical flows, and 5 pressurized flows. As indicated in Table 6.1, these experiments have k_s^+ values above 70. Therefore, the bed is fully rough and equation 2.15 is used as the basis for the velocity distribution analysis. The representative length of the roughness elements, k_s , is set equal to the median particle diameter, D_{50} . This is an appropriate selection for the type of bed used in the present study, because the test particles are contributing to most of the form drag. Einstein and Barbarossa (1953) used a similar value, $k_s = D_{65}$. The datum is set at the top of the balls in the well-packed bed. The traditional approach of setting the datum beneath the top of the balls is not followed for reasons that will be mentioned in Section 6.2. The friction velocity is computed as

$$u^* = \sqrt{\frac{\tau_w}{\rho_f}} \quad (6.1)$$

where τ_w = shear stress at the wall. In open channels, the friction velocity can be approximated as

$$u^* = \sqrt{gHS} \quad (6.2).$$

Since the flow is fully rough, the Reynolds stress measured by the LDV is used as τ_w . Therefore,

$$\tau_w = -\rho_f \overline{u'v'} \quad (6.3)$$

where u' and v' are the fluctuating components of the velocity in the x and z directions, respectively, and the bar over these terms denotes their product averaged over a period of time. Measurements were taken by the LDV at several points very close to the bed. The friction velocity is computed using equations 6.1 and 6.3 for the 2 or 3 points closest to the bed, which are between 1-3 mm away from it. The u^* value that most closely matches the approximate value (eq. 6.2) is selected for use in the log-law. Table 6.1 shows how the friction velocity computed from the Reynolds stress compares to the approximation. In addition, it shows how the Reynolds stress compares to the bed shear stress

approximation of $\tau_w = \gamma_f HS$ applicable in open channels. The approximations agree very well with the values measured by the LDV. The approximate values of the bed shear stress agree within $\pm 6\%$ of the LDV values in seven out of the nine free surface experiments. Considering the fact that the measurement of slope and depth are subject to visual error, this is a very close approximation. Therefore, the use of equation 4.7 for the calculation of dimensionless critical shear stress is justified. Table 6.1 also shows that the shear velocity computed by equation 6.2 agrees within $\pm 3\%$ of the LDV value for seven out of the nine free surface experiments. These strong agreements provide confidence that the LDV measurements are accurate.

6.2 Velocity Profile Plotting Procedure

Several methods of plotting the velocity profiles are presented here. Figure 6.1a shows a typical profile plotted in arithmetic coordinates. Due to the 4.8° tilt of the laser's traverse table, measurements could not be taken higher than about 5mm below the free surface. Figure 6.1b shows the same profile in semi-log paper. It can be seen that there is no deviation from the log-law, so no wake-strength coefficient is necessary. This is true for all velocity profiles in this study. Therefore, the rough wall log-law (equation 2.15) is used for the entire flow depth. Cardoso et al. (1989) also used the law of the wall to fit the data along the entire flow depth. An interesting feature of the profile in Figure 6.1b is that the points near the bed ($z/k_s < 0.8$) follow a different slope than the rest of the points. This occurs when the datum is set at the top of the balls in the channel bed. As the datum is lowered, the slope of the points at $z/k_s < 0.8$ starts approaching the slope of the rest of the points. Figure 6.1c shows that when the datum is lowered to $0.4375k$ below the top of the balls in this particular case, the slope in the region very near the wall is equal to the slope that represents the rest of the depth. This behavior was also noticed by Mansour-Tehrani (1992). In that case, the points follow a straight line in semi-log paper along the entire flow depth when the datum is $0.5k$ below the top of the spheres in the bed. When the datum is at the top of the balls, the velocity profile splits into 2 separate regions as seen in Figure 6.1b. This is also apparent in Kirkgoz's (1989) rough wall data. This type of behavior has not been documented often, but is apparent in works conducted with an LDV, which allows for measurements very close to the bed. The problem with Figure

6.1b is that the von Karman constant does not match the universally known value of 0.40. Figure 6.1b shows that for the region of $z/k_s > 0.8$, $\kappa = 0.336$. However, a much closer value to the von Karman constant is obtained when a single straight line is run through the entire flow depth. Figure 6.1d shows a plot of the same velocity profile with a single line (equation) representing all the points. The datum is at the top of the balls in the bed. As seen, $\kappa = 0.382$, which is closer to 0.4 than the κ obtained in Figure 6.1b. Figure 6.1d also shows that the correlation coefficient, R^2 , is high ($R^2 = 0.9836$) when fitting a single line to the entire depth, although not as high as when splitting the depth into two regions. Figure 6.1e shows a plot very similar to the one in Figure 6.1d. The difference is that the datum is lowered to 1mm (0.125k) below the top of the balls in the bed. The correlation coefficient improves to 0.9947, but the von Karman constant drops to 0.34. The integral constant, B, drops from 9.97 to 9.44. These constants are further affected as the datum is lowered more. Raising the representative length of the roughness elements will increase the integral constant. For example, if a value of $k_s = 2D_{50}$ is used in the profile in Figure 6.1d, B jumps to 11.78, which is considerably higher than the typical value of 8.5 (Nikuradse 1933, Monin and Yaglom 1975). Therefore, it is desirable to keep $k_s = D_{50}$.

The preferred plotting procedure for the analysis of the velocity profiles is the one shown in Figure 6.1d, where the datum is at the top of the balls in the bed and the entire data is represented by a single straight line. This method is preferred because the values of κ obtained are very close to the universally known value. The procedure is also justified by the high R^2 values. Sections 6.3 and 6.4 will discuss the results for the free surface and pressurized flows, respectively, using this procedure. However, Appendix 2 contains tables that summarize the results for all 14 cases when using the methods depicted by Figure 6.2b (velocity profile split into 2 regions) and Figure 6.2e (single region, datum is 1mm below top of the ball). Appendix 2 also includes plots similar to Figures 6.1a,b,d, and e for all 14 cases.

6.3 Results (Velocity Profiles for Free Surface Flows)

Table 6.2 summarizes the von Karman constant, integral constant, and correlation coefficient obtained from the logarithmic velocity profiles in the free surface flows. For all nine cases the correlation coefficient is high, meaning that a single equation fits the

data for the entire flow depth well. The average κ is 0.395 with a standard deviation, σ , of 0.0188. This shows that κ remains constant, regardless of Froude number and relative depth. The integral constant averages 9.64 with a narrow standard deviation of 0.604. In general, some scatter is always present when looking at κ and B values of different experiments. No trend is seen with the Froude number or relative depth. However, the range of Froude numbers here (0.36-1.17) is very narrow compared to the range tested by Tominaga and Nezu (1992) and Prinos and Zeris (1995). Using the average constants from Table 6.2, the logarithmic velocity equation representing the free surface experiments in this study is

$$\frac{V}{u^*} = 2.54 \ln \frac{z}{k_s} + 9.64 \quad (6.4)$$

which is similar to that obtained by Nikuradse (1933) in rough pipes.

From the information in Table 6.2 it can be concluded that although the dimensionless critical shear stress changes with decreasing relative depth and increasing Froude number the velocity distribution does not. As mentioned in Section 2.1.1, Ashida and Bayazit (1973) found that the non-dimensional velocity, V/u^* , at a certain distance from the bed decreases as the depth of flow diminishes. They mentioned that this could be a partial explanation to why critical shear stress increases when relative depth decreases. A drop of V/u^* was not seen in the present study, possibly ruling out that this phenomenon can be explained by changes in the structure of the velocity profile. Ashida and Bayazit had a range of Froude numbers comparable to those obtained by Tominaga and Nezu and Prinos and Zeris. This might explain the drop in V/u^* in their experiments.

6.4 Results (Velocity Profiles for Pressurized Flows)

Table 6.3 summarizes the constants of the logarithmic equation for the 5 pressurized flows. The purpose of running tests under pressurized flow in this study is to make comparisons with the free surface flows. The H/D_{50} range for the 5 experiments is 3-8.5 and all five experiments were run at a slope of 0.21%. This is part of a trial-and-error procedure with the intention of reproducing the velocity profile obtained in the $H/D_{50} = 5$ free surface case. As seen in Figure 6.2 the effort was not very successful. All the velocities in the pressurized flow, including the one for the $H/D_{50} = 3$ case, are

considerably higher than the velocity corresponding to the free surface case. The head upstream of the lid structure is probably not responsible because it was only 1.35 cm. In any case, Table 6.3 shows that the average von Karman constant is 0.4. The R^2 values are high, but not as high as the ones in Table 6.2. The integral constant is 10.36 with a small standard deviation of 0.21. The value of B is higher for the pressurized flow than it is for the free surface flow, but not considerably. The following logarithmic equation represents the pressurized experiments in this study:

$$\frac{V}{u^*} = 2.51 \ln \frac{z}{k_s} + 10.36 \quad (6.5).$$

The lid was not roughened and the values in Table 6.3 represent the bottom portion of the velocity profile. The maximum velocity typically occurred at 0.70-0.75H.

Incipient motion under pressurized flow was not attempted in this study. If incipient motion was studied for 2 shallow flow experiments with identical slopes and velocity profiles, where one is pressurized and the other is not, it is likely that less motion would occur under the pressurized flow due to the elimination of surface waves, and hence the wave drag component. Sediment transport under a lid structure is analogous to sediment transport under ice.

Table 6.1 Summary of k_s^+ and comparison of the τ_w and u^* values obtained by the LDV vs. the approximations.

H/D ₅₀	τ_w (N/m ²) (LDV)	τ_w (N/m ²) (Approx.)	% Error	u^* (m/s) (LDV)	u^* (m/s) (Approx.)	% Error	k_s^+ **
4	0.838	0.879	4.89	0.0289	0.0296	2.42	259
4 (Fr > 1)	3.29	3.14	-4.56	0.0573	0.0560	-2.27	513
5	0.643	0.824	28.1	0.0254	0.0287	13.0	227
6	0.763	0.777	1.83	0.0276	0.0279	1.09	247
6 (Fr > 1)	4.04	4.00	-0.99	0.0635	0.0633	-0.31	568
7	0.700	0.742	6.00	0.0265	0.0272	2.64	237
8	0.809	0.722	-10.8	0.0284	0.0269	-5.28	254
10	0.718	0.706	-1.67	0.0268	0.0266	-0.75	240
12	0.670	0.706	5.37	0.0259	0.0266	2.70	232

** At 25°C

Table 6.2 Summary of logarithmic velocity profiles for free surface flow: Single region (The datum is at the top of the balls in the channel bed).

H/D ₅₀	Date of Experiment	Slope (%)	Froude Number	A	von Karman κ	B	R ²
4	9/20/98	0.28	0.62	2.58	0.388	10.37	0.9745
4 (Fr>1)	7/14/98	1	1.17	2.32	0.431	8.92	0.9727
5	9/19/98	0.21	0.56	2.46	0.407	10.64	0.971
6	7/17/98	0.165	0.50	2.63	0.380	9.25	0.9896
6 (Fr>1)	7/14/98	0.85	1.11	2.42	0.413	8.95	0.9804
7	7/15/98	0.135	0.47	2.62	0.382	9.97	0.9836
8	8/10/98	0.115	0.46	2.61	0.383	9.82	0.9811
10	6/23/98	0.09	0.41	2.68	0.373	9.40	0.976
12	6/22/98	0.075	0.36	2.51	0.398	9.45	0.9823
Average:	-	-	-	2.54	0.395	9.64	-
Std.Dev:	-	-	-	0.118	0.0188	0.604	-

Table 6.3 Summary of logarithmic velocity profiles for pressurized flow: Single region (The datum is at the top of the balls in the channel bed).

H/D ₅₀	Date of Experiment	Slope (%)	A	von Karman κ	B	R ²
3	9/19/98	0.21	2.48	0.403	10.66	0.97
4.5	9/14/98	0.21	2.79	0.358	10.43	0.9571
5.5	9/13/98	0.21	2.41	0.415	10.14	0.9433
6.5	9/9/98	0.21	2.35	0.426	10.18	0.9496
8.5	9/8/98	0.21	2.52	0.397	10.39	0.9545
Average:	-	-	2.51	0.400	10.36	-
Std.Dev:	-	-	0.170	0.0259	0.210	-

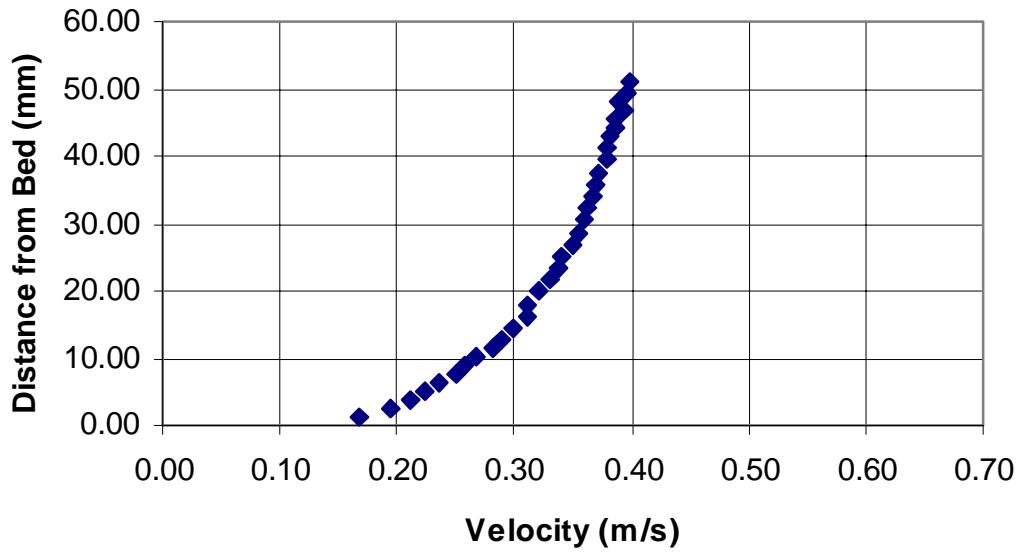


Figure 6.1a Velocity profile for experiment F3 ($H/D_{50} = 7$ and $S = 0.135\%$). The datum is at the top of the balls in the channel bed.

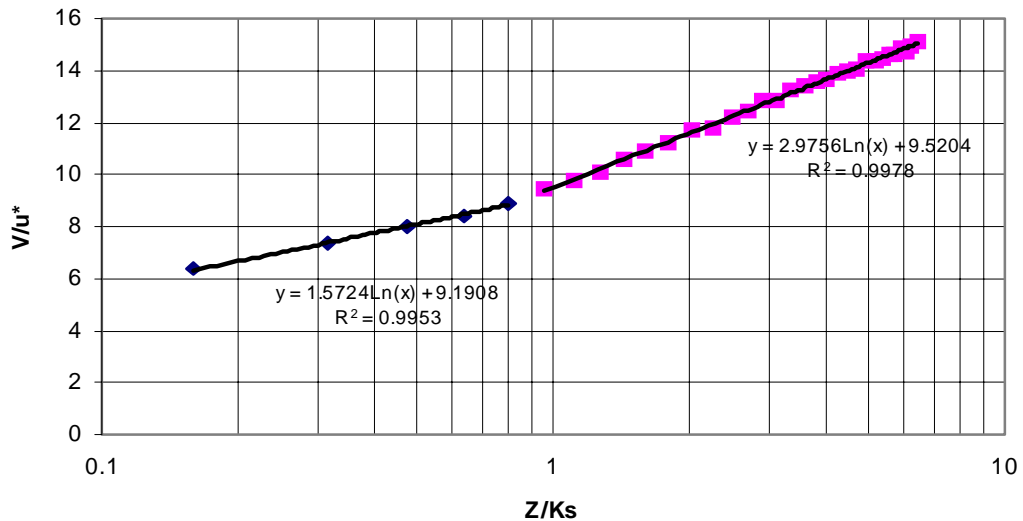


Figure 6.1b Logarithmic velocity profile for experiment F3 ($H/D_{50} = 7$ and $S = 0.135\%$) split into two regions. The datum is at the top of the balls in the channel bed.

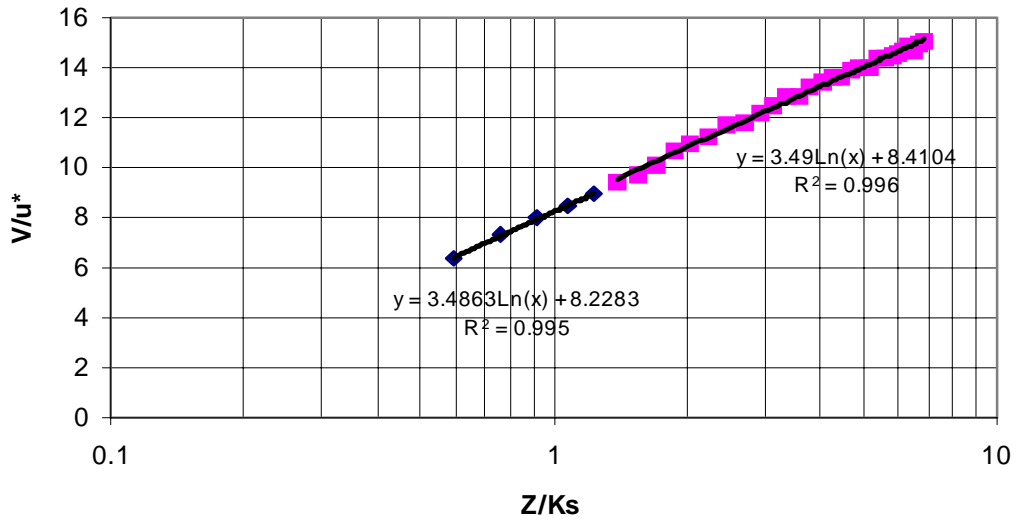


Figure 6.1c Logarithmic velocity profile for experiment F3 ($H/D_{50} = 7$ and $S = 0.135\%$) split into two regions. The datum is 3.5 mm (0.4375k) below the top of the balls in the channel bed.

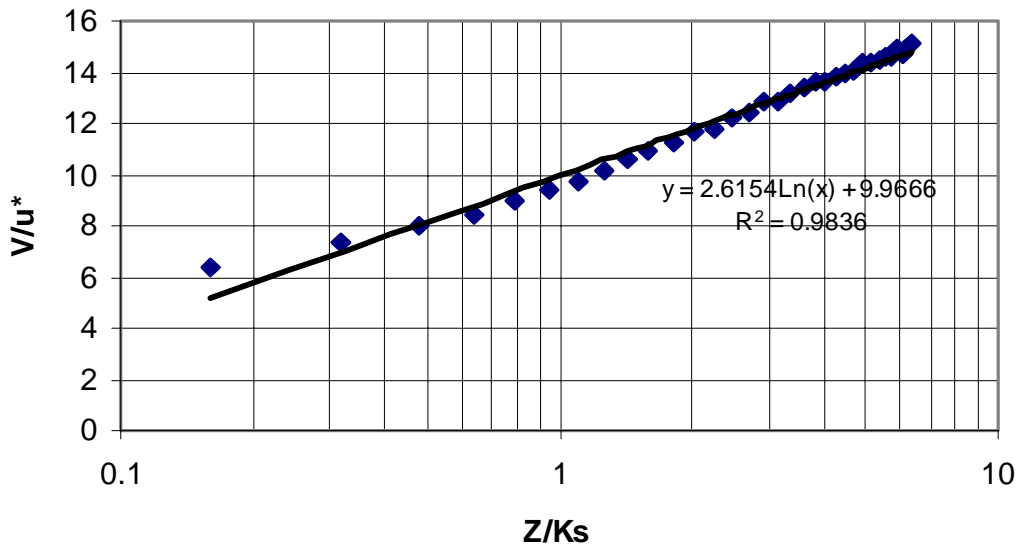


Figure 6.1d Logarithmic velocity profile for experiment F3 ($H/D_{50} = 7$ and $S = 0.135\%$): single region. The datum is at the top of the balls in the channel bed.

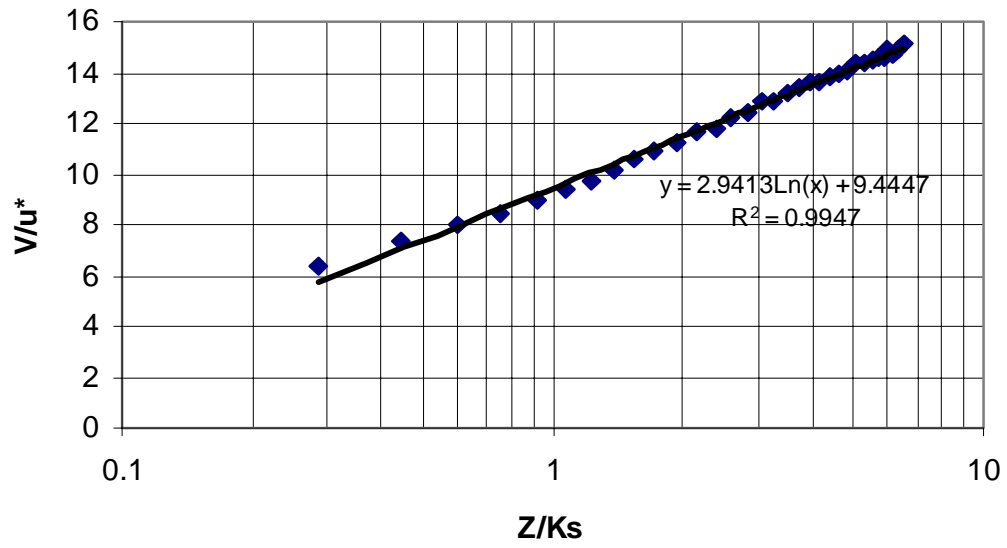


Figure 6.1e Logarithmic velocity profile for experiment F3 ($H/D_{50} = 7$ and $S = 0.135\%$): single region. The datum is 1 mm below the top of the balls in the bed.

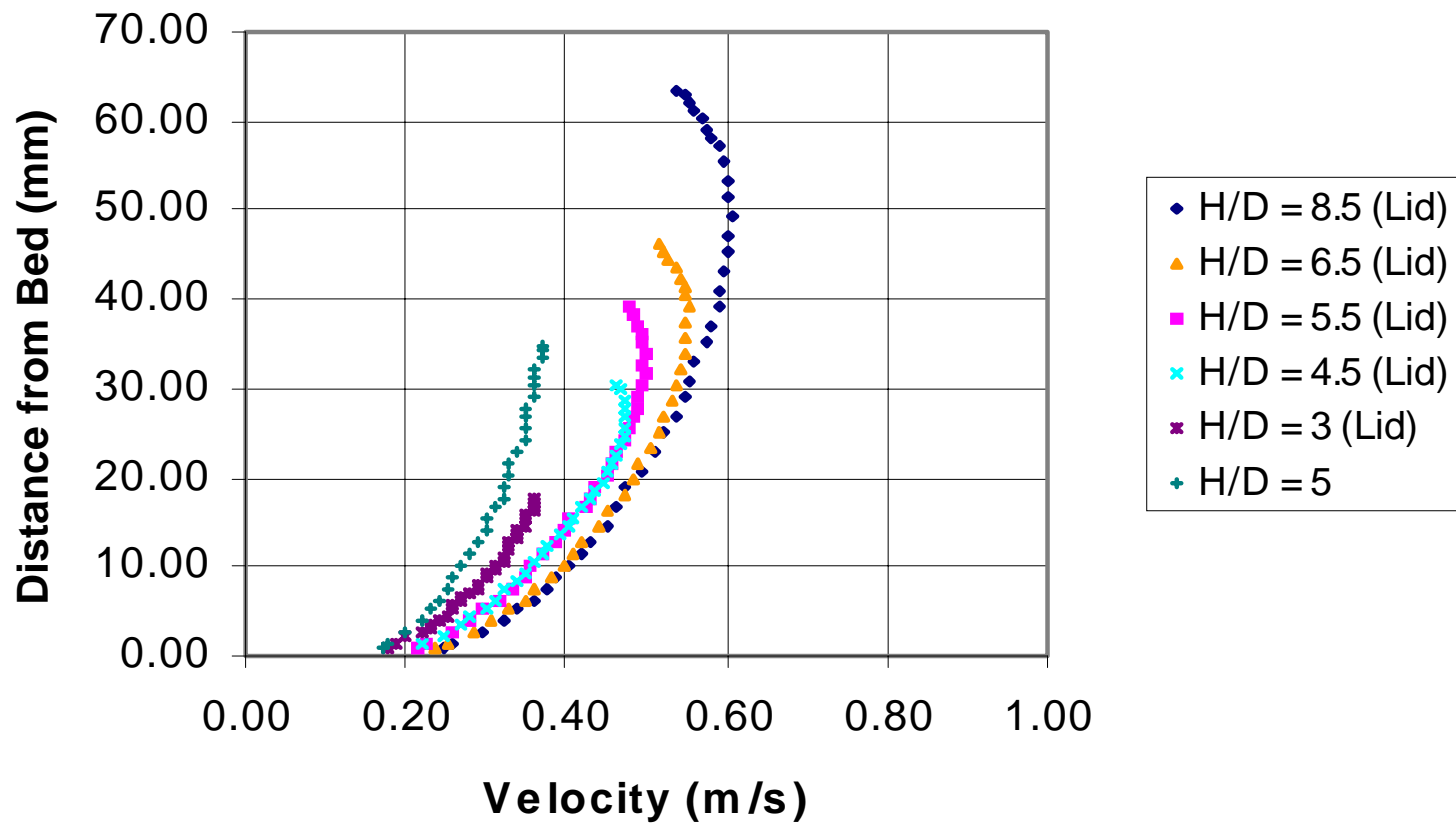


Figure 6.2 Velocity profile comparison of $H/D_{50} = 5$ (free surface) vs. 5 pressurized flows with a relative depth range of 3-8.5.

Chapter 7. Conclusion

The results obtained from this experimental study show that the traditional Shields diagram is not valid in flows with low relative depths and high Froude numbers. For all four particles tested, the dimensionless critical shear stress slowly increases as the relative depth decreases from 10 to approximately 4. As the relative depth drops below 4, the increase in τ_{cr}^* is dramatic. The glass ball data reveal that the τ_{cr}^* value corresponding to the $H/D_{50} = 2$ case is two times higher than the value corresponding to the high relative depths ($H/D_{50} > 10$). Thus, if the traditional Shields diagram is used to design riprap for very shallow flows, the stones may be two times larger than necessary, translating into unnecessary costs. This can be verified by referring to equation 4.6. The dimensionless critical shear stress also increases at high Froude numbers. The ceramic and glass ball data show that τ_{cr}^* remains constant for Froude numbers up to 0.5, approximately, and steadily increases above this point. In the case of the viton and teflon balls, τ_{cr}^* remains constant up to a Froude number of about 0.4. Interestingly enough, no changes were seen in the velocity distribution as a function of relative depth and Froude number. The integral constant, B, in the log-law averaged 9.64 with a narrow standard deviation of 0.6.

The trends observed in this study agree with the results obtained by previous researchers. However, the single plot showing τ_{cr}^* as a function of both relative depth and Froude number offers a more complete picture than shown by earlier research. Also, the fact that fully exposed spherical particles were used is advantageous because the effects of the free surface are isolated. Although the present experiments show interesting trends, their purpose is mainly to demonstrate the behavior of sediment at critical shallow flow conditions. The τ_{cr}^* values obtained are not applicable to riprap because fully exposed spherical particles were used in this study. Plenty of natural gravel data is available to create a single plot like the one suggested here. However, careful attention must be placed to the exact conditions in which each experiment was performed.

References

- Abt, S.R., Wittler, R.J., Ruff, J.F., LaGrone, D.L., Khattak, M.S., Nelson, J.D., Hinkle, N.E., and Lee, D.W. (1988). "Development of riprap design criteria by riprap testing in flumes : Phase II. Follow-up investigations." US Nuclear Regulatory Commission, NUREG/CR4651, ORNL/TM-10100/V2, Vol.2, September.
- Ackers, P. (1964). "Experiments on small streams in alluvium." *Journal of the Hydraulics Division*, ASCE, Vol.90, No.HY4, 1-37.
- Ackers, P., and White, W. (1973). "Sediment transport: New approach and analysis." *Journal of the Hydraulics Division*, ASCE, Vol.99, No.HY11, 2041-2060.
- Aguirre-Pe, J. (1975). "Incipient erosion in high gradient open channel flow with artificial roughness elements." *Proceedings of the 16th Congress of the International Association for Hydraulic Research*, Sao Paulo, Brazil, 2, 173-180.
- Aksoy, S. (1973). "The influence of the relative depth on threshold of grain motion." International Symposium on River Mechanics, Bangkok, Thailand, paper A-32, 359-370.
- Ashida, K., and Bayazit, M. (1973). "Initiation of motion and roughness of flows in steep channels." *Proceedings of the 15th Congress of the International Association for Hydraulic Research*, Istanbul, Turkey, 1, 475-484.
- Balakrishnan, M. (1997). "The role of turbulence on the entrainment of a single sphere and the effects of roughness on fluid-solid interaction." Ph.D Dissertation, Virginia Polytechnic Institute and State University, Blacksburg, VA.
- Bartnik, W. (1991). "Determination of the critical conditions of incipient motion of bed load in mountain rivers." Lecture Notes in Earth Sciences. Edited by A.Armanini and G.DiSilvio, Springer-Verlag, Berlin, 83-88.
- Bathurst, J.C. (1978). "Flow resistance of large-scale roughness." *Journal of the Hydraulics Division*, ASCE, Vol. 104, No. HY12, 1587-1603.
- Bathurst, J.C., Li, R-M., and Simons, D.B. (1979). "Hydraulics of mountain rivers." Report No. CER78-79JCB-RML-DBS55, Civil Engineering Department, Colorado State University, Fort Collins, Colorado.
- Bathurst, J.C., Graf, W.H., and Cao, H.H. (1982). "Initiation of sediment transport in steep channels with coarse bed material." *Euromech 156 : Mechanics of Sediment Transport*, Istanbul, Turkey, 207-213.
- Bayazit, M. (1982). "Flow structure and sediment transport mechanics in steep channels." *Euromech 156 : Mechanics of Sediment Transport*, Istanbul, Turkey, 197-206.

- Bettess, R. (1984). "Initiation of sediment transport in gravel streams." *Proceedings of the Institution of the Civil Engineers*, Part 2, 79-88.
- Cantwell, B.J. (1981). "Organized Motion in Turbulent Flow." *Annual Review of Fluid Mechanics*, Vol.13, 457-515.
- Cao, H.H. (1985). "Etude experimentale des ecoulement dans un canal a pente raide et avec lit a gravier." Thesis No. 589, Ecole Polytechnique Federale de Lausanne, Lausanne, Switzerland.
- Cardoso, A.H., Graf, W.H., and Gust,G. (1989). "Uniform flow in a smooth open channel." *Journal of Hydraulic Research*, 27(5), 603-615.
- Cheng, E.D.H. (1969). "Incipient motion of large roughness elements in turbulent open channel flow." Ph.D Dissertation, Utah State University, Logan, Utah.
- Clauser, F.H. (1954). "Turbulent boundary layer." *Advanced Applied Mechanics*, Vol.IV, p1.
- Coleman, N.L. (1967). "A theoretical and experimental study of drag and lift forces acting on a sphere resting on a hypothetical stream bed." *Proceedings of the 12th Congress of the International Association for Hydraulic Research*, Fort Collins, CO, Vol. 3, 185-192.
- Dean, R.B. (1978). "Reynolds number dependence of skin friction and other bulk flow variables in two-dimensional rectangular duct flow." *Journal of Fluids Engineering*, ASME, Vol.100, 215-223.
- Diplas, P. (1990). "Characteristics of self-formed straight channels." *Journal of Hydraulic Engineering*, Vol. 116, No.5, 707-728.
- Einstein, H.A., and El-Samni, E.A. (1949). "Hydrodynamic forces on a rough wall." *Reviews of Modern Physics*, 31(3), 520-524.
- Einstein, H.A., and Barbarossa, N.L. (1953). Transaction Paper 2528, ASCE.
- Fenton, J.D., and Abbott, J.E. (1977). "Initial movement of grains on a stream bed: The effect of relative protrusion." *Proceedings of the Royal Society of London*, Series A, Vol.352, 523-537.
- Gilbert, G.K. (1914). "The transportation of debris by running water." Professional Paper 86, U.S. Geological Survey, Washington DC.
- GKY & Associates (1993). "Lab Report on Scour Protection Alternatives at Bridge Piers." FHWA

- Graf, W.H., and Suszka, L. (1987). "Sediment transport in steep channels." *Journal of Hydroscience and Hydraulic Engineering*, Vol.5, No.1, 11-26.
- Grant, G.E. (1997). "Critical flow constraints flow hydraulics in mobile-bed streams: A new hypothesis." *Water Resources Research*, Vol.33, No.2, 349-358.
- Hey, R.D. (1979). "Flow resistance in gravel-bed rivers." *Journal of the Hydraulics Division, ASCE*, Vol. 105, No. HY4, 365-379.
- Ho Pang-Yung (1939). "Abhängigkeit der geschiebebewegung von der kornform und der temperature." *Mitteilungen der Preussischen Versuchsanstalt für Wasserbau und Schiffbau*, Berlin, Vol. 37.
- Jarrett, R.D. (1984). "Hydraulics of high-gradient streams." *Journal of Hydraulic Engineering*, Vol.110, No.11, 1519-1539.
- Kamphuis, J.W. (1974). "Determination of sand roughness for fixed beds." *Journal of Hydraulic Research*, 12(2), 193-203.
- Kilgore, R.T, and Young, G.K. (1993). "Riprap incipient motion and Shields' parameter." *Hydraulic Engineering* 93, 1552-1557.
- Kirkgoz, M.S. (1989). "Turbulent velocity profiles for smooth and rough open channel flow." *Journal of Hydraulic Engineering*, Vol.115, No.11, 1543-1561.
- Li, C.H. (1965). "The criteria of threshold shearing stress and ripple formation (experimental results in glycerine flow)." Report No.70, Nanjin Hydraulic Research Institute (in Chinese).
- Ling, C.H. (1995). "Criteria for incipient motion of spherical sediment particles." *Journal of Hydraulic Engineering*, Vol.121, No.6, 472-478.
- Mansour-Tehrani, M. (1992). "Spatial distribution and scaling of bursting events in boundary layer turbulence over smooth and rough surfaces." Ph.D Thesis, London University.
- Meyer-Peter, E., and Muller, R. (1948). "Formulas for bed load transport." *Proceedings of the 2nd Meeting of the International Association for Hydraulic Structures Research*, Stockholm, 39-64.
- Mizuyama, T. (1977). "Bedload transport in steep channels." Ph.D Dissertation, Kyoto University, Kyoto, Japan.
- Monin, A.S., and Yaglom, A.M. (1975). "Statistical fluid mechanics." MIT Press, Cambridge, Mass.

- Moore, M.C. (1994). "Bedload transport : The effects of particle shape and an investigation of a wide range of transport rates." Master's Thesis, Virginia Polytechnic Institute and State University, Blacksburg, VA.
- Neill, C.R. (1967). "Mean velocity criterion for scour of coarse uniform bed material." *Proceedings of the 12th Congress of the International Association for Hydraulic Research*, Fort Collins, CO, Vol.3, 46-54.
- Nezu, I., and Rodi, W. (1986). "Open-channel flow measurements with a laser-Doppler anemometer." *Journal of Hydraulic Engineering*, Vol.112, No.5, 335-355.
- Nezu, I., and Nakagawa, H. (1993). "Turbulence in open-channel flows." IAHR, A.A.Balkema, Rotterdam, Netherlands.
- Nikuradse, J. (1932). "Gesetzmässigkeiten der turbulenten Stromung in glatten Rohren." *Forsch. Geb. Ing.-Wes.*, Heft 356, Berlin (in German).
- Nikuradse, J. (1933). "Stromungsgesetze in rauhen Rohren." *Forsch. Geb. Ing.-Wes.*, Heft 361, Berlin (in German).
- Nordin, C.F. (1964). Water-Supply Paper 1498-H, U.S. Geological Survey.
- Paintal, A.S. (1971). "Concept of critical shear stress in loose boundary open channels." *Journal of Hydraulic Research*, No.1, 91-113.
- Papanicolaou, A. (1997). "The role of turbulence on the initiation of sediment motion." Ph.D Dissertation, Virginia Polytechnic Institute and State University, Blacksburg, VA.
- Parola, A.C. (1991). "The stability of riprap used to protect bridge piers." Federal Highway Administration Publication No. FHWA-RD-91-063.
- Pazis, and Graf, W.H. (1977). "Erosion et deposition; un concept probabiliste." *Proceedings of the 17th Congress of the International Association for Hydraulic Research*, Baden-Baden., Vol.1, 39-46.
- Perry, E.A., and Joubert, N.P. (1963). "Rough-wall boundary layers in adverse pressure gradients." *Journal of Fluid Mechanics*, 17(2), 193-211.
- Peterson, A.W., and Howells, R.F. (1973). "A compendium of solids transport data for mobile boundary channels." Report No. HY-1973-ST3, University of Alberta, Calgary, Canada.
- Prinos, P., and Zeris, A. (1995). "Uniform flow in open channels with steep slopes." *Journal of Hydraulic Research*, Vol.33, No.5, 705-719.

Shields, A. (1936). "Anwendung der ahnlichkeitsmechanik und der turbulenzforschung auf die geschiebebewegung." *Mitteilungen der Preussischen Versuchsanstalt fur Wasserbau und Schiffbau*, No. 26, Berlin, Germany (English Translation by W.P. Ott and J.C. van Uchelen, California Institute of Technology, Pasadena, California, USA).

Suszka, L. (1987). "Sediment transport at steady and unsteady flow; A laboratory study." Thesis No. 704, Ecole Polytechnique Federale de Lausanne, Lausanne, Switzerland.

Suszka, L. (1991). "Modification of transport rate formula for steep channels." Lecture Notes in Earth Sciences. Edited by A.Armanini and G.DiSilvio, Springer-Verlag, Berlin, 59-70.

Tabata, S., and Ichinose, M. (1971). "An empirical study of critical tractive force of large gravel." *The SHIN-SABO* 79, May 1971.

Taylor, B.D., and Vanoni, V.A. (1972). "Temperature effects in low-transport, flat-bed flows." *Journal of the Hydraulics Division, ASCE*, No. 98, 1427-1445.

Thompson, S.M., and Campbell, P.L. (1979). "Hydraulics of a large channel paved with boulders." *Journal of Hydraulic Research*, Vol. 17, No. 4, 341-354.

Thorne, C.R., and Zevenbergen, L.W. (1985). "Estimating mean velocity in mountain rivers." *Journal of Hydraulic Engineering*, Vol.111, No.4, 612-624.

Tominaga, A., and Nezu, I. (1992). "Velocity profiles in steep open-channel flows." *Journal of Hydraulic Engineering*, Vol.118, No.1, 73-90.

Trieste, D.J. (1992). "Evaluation of supercritical / subcritical flows in high-gradient channel." *Journal of Hydraulic Engineering*, Vol.118, No.8, 1107-1118.

U.S. Army Corps of Engineers (1935). "Studies of river bed materials and their movement with special references to the lower Mississippi River." U.S. Waterways Experiment Station, Vicksburg, MS, Paper No.17, p161.

van Rijn, L.C. (1982). "Equivalent roughness of alluvial bed." *Journal of the Hydraulics Division, ASCE*, Vol.108, No.HY10, 1215-1218.

Wahl, K.L (1993). "Variation of Froude number with discharge for large-gradient streams." *Hydraulic Engineering'93*, 1517-1522.

Wang, S. Y. (1975). "Stability of alluvial rivers." Technical Report, Tianjin University (in Chinese).

Wang, S., and Shen, H.W. (1985). "Incipient sediment motion and riprap design." *Journal of Hydraulic Engineering*, Vol.111, No.3, 520-538.

Wigley, W.C.S. (1953). "Water forces on submerged bodies in motion." *Transactions of the Institute of Naval Architecture*, No. 95, p.268.

Wittler, R.J., and Abt, S.R. (1995). "Shields parameter in low submergence or steep flows." *River, Coastal and Shoreline Protection : Erosion Control Using Riprap and Armourstone*, Edited by C.R. Thorne, S.R. Abt, F.B.J Barends, S.T. Maynard and K.W. Pilarczyk. John Wiley & Sons Ltd., 93-101.

Appendix 1.

This appendix contains a summary page for each of the 34 experiments run at threshold conditions. Each summary includes a table that shows the number of particles entrained during each minute of the experiment, the date in which the experiment was performed, slope, water depth, pump speed, gate configuration (rods), the head differential in the manometer, water discharge, depth-averaged velocity, bursting period, probability of entrainment, the $P_E/P_{E_{crit}}$ ratio, Froude number, densimetric Froude number, particle Reynolds number, dimensionless critical shear stress, and comments, if any.

Tables A.1-A.29 summarize the experiments that consider the bursting period as part of the incipient motion criterion. Tables A.30 and A.31 summarize the experiments that do not consider the bursting period. These two experiments have a “T_B” in front of their label (i.e D3T_B). Experiments A3 (Table A.3) and B3 (Table A.7) were used for both types of analysis. The summary tables for these four experiments also include the f_{avg}/f_{avg_crit} ratio. Finally, Tables A.32-A.34 summarize the experiments with the M1 water-surface profile. These include an “M1” in front of their label (i.e B2M1). The flow depth in this case is given for 3 measuring stations along the test section. Station H₄ is the one farthest upstream and station H₆ is the one farthest downstream.

Table A.1 Frequency of particle displacements at threshold conditions for experiment A1 (viton balls $H/D_{50} = 2$).

Time Period, Δt_i (minutes)	Fraction Displaced N_E/N_T	Fraction Displaced N_E/N_T (decimal)	Frequency of Displacement, f_i (1/s)
0-1	2/64	0.03125	0.000520833
1-2	1/62	0.016129032	0.000268817
2-3	2/61	0.032786885	0.000546448
3-4	4/61	0.06557377	0.001092896
4-5	0/60	0	0
5-6	0/60	0	0
6-7	0/61	0	0
7-8	0/61	0	0
8-9	2/61	0.032786885	0.000546448
9-10	2/60	0.033333333	0.000555556
10-11	1/59	0.016949153	0.000282486
11-12	0/59	0	0
12-13	2/59	0.033898305	0.000564972
13-14	0/59	0	0
14-15	1/60	0.016666667	0.000277778
15-16	1/59	0.016949153	0.000282486
16-17	1/59	0.016949153	0.000282486
17-18	1/59	0.016949153	0.000282486
18-19	1/59	0.016949153	0.000282486
19-20	0/59	0	0

$$f_{avg} = 2.89 \times 10^{-4}$$

Date of Experiment : July 27, 1997

Slope, S (%) : 0.3

Flow Depth, H (cm) : 1.6

Pump No.1 Speed (Hz) : 14.0

Gate Configuration (Rods) : 2 (3/10)''

Δh (mm) for Air/Water Manometer : 7.5

Water Discharge, Q (m³/s) : 0.00265

Depth-Averaged Velocity, V (m/s) : 0.274

Bursting Period, T_B (s) : 0.351

Probability of Entrainment, P_E : 1.104×10^{-4}

P_E/P_{Ecrit} : 1.00

Froude Number : 0.691

Densimetric Froude Number : 0.758

Particle Reynolds Number : 189

Dimensionless Critical Shear Stress : 0.00723

Comments : none

Table A.2 Frequency of particle displacements at threshold conditions for experiment A2 (teflon balls $H/D_{50} = 2$).

Time Period, Δt_i (minutes)	Fraction Displaced N_E/N_T	Fraction Displaced N_E/N_T (decimal)	Frequency of Displacement, f_i (1/s)
0-1	0/59	0	0
1-2	4/59	0.06779661	0.001129944
2-3	0/58	0	0
3-4	2/58	0.034482759	0.000574713
4-5	0/58	0	0
5-6	2/60	0.033333333	0.000555556
6-7	3/60	0.05	0.000833333
7-8	0/60	0	0
8-9	0/60	0	0
9-10	1/60	0.016666667	0.000277778
10-11	0/60	0	0
11-12	0/60	0	0
12-13	2/60	0.033333333	0.000555556
13-14	0/59	0	0
14-15	2/59	0.033898305	0.000564972
15-16	1/59	0.016949153	0.000282486
16-17	0/58	0	0
17-18	1/58	0.017241379	0.000287356
18-19	0/58	0	0
19-20	1/58	0.017241379	0.000287356

$$f_{avg} = 2.67 \times 10^{-4}$$

Date of Experiment : July 29, 1997
Slope, S (%) : 0.6
Flow Depth, H (cm) : 1.6
Pump No.1 Speed (Hz) : 15.3
Gate Configuration (Rods) : 2 (3/10)''
 Δh (mm) for Air/Water Manometer : 10
Water Discharge, Q (m³/s) : 0.00306
Depth-Averaged Velocity, V (m/s) : 0.316
Bursting Period, T_B (s) : 0.304
Probability of Entrainment, P_E : 8.122×10^{-5}
P_E/P_{Ecrit} : 0.80
Froude Number : 0.798
Densimetric Froude Number : 0.757
Particle Reynolds Number : 268
Dimensionless Critical Shear Stress : 0.0108
Comments : none

Table A.3 Frequency of particle displacements at threshold conditions for experiment A3 (glass balls $H/D_{50} = 2$).

Time Period, Δt_i (minutes)	Fraction Displaced N_E/N_T	Fraction Displaced N_E/N_T (decimal)	Frequency of Displacement, f_i (1/s)
0-1	3/64	0.046875	0.00078125
1-2	1/62	0.016129032	0.000268817
2-3	4/62	0.064516129	0.001075269
3-4	1/61	0.016393443	0.000273224
4-5	3/61	0.049180328	0.000819672
5-6	0/60	0	0
6-7	2/60	0.033333333	0.000555556
7-8	0/61	0	0
8-9	0/61	0	0
9-10	0/61	0	0
10-11	0/62	0	0
11-12	0/62	0	0
12-13	3/62	0.048387097	0.000806452
13-14	3/62	0.048387097	0.000806452
14-15	0/62	0	0
15-16	0/62	0	0
16-17	1/62	0.016129032	0.000268817
17-18	0/62	0	0
18-19	1/62	0.016129032	0.000268817
19-20	0/62	0	0

$$f_{avg} = 2.96 \times 10^{-4}$$

Date of Experiment : July 29, 1997

Slope, S (%) : 0.9

Flow Depth, H (cm) : 1.6

Pump No.1 Speed (Hz) : 16.2

Gate Configuration (Rods) : 2 (3/10)''

Δh (mm) for Air/Water Manometer : 11.5

Water Discharge, Q (m³/s) : 0.00328

Depth-Averaged Velocity, V (m/s) : 0.339

Bursting Period, T_B (s) : 0.283

Probability of Entrainment, P_E : 8.388×10^{-5}

P_E/P_{Ecrit} : 0.83

f_{avg}/f_{avg_crit} : 1.02

Froude Number : 0.856

Densimetric Froude Number : 0.679

Particle Reynolds Number : 328

Dimensionless Critical Shear Stress : 0.0113

Comments : none

Table A.4 Frequency of particle displacements at threshold conditions for experiment A4 (ceramic balls $H/D_{50} = 2$).

Time Period, Δt_i (minutes)	Fraction Displaced N_E/N_T	Fraction Displaced N_E/N_T (decimal)	Frequency of Displacement, f_i (1/s)
0-1	2/58	0.034482759	0.000574713
1-2	1/57	0.01754386	0.000292398
2-3	0/56	0	0
3-4	0/56	0	0
4-5	1/56	0.017857143	0.000297619
5-6	0/57	0	0
6-7	2/57	0.035087719	0.000584795
7-8	0/57	0	0
8-9	1/57	0.01754386	0.000292398
9-10	1/56	0.017857143	0.000297619
10-11	3/56	0.053571429	0.000892857
11-12	1/55	0.018181818	0.00030303
12-13	3/54	0.055555556	0.000925926
13-14	2/53	0.037735849	0.000628931
14-15	3/51	0.058823529	0.000980392

$$f_{avg} = 4.05 \times 10^{-4}$$

Date of Experiment : February 3, 1998

Slope, S (%) : 1.65

Flow Depth, H (cm) : 1.6

Pump No.1 Speed (Hz) : 20.9

Gate Configuration (Rods) : 2 (3/10)''

Δh (mm) for Air/Water Manometer : 26

Water Discharge, Q (m³/s) : 0.00493

Depth-Averaged Velocity, V (m/s) : 0.510

Bursting Period, T_B (s) : 0.188

Probability of Entrainment, P_E : 7.622×10^{-5}

P_E/P_{Ecrit} : 0.75

Froude Number : 1.29

Densimetric Froude Number : 0.769

Particle Reynolds Number : 444

Dimensionless Critical Shear Stress : 0.0118

Comments : This test is not within the required $\pm 20\%$ of P_{Ecrit} because the motion for this case was too massive.

Table A.5 Frequency of particle displacements at threshold conditions for experiment B1 (viton balls $H/D_{50} = 3$).

Time Period, Δt_i (minutes)	Fraction Displaced N_E/N_T	Fraction Displaced N_E/N_T (decimal)	Frequency of Displacement, f_i (1/s)
0-1	1/57	0.01754386	0.000292398
1-2	1/57	0.01754386	0.000292398
2-3	0/57	0	0
3-4	1/57	0.01754386	0.000292398
4-5	0/57	0	0
5-6	1/57	0.01754386	0.000292398
6-7	0/57	0	0
7-8	1/57	0.01754386	0.000292398
8-9	1/57	0.01754386	0.000292398
9-10	0/57	0	0
10-11	2/57	0.035087719	0.000584795
11-12	0/57	0	0
12-13	0/57	0	0
13-14	0/57	0	0
14-15	1/57	0.01754386	0.000292398
15-16	0/57	0	0
16-17	1/57	0.01754386	0.000292398
17-18	1/56	0.017857143	0.000297619
18-19	1/56	0.017857143	0.000297619
19-20	1/56	0.017857143	0.000297619

$$f_{avg} = 1.91 \times 10^{-4}$$

Date of Experiment : August 1, 1997
Slope, S (%) : 0.15
Flow Depth, H (cm) : 2.4
Pump No.1 Speed (Hz) : 16.4
Gate Configuration (Rods) : 3 (3/10)''
 Δh (mm) for Air/Water Manometer : 16
Water Discharge, Q (m³/s) : 0.00387
Depth-Averaged Velocity, V (m/s) : 0.267
Bursting Period, T_B (s) : 0.540
Probability of Entrainment, P_E : 1.030×10^{-4}
P_E/P_{Ecrit} : 1.02
Froude Number : 0.549
Densimetric Froude Number : 0.603
Particle Reynolds Number : 162
Dimensionless Critical Shear Stress : 0.00542
Comments : none

Table A.6 Frequency of particle displacements at threshold conditions for experiment B2 (teflon balls $H/D_{50} = 3$).

Time Period, Δt_i (minutes)	Fraction Displaced N_E/N_T	Fraction Displaced N_E/N_T (decimal)	Frequency of Displacement, f_i (1/s)
0-1	2/68	0.029411765	0.000490196
1-2	1/66	0.015151515	0.000252525
2-3	2/66	0.03030303	0.000505051
3-4	1/66	0.015151515	0.000252525
4-5	0/66	0	0
5-6	0/66	0	0
6-7	3/66	0.045454545	0.000757576
7-8	1/66	0.015151515	0.000252525
8-9	2/67	0.029850746	0.000497512
9-10	1/66	0.015151515	0.000252525
10-11	0/66	0	0
11-12	0/66	0	0
12-13	0/66	0	0
13-14	3/66	0.045454545	0.000757576
14-15	1/66	0.015151515	0.000252525
15-16	0/66	0	0
16-17	0/66	0	0
17-18	0/66	0	0
18-19	0/66	0	0
19-20	0/66	0	0

$$f_{avg} = 2.14 \times 10^{-4}$$

Date of Experiment : April 14, 1998
Slope, S (%) : 0.29
Flow Depth, H (cm) : 2.4
Pump No.1 Speed (Hz) : 19.8
Gate Configuration (Rods) : 2 (3/10)" , 1 (1/4) "
 Δh (mm) for Air/Water Manometer : 23.5
Water Discharge, Q (m³/s) : 0.00469
Depth-Averaged Velocity, V (m/s) : 0.323
Bursting Period, T_B (s) : 0.446
Probability of Entrainment, P_E : 9.517×10^{-5}
P_E/P_{Ecrit} : 0.94
Froude Number : 0.666
Densimetric Froude Number : 0.632
Particle Reynolds Number : 225
Dimensionless Critical Shear Stress : 0.00784
Comments : none

Table A.7 Frequency of particle displacements at threshold conditions for experiment B3 (glass balls $H/D_{50} = 3$).

Time Period, Δt_i (minutes)	Fraction Displaced N_E/N_T	Fraction Displaced N_E/N_T (decimal)	Frequency of Displacement, f_i (1/s)
0-1	2/68	0.029411765	0.000490196
1-2	2/68	0.029411765	0.000490196
2-3	5/67	0.074626866	0.001243781
3-4	0/67	0	0
4-5	0/67	0	0
5-6	2/67	0.029850746	0.000497512
6-7	0/67	0	0
7-8	0/67	0	0
8-9	3/67	0.044776119	0.000746269
9-10	0/66	0	0
10-11	2/66	0.03030303	0.000505051
11-12	0/66	0	0
12-13	0/66	0	0
13-14	0/66	0	0
14-15	0/66	0	0
15-16	1/66	0.015151515	0.000252525
16-17	0/66	0	0
17-18	2/66	0.03030303	0.000505051
18-19	1/66	0.015151515	0.000252525
19-20	3/66	0.045454545	0.000757576

$$f_{avg} = 2.87 \times 10^{-4}$$

Date of Experiment : April 10, 1998

Slope, S (%) : 0.44

Flow Depth, H (cm) : 2.4

Pump No.1 Speed (Hz) : 20.9

Gate Configuration (Rods) : 2 (3/10)" , 1 (1/4) "

Δh (mm) for Air/Water Manometer : 31.5

Water Discharge, Q (m³/s) : 0.00543

Depth-Averaged Velocity, V (m/s) : 0.374

Bursting Period, T_B (s) : 0.385

Probability of Entrainment, P_E : 1.105×10^{-4}

P_E/P_{Ecrit} : 1.09

f_{avg}/f_{avg_crit} : 0.99

Froude Number : 0.771

Densimetric Froude Number : 0.611

Particle Reynolds Number : 277

Dimensionless Critical Shear Stress : 0.00830

Comments : In the movie, the slope was mistakenly recorded as 0.45%.

Table A.8 Frequency of particle displacements at threshold conditions for experiment B4 (ceramic balls $H/D_{50} = 3$).

Time Period, Δt_i (minutes)	Fraction Displaced N_E/N_T	Fraction Displaced N_E/N_T (decimal)	Frequency of Displacement, f_i (1/s)
0-1	3/61	0.049180328	0.000819672
1-2	2/61	0.032786885	0.000546448
2-3	2/61	0.032786885	0.000546448
3-4	0/61	0	0
4-5	2/61	0.032786885	0.000546448
5-6	3/61	0.049180328	0.000819672
6-7	1/61	0.016393443	0.000273224
7-8	0/62	0	0
8-9	2/62	0.032258065	0.000537634
9-10	1/62	0.016129032	0.000268817
10-11	2/61	0.032786885	0.000546448
11-12	3/59	0.050847458	0.000847458
12-13	1/59	0.016949153	0.000282486
13-14	0/58	0	0
14-15	0/58	0	0
15-16	0/58	0	0
16-17	1/58	0.017241379	0.000287356
17-18	1/58	0.017241379	0.000287356
18-19	1/58	0.017241379	0.000287356
19-20	1/58	0.017241379	0.000287356

$$f_{avg} = 3.59 \times 10^{-4}$$

Date of Experiment : April 23, 1998
Slope, S (%) : 0.97
Flow Depth, H (cm) : 2.4
Pump No.1 Speed (Hz) : 25.5
Gate Configuration (Rods) : 2 (3/10)''
 Δh (mm) for Air/Water Manometer : 63.5
Water Discharge, Q (m³/s) : 0.00771
Depth-Averaged Velocity, V (m/s) : 0.531
Bursting Period, T_B (s) : 0.271
Probability of Entrainment, P_E : 9.740×10^{-5}
P_E/P_{Ecrit} : 0.96
Froude Number : 1.09
Densimetric Froude Number : 0.654
Particle Reynolds Number : 412
Dimensionless Critical Shear Stress : 0.0104
Comments : none

Table A.9 Frequency of particle displacements at threshold conditions for experiment C1 (viton balls $H/D_{50} = 4$).

Time Period, Δt_i (minutes)	Fraction Displaced N_E/N_T	Fraction Displaced N_E/N_T (decimal)	Frequency of Displacement, f_i (1/s)
0-1	2/63	0.031746032	0.000529101
1-2	1/63	0.015873016	0.00026455
2-3	1/63	0.015873016	0.00026455
3-4	2/63	0.031746032	0.000529101
4-5	0/63	0	0
5-6	1/63	0.015873016	0.00026455
6-7	1/63	0.015873016	0.00026455
7-8	0/63	0	0
8-9	1/63	0.015873016	0.00026455
9-10	0/63	0	0
10-11	0/63	0	0
11-12	0/63	0	0
12-13	0/63	0	0
13-14	0/63	0	0
14-15	0/63	0	0
15-16	1/63	0.015873016	0.00026455
16-17	0/63	0	0
17-18	0/63	0	0
18-19	0/63	0	0
19-20	1/63	0.015873016	0.00026455

$$f_{avg} = 1.46 \times 10^{-4}$$

Date of Experiment : April 17, 1998

Slope, S (%) : 0.06

Flow Depth, H (cm) : 3.2

Pump No.1 Speed (Hz) : 20.5

Gate Configuration (Rods) : 3 (3/10)" , 1 square rod (tied)

Δh (mm) for Air/Water Manometer : 29.5

Water Discharge, Q (m³/s) : 0.00526

Depth-Averaged Velocity, V (m/s) : 0.271

Bursting Period, T_B (s) : 0.707

Probability of Entrainment, P_E : 1.029×10^{-4}

P_E/P_{Ecrit} : 1.01

Froude Number : 0.485

Densimetric Froude Number : 0.532

Particle Reynolds Number : 117

Dimensionless Critical Shear Stress : 0.00289

Comments : This test should start 32 seconds before the "begin" signal in the video.

Table A.10 Frequency of particle displacements at threshold conditions for experiment C2 (teflon balls $H/D_{50} = 4$).

Time Period, Δt_i (minutes)	Fraction Displaced N_E/N_T	Fraction Displaced N_E/N_T (decimal)	Frequency of Displacement, f_i (1/s)
0-1	2/65	0.030769231	0.000512821
1-2	1/65	0.015384615	0.00025641
2-3	1/65	0.015384615	0.00025641
3-4	0/65	0	0
4-5	2/65	0.030769231	0.000512821
5-6	1/65	0.015384615	0.00025641
6-7	0/65	0	0
7-8	0/65	0	0
8-9	1/65	0.015384615	0.00025641
9-10	0/65	0	0
10-11	0/65	0	0
11-12	1/65	0.015384615	0.00025641
12-13	1/65	0.015384615	0.00025641
13-14	0/65	0	0
14-15	0/65	0	0
15-16	1/65	0.015384615	0.00025641
16-17	1/65	0.015384615	0.00025641
17-18	0/65	0	0
18-19	0/65	0	0
19-20	0/65	0	0

$$f_{avg} = 1.54 \times 10^{-4}$$

Date of Experiment : January 19, 1998

Slope, S (%) : 0.1

Flow Depth, H (cm) : 3.2

Pump No.1 Speed (Hz) : 20.3

Gate Configuration (Rods) : 3 (3/10)''

Δh (mm) for Air/Water Manometer : 36.5

Water Discharge, Q (m³/s) : 0.00585

Depth-Averaged Velocity, V (m/s) : 0.302

Bursting Period, T_B (s) : 0.636

Probability of Entrainment, P_E : 9.782×10^{-5}

P_E/P_{Ecrit} : 0.96

Froude Number : 0.539

Densimetric Froude Number : 0.512

Particle Reynolds Number : 151

Dimensionless Critical Shear Stress : 0.0036

Comments : This test started at S = 0.08 % and was then increased to S = 0.10 % right before threshold conditions were reached.

Table A.11 Frequency of particle displacements at threshold conditions for experiment C3 (glass balls $H/D_{50} = 4$).

Time Period, Δt_i (minutes)	Fraction Displaced N_E/N_T	Fraction Displaced N_E/N_T (decimal)	Frequency of Displacement, f_i (1/s)
0-1	0/65	0	0
1-2	0/65	0	0
2-3	2/65	0.030769231	0.000512821
3-4	2/65	0.030769231	0.000512821
4-5	1/65	0.015384615	0.00025641
5-6	2/65	0.030769231	0.000512821
6-7	0/65	0	0
7-8	1/65	0.015384615	0.00025641
8-9	1/65	0.015384615	0.00025641
9-10	0/65	0	0
10-11	0/65	0	0
11-12	0/65	0	0
12-13	2/65	0.030769231	0.000512821
13-14	1/65	0.015384615	0.00025641
14-15	1/65	0.015384615	0.00025641
15-16	0/65	0	0
16-17	0/65	0	0
17-18	1/65	0.015384615	0.00025641
18-19	1/65	0.015384615	0.00025641
19-20	0/65	0	0

$$f_{avg} = 1.92 \times 10^{-4}$$

Date of Experiment : August 13, 1997

Slope, S (%) : 0.28

Flow Depth, H (cm) : 3.2

Pump No.1 Speed (Hz) : 21.4

Gate Configuration (Rods) : 3 (3/10)''

Δh (mm) for Air/Water Manometer : 48.5

Water Discharge, Q (m³/s) : 0.00674

Depth-Averaged Velocity, V (m/s) : 0.348

Bursting Period, T_B (s) : 0.552

Probability of Entrainment, P_E : 1.060×10^{-4}

P_E/P_{Ecrit} : 1.05

Froude Number : 0.621

Densimetric Froude Number : 0.493

Particle Reynolds Number : 252

Dimensionless Critical Shear Stress : 0.00704

Comments : none

Table A.12 Frequency of particle displacements at threshold conditions for experiment C4 (ceramic balls $H/D_{50} = 4$).

Time Period, Δt_i (minutes)	Fraction Displaced N_E/N_T	Fraction Displaced N_E/N_T (decimal)	Frequency of Displacement, f_i (1/s)
0-1	2/62	0.032258065	0.000537634
1-2	4/61	0.06557377	0.001092896
2-3	1/61	0.016393443	0.000273224
3-4	0/61	0	0
4-5	3/61	0.049180328	0.000819672
5-6	0/61	0	0
6-7	0/61	0	0
7-8	0/61	0	0
8-9	0/61	0	0
9-10	1/61	0.016393443	0.000273224
10-11	2/61	0.032786885	0.000546448
11-12	2/61	0.032786885	0.000546448
12-13	0/61	0	0
13-14	0/61	0	0
14-15	0/61	0	0
15-16	1/61	0.016393443	0.000273224
16-17	0/61	0	0
17-18	2/61	0.032786885	0.000546448
18-19	0/61	0	0
19-20	1/61	0.016393443	0.000273224

$$f_{avg} = 2.59 \times 10^{-4}$$

Date of Experiment : January 30, 1998

Slope, S (%) : 0.62

Flow Depth, H (cm) : 3.2

Pump No.1 Speed (Hz) : 28.0

Gate Configuration (Rods) : 2 (3/10)''

Δh (mm) for Air/Water Manometer : 100

Water Discharge, Q (m³/s) : 0.00968

Depth-Averaged Velocity, V (m/s) : 0.500

Bursting Period, T_B (s) : 0.384

Probability of Entrainment, P_E : 9.954×10^{-5}

P_E/P_{Ecrit} : 0.981

Froude Number : 0.892

Densimetric Froude Number : 0.533

Particle Reynolds Number : 375

Dimensionless Critical Shear Stress : 0.00886

Comments : This test started at S = 0.60 % and was then increased to S = 0.62 % right before threshold conditions were reached.

Table A.13 Frequency of particle displacements at threshold conditions for experiment D1 (viton balls $H/D_{50} = 5$).

Time Period, Δt_i (minutes)	Fraction Displaced N_E/N_T	Fraction Displaced N_E/N_T (decimal)	Frequency of Displacement, f_i (1/s)
0-1	2/67	0.029850746	0.000497512
1-2	0/67	0	0
2-3	0/67	0	0
3-4	0/67	0	0
4-5	0/67	0	0
5-6	0/67	0	0
6-7	0/67	0	0
7-8	2/67	0.029850746	0.000497512
8-9	0/67	0	0
9-10	0/67	0	0
10-11	2/67	0.029850746	0.000497512
11-12	0/67	0	0
12-13	1/67	0.014925373	0.000248756
13-14	1/67	0.014925373	0.000248756
14-15	0/67	0	0
15-16	1/67	0.014925373	0.000248756
16-17	0/67	0	0
17-18	0/67	0	0
18-19	0/67	0	0
19-20	0/67	0	0

$$f_{avg} = 1.12 \times 10^{-4}$$

Date of Experiment : May 31, 1998
Slope, S (%) : 0.025
Flow Depth, H (cm) : 4.0
Pump No.1 Speed (Hz) : 23.0
Gate Configuration (Rods) : 4 (3/10)" , 1 square rod
 Δh (mm) for Air/Water Manometer : 45
Water Discharge, Q (m³/s) : 0.00649
Depth-Averaged Velocity, V (m/s) : 0.268
Bursting Period, T_B (s) : 0.895
Probability of Entrainment, P_E : 1.002×10^{-4}
P_E/P_{Ecrit} : 0.99
Froude Number : 0.428
Densimetric Froude Number : 0.470
Particle Reynolds Number : 83
Dimensionless Critical Shear Stress : 0.00151
Comments : none

Table A.14 Frequency of particle displacements at threshold conditions for experiment D2 (teflon balls $H/D_{50} = 5$).

Time Period, Δt_i (minutes)	Fraction Displaced N_E/N_T	Fraction Displaced N_E/N_T (decimal)	Frequency of Displacement, f_i (1/s)
0-1	0/64	0	0
1-2	0/64	0	0
2-3	0/64	0	0
3-4	0/64	0	0
4-5	1/64	0.015625	0.000260417
5-6	1/64	0.015625	0.000260417
6-7	0/64	0	0
7-8	0/64	0	0
8-9	1/64	0.015625	0.000260417
9-10	1/65	0.015384615	0.00025641
10-11	0/65	0	0
11-12	0/65	0	0
12-13	2/65	0.030769231	0.000512821
13-14	1/65	0.015384615	0.00025641
14-15	0/65	0	0
15-16	0/65	0	0
16-17	1/65	0.015384615	0.00025641
17-18	0/65	0	0
18-19	1/65	0.015384615	0.00025641
19-20	1/65	0.015384615	0.00025641

$$f_{avg} = 1.29 \times 10^{-4}$$

Date of Experiment : March 2, 1998

Slope, S (%) : 0.08

Flow Depth, H (cm) : 4.0

Pump No.1 Speed (Hz) : 24.0

Gate Configuration (Rods) : 3 (3/10)" , 1 (1/4) "

Δh (mm) for Air/Water Manometer : 61

Water Discharge, Q (m³/s) : 0.00756

Depth-Averaged Velocity, V (m/s) : 0.312

Bursting Period, T_B (s) : 0.768

Probability of Entrainment, P_E : 9.899×10^{-5}

P_E/P_{Ecrit} : 0.98

Froude Number : 0.499

Densimetric Froude Number : 0.473

Particle Reynolds Number : 149

Dimensionless Critical Shear Stress : 0.00360

Comments : This test started at S = 0.06 % and was then increased to S = 0.08 % right before threshold conditions were reached.

Table A.15 Frequency of particle displacements at threshold conditions for experiment D3 (glass balls $H/D_{50} = 5$).

Time Period, Δt_i (minutes)	Fraction Displaced N_E/N_T	Fraction Displaced N_E/N_T (decimal)	Frequency of Displacement, f_i (1/s)
0-1	1/68	0.014705882	0.000245098
1-2	0/68	0	0
2-3	3/68	0.044117647	0.000735294
3-4	2/68	0.029411765	0.000490196
4-5	0/67	0	0
5-6	0/67	0	0
6-7	1/67	0.014925373	0.000248756
7-8	1/67	0.014925373	0.000248756
8-9	0/67	0	0
9-10	0/67	0	0
10-11	1/67	0.014925373	0.000248756
11-12	1/67	0.014925373	0.000248756
12-13	0/67	0	0
13-14	0/67	0	0
14-15	1/67	0.014925373	0.000248756
15-16	0/67	0	0
16-17	0/67	0	0
17-18	0/67	0	0
18-19	0/67	0	0
19-20	0/67	0	0

$$f_{avg} = 1.36 \times 10^{-4}$$

Date of Experiment : March 8, 1998
Slope, S (%) : 0.21
Flow Depth, H (cm) : 4.0
Pump No.1 Speed (Hz) : 25.6
Gate Configuration (Rods) : 3 (3/10)" , 1 (1/4) "
 Δh (mm) for Air/Water Manometer : 76
Water Discharge, Q (m³/s) : 0.00844
Depth-Averaged Velocity, V (m/s) : 0.349
Bursting Period, T_B (s) : 0.688
Probability of Entrainment, P_E : 9.344×10^{-5}
P_E/P_{Ecrit} : 0.92
Froude Number : 0.556
Densimetric Froude Number : 0.441
Particle Reynolds Number : 241
Dimensionless Critical Shear Stress : 0.0066
Comments : none

Table A.16 Frequency of particle displacements at threshold conditions for experiment D4 (ceramic balls $H/D_{50} = 5$).

Time Period, Δt_i (minutes)	Fraction Displaced N_E/N_T	Fraction Displaced N_E/N_T (decimal)	Frequency of Displacement, f_i (1/s)
0-1	0/62	0	0
1-2	3/62	0.048387097	0.000806452
2-3	0/62	0	0
3-4	0/62	0	0
4-5	2/62	0.032258065	0.000537634
5-6	2/61	0.032786885	0.000546448
6-7	1/61	0.016393443	0.000273224
7-8	0/61	0	0
8-9	2/61	0.032786885	0.000546448
9-10	1/61	0.016393443	0.000273224
10-11	2/61	0.032786885	0.000546448
11-12	0/60	0	0
12-13	0/60	0	0
13-14	0/60	0	0
14-15	0/60	0	0
15-16	0/60	0	0
16-17	0/60	0	0
17-18	0/60	0	0
18-19	1/60	0.016666667	0.000277778
19-20	1/60	0.016666667	0.000277778

$$f_{avg} = 2.04 \times 10^{-4}$$

Date of Experiment : March 9, 1998
Slope, S (%) : 0.43
Flow Depth, H (cm) : 4.0
Pump No.1 Speed (Hz) : 32.2
Gate Configuration (Rods) : 2 (3/10)" , 1 (1/4) "
 Δh (mm) for Air/Water Manometer : 158
Water Discharge, Q (m³/s) : 0.0122
Depth-Averaged Velocity, V (m/s) : 0.503
Bursting Period, T_B (s) : 0.477
Probability of Entrainment, P_E : 9.754×10^{-5}
P_E/P_{Ecrit} : 0.96
Froude Number : 0.80
Densimetric Froude Number : 0.48
Particle Reynolds Number : 345
Dimensionless Critical Shear Stress : 0.00768
Comments : none

Table A.17 Frequency of particle displacements at threshold conditions for experiment E1 (viton balls $H/D_{50} = 6$).

Time Period, Δt_i (minutes)	Fraction Displaced N_E/N_T	Fraction Displaced N_E/N_T (decimal)	Frequency of Displacement, f_i (1/s)
0-1	1/66	0.015151515	0.000252525
1-2	0/65	0	0
2-3	0/65	0	0
3-4	0/65	0	0
4-5	0/65	0	0
5-6	0/65	0	0
6-7	1/65	0.015384615	0.00025641
7-8	0/65	0	0
8-9	1/65	0.015384615	0.00025641
9-10	0/65	0	0
10-11	1/65	0.015384615	0.00025641
11-12	0/65	0	0
12-13	0/65	0	0
13-14	0/65	0	0
14-15	1/65	0.015384615	0.00025641
15-16	0/65	0	0
16-17	0/65	0	0
17-18	0/65	0	0
18-19	0/65	0	0
19-20	1/65	0.015384615	0.00025641

$$f_{avg} = 7.67 \times 10^{-5}$$

Date of Experiment : June 11, 1998

Slope, S (%) : 0.015

Flow Depth, H (cm) : 4.8

Pump No.1 Speed (Hz) : 24.3

Gate Configuration (Rods) : 4 (3/10)" , 1 (1/4) " , 1 square rod

Δh (mm) for Air/Water Manometer : 59.5

Water Discharge, Q (m³/s) : 0.00746

Depth-Averaged Velocity, V (m/s) : 0.257

Bursting Period, T_B (s) : 1.12

Probability of Entrainment, P_E : 8.597×10^{-5}

P_E/P_{Ecrit} : 0.85

Froude Number : 0.38

Densimetric Froude Number : 0.41

Particle Reynolds Number : 70

Dimensionless Critical Shear Stress : 0.00108

Comments : none

Table A.18 Frequency of particle displacements at threshold conditions for experiment E2 (teflon balls $H/D_{50} = 6$).

Time Period, Δt_i (minutes)	Fraction Displaced N_E/N_T	Fraction Displaced N_E/N_T (decimal)	Frequency of Displacement, f_i (1/s)
0-1	0/66	0	0
1-2	2/66	0.03030303	0.000505051
2-3	0/66	0	0
3-4	2/66	0.03030303	0.000505051
4-5	1/66	0.015151515	0.000252525
5-6	0/66	0	0
6-7	0/66	0	0
7-8	0/66	0	0
8-9	1/66	0.015151515	0.000252525
9-10	0/66	0	0
10-11	0/66	0	0
11-12	0/66	0	0
12-13	1/66	0.015151515	0.000252525
13-14	0/66	0	0
14-15	0/66	0	0
15-16	0/66	0	0
16-17	0/66	0	0
17-18	1/66	0.015151515	0.000252525
18-19	1/66	0.015151515	0.000252525
19-20	0/66	0	0

$$f_{avg} = 1.14 \times 10^{-4}$$

Date of Experiment : March 26, 1998

Slope, S (%) : 0.06

Flow Depth, H (cm) : 4.8

Pump No.1 Speed (Hz) : 26.6

Gate Configuration (Rods) : 4 (3/10)" , 1 square rod

Δh (mm) for Air/Water Manometer : 85

Water Discharge, Q (m³/s) : 0.00892

Depth-Averaged Velocity, V (m/s) : 0.307

Bursting Period, T_B (s) : 0.937

Probability of Entrainment, P_E : 1.065×10^{-4}

P_E/P_{Ecrit} : 1.05

Froude Number : 0.45

Densimetric Froude Number : 0.43

Particle Reynolds Number : 140

Dimensionless Critical Shear Stress : 0.00324

Comments : This test should start 50 seconds after the "begin" signal in the video. Also, the slope was increased from 0.04% to 0.06% right before reaching threshold conditions.

Table A.19 Frequency of particle displacements at threshold conditions for experiment E3 (glass balls $H/D_{50} = 6$).

Time Period, Δt_i (minutes)	Fraction Displaced N_E/N_T	Fraction Displaced N_E/N_T (decimal)	Frequency of Displacement, f_i (1/s)
0-1	1/63	0.015873016	0.00026455
1-2	0/63	0	0
2-3	1/63	0.015873016	0.00026455
3-4	0/63	0	0
4-5	1/63	0.015873016	0.00026455
5-6	0/63	0	0
6-7	0/63	0	0
7-8	0/63	0	0
8-9	2/63	0.031746032	0.000529101
9-10	1/63	0.015873016	0.00026455
10-11	0/63	0	0
11-12	0/63	0	0
12-13	0/63	0	0
13-14	0/63	0	0
14-15	0/63	0	0
15-16	0/63	0	0
16-17	1/63	0.015873016	0.00026455
17-18	0/63	0	0
18-19	0/63	0	0
19-20	1/63	0.015873016	0.00026455

$$f_{avg} = 1.06 \times 10^{-4}$$

Date of Experiment : April 3, 1998

Slope, S (%) : 0.165

Flow Depth, H (cm) : 4.8

Pump No.1 Speed (Hz) : 28.5

Gate Configuration (Rods) : 4 (3/10)" , 1 square rod

Δh (mm) for Air/Water Manometer : 105

Water Discharge, Q (m³/s) : 0.00992

Depth-Averaged Velocity, V (m/s) : 0.341

Bursting Period, T_B (s) : 0.843

Probability of Entrainment, P_E : 8.93×10^{-5}

P_E/P_{Ecrit} : 0.88

Froude Number : 0.50

Densimetric Froude Number : 0.40

Particle Reynolds Number : 232

Dimensionless Critical Shear Stress : 0.00623

Comments : This test should start 30 seconds after the "begin" signal in the video.

Table A.20 Frequency of particle displacements at threshold conditions for experiment E4 (ceramic balls $H/D_{50} = 6$).

Time Period, Δt_i (minutes)	Fraction Displaced N_E/N_T	Fraction Displaced N_E/N_T (decimal)	Frequency of Displacement, f_i (1/s)
0-1	1/64	0.015625	0.000260417
1-2	2/63	0.031746032	0.000529101
2-3	1/63	0.015873016	0.00026455
3-4	2/63	0.031746032	0.000529101
4-5	2/63	0.031746032	0.000529101
5-6	0/64	0	0
6-7	0/64	0	0
7-8	1/64	0.015625	0.000260417
8-9	0/64	0	0
9-10	0/64	0	0
10-11	0/64	0	0
11-12	1/65	0.015384615	0.00025641
12-13	0/65	0	0
13-14	1/65	0.015384615	0.00025641
14-15	1/65	0.015384615	0.00025641
15-16	0/65	0	0
16-17	2/65	0.030769231	0.000512821
17-18	0/64	0	0
18-19	1/64	0.015625	0.000260417
19-20	0/64	0	0

$$f_{avg} = 1.96 \times 10^{-4}$$

Date of Experiment : March 23, 1998

Slope, S (%) : 0.32

Flow Depth, H (cm) : 4.8

Pump No.1 Speed (Hz) : 36.3

Gate Configuration (Rods) : 3 (3/10)''

Δh (mm) for Air/Water Manometer : 233.5

Water Discharge, Q (m³/s) : 0.0148

Depth-Averaged Velocity, V (m/s) : 0.509

Bursting Period, T_B (s) : 0.566

Probability of Entrainment, P_E : 1.107×10^{-4}

P_E/P_{Ecrit} : 1.09

Froude Number : 0.74

Densimetric Froude Number : 0.44

Particle Reynolds Number : 323

Dimensionless Critical Shear Stress : 0.00686

Comments : This test should start 50 seconds after the “begin” signal in the video.

Table A.21 Frequency of particle displacements at threshold conditions for experiment F2 (teflon balls $H/D_{50} = 7$).

Time Period, Δt_i (minutes)	Fraction Displaced N_E/N_T	Fraction Displaced N_E/N_T (decimal)	Frequency of Displacement, f_i (1/s)
0-1	2/64	0.03125	0.000520833
1-2	2/64	0.03125	0.000520833
2-3	0/64	0	0
3-4	0/64	0	0
4-5	0/64	0	0
5-6	0/64	0	0
6-7	0/64	0	0
7-8	1/64	0.015625	0.000260417
8-9	0/64	0	0
9-10	0/64	0	0
10-11	0/64	0	0
11-12	0/64	0	0
12-13	1/64	0.015625	0.000260417
13-14	0/64	0	0
14-15	0/64	0	0
15-16	1/64	0.015625	0.000260417
16-17	0/64	0	0
17-18	1/64	0.015625	0.000260417
18-19	0/64	0	0
19-20	0/64	0	0

$$f_{avg} = 1.04 \times 10^{-4}$$

Date of Experiment : May 14, 1998

Slope, S (%) : 0.045

Flow Depth, H (cm) : 5.6

Pump No.1 Speed (Hz) : 29.5

Gate Configuration (Rods) : 4 (3/10)" , 1 (1/4) " , 1 square rod

Δh (mm) for Air/Water Manometer : 114.5

Water Discharge, Q (m³/s) : 0.0104

Depth-Averaged Velocity, V (m/s) : 0.306

Bursting Period, T_B (s) : 1.10

Probability of Entrainment, P_E : 1.145×10^{-4}

P_E/P_{Ecrit} : 1.13

Froude Number : 0.41

Densimetric Froude Number : 0.39

Particle Reynolds Number : 129

Dimensionless Critical Shear Stress : 0.00284

Comments : none

Table A.22 Frequency of particle displacements at threshold conditions for experiment F3 (glass balls $H/D_{50} = 7$).

Time Period, Δt_i (minutes)	Fraction Displaced N_E/N_T	Fraction Displaced N_E/N_T (decimal)	Frequency of Displacement, f_i (1/s)
0-1	2/63	0.031746032	0.000529101
1-2	0/63	0	0
2-3	1/63	0.015873016	0.00026455
3-4	0/63	0	0
4-5	0/63	0	0
5-6	0/63	0	0
6-7	0/63	0	0
7-8	0/63	0	0
8-9	1/63	0.015873016	0.00026455
9-10	1/63	0.015873016	0.00026455
10-11	2/63	0.031746032	0.000529101
11-12	0/63	0	0
12-13	0/63	0	0
13-14	1/63	0.015873016	0.00026455
14-15	0/63	0	0
15-16	0/63	0	0
16-17	0/63	0	0
17-18	0/64	0	0
18-19	0/64	0	0
19-20	0/64	0	0

$$f_{avg} = 1.06 \times 10^{-4}$$

Date of Experiment : May 13, 1998

Slope, S (%) : 0.135

Flow Depth, H (cm) : 5.6

Pump No.1 Speed (Hz) : 32.0

Gate Configuration (Rods) : 4 (3/10)" , 1 (1/4) "

Δh (mm) for Air/Water Manometer : 151.5

Water Discharge, Q (m³/s) : 0.0119

Depth-Averaged Velocity, V (m/s) : 0.352

Bursting Period, T_B (s) : 0.956

Probability of Entrainment, P_E : 1.011×10^{-4}

P_E/P_{Ecrit} : 1.00

Froude Number : 0.47

Densimetric Froude Number : 0.38

Particle Reynolds Number : 224

Dimensionless Critical Shear Stress : 0.00594

Comments : This test should start 2 minutes after the "begin" signal in the video.

Table A.23 Frequency of particle displacements at threshold conditions for experiment F4 (ceramic balls $H/D_{50} = 7$).

Time Period, Δt_i (minutes)	Fraction Displaced N_E/N_T	Fraction Displaced N_E/N_T (decimal)	Frequency of Displacement, f_i (1/s)
0-1	1/64	0.015625	0.000260417
1-2	2/64	0.03125	0.000520833
2-3	1/64	0.015625	0.000260417
3-4	0/64	0	0
4-5	0/64	0	0
5-6	2/64	0.03125	0.000520833
6-7	0/64	0	0
7-8	1/64	0.015625	0.000260417
8-9	0/64	0	0
9-10	0/64	0	0
10-11	0/64	0	0
11-12	0/64	0	0
12-13	3/64	0.046875	0.00078125
13-14	0/64	0	0
14-15	0/64	0	0
15-16	0/64	0	0
16-17	0/64	0	0
17-18	0/64	0	0
18-19	0/64	0	0
19-20	0/64	0	0

$$f_{avg} = 1.30 \times 10^{-4}$$

Date of Experiment : May 16, 1998

Slope, S (%) : 0.26

Flow Depth, H (cm) : 5.6

Pump No.1 Speed (Hz) : 41.1

Gate Configuration (Rods) : 3 (3/10)" , 1 square rod (tied)

Δh (mm) for Air/Water Manometer : 326

Water Discharge, Q (m³/s) : 0.0175

Depth-Averaged Velocity, V (m/s) : 0.516

Bursting Period, T_B (s) : 0.652

Probability of Entrainment, P_E : 8.484×10^{-5}

P_E/P_{Ecrit} : 0.84

Froude Number : 0.70

Densimetric Froude Number : 0.42

Particle Reynolds Number : 311

Dimensionless Critical Shear Stress : 0.0065

Comments : none

Table A.24 Frequency of particle displacements at threshold conditions for experiment G2 (teflon balls $H/D_{50} = 8$).

Time Period, Δt_i (minutes)	Fraction Displaced N_E/N_T	Fraction Displaced N_E/N_T (decimal)	Frequency of Displacement, f_i (1/s)
0-1	1/62	0.016129032	0.000268817
1-2	0/62	0	0
2-3	0/62	0	0
3-4	1/62	0.016129032	0.000268817
4-5	1/62	0.016129032	0.000268817
5-6	0/62	0	0
6-7	2/62	0.032258065	0.000537634
7-8	0/63	0	0
8-9	0/63	0	0
9-10	0/63	0	0
10-11	0/63	0	0
11-12	0/63	0	0
12-13	0/63	0	0
13-14	0/63	0	0
14-15	0/63	0	0
15-16	1/63	0.015873016	0.00026455
16-17	0/63	0	0
17-18	0/63	0	0
18-19	0/63	0	0
19-20	1/63	0.015873016	0.00026455

$$f_{avg} = 9.37 \times 10^{-5}$$

Date of Experiment : May 24, 1998

Slope, S (%) : 0.035

Flow Depth, H (cm) : 6.4

Pump No.1 Speed (Hz) : 32.3

Gate Configuration (Rods) : 4 (3/10)" , 2 (1/4) " , 1 square rod

Δh (mm) for Air/Water Manometer : 154.5

Water Discharge, Q (m³/s) : 0.0120

Depth-Averaged Velocity, V (m/s) : 0.311

Bursting Period, T_B (s) : 1.24

Probability of Entrainment, P_E : 1.158×10^{-4}

P_E/P_{Ecrit} : 1.14

Froude Number : 0.39

Densimetric Froude Number : 0.37

Particle Reynolds Number : 121

Dimensionless Critical Shear Stress : 0.00252

Comments : This test should start 1 minute after the "begin" signal in the video.

Table A.25 Frequency of particle displacements at threshold conditions for experiment G3 (glass balls $H/D_{50} = 8$).

Time Period, Δt_i (minutes)	Fraction Displaced N_E/N_T	Fraction Displaced N_E/N_T (decimal)	Frequency of Displacement, f_i (1/s)
0-1	0/69	0	0
1-2	1/69	0.014492754	0.000241546
2-3	1/69	0.014492754	0.000241546
3-4	0/69	0	0
4-5	1/69	0.014492754	0.000241546
5-6	1/69	0.014492754	0.000241546
6-7	0/69	0	0
7-8	0/69	0	0
8-9	0/69	0	0
9-10	1/69	0.014492754	0.000241546
10-11	0/69	0	0
11-12	2/69	0.028985507	0.000483092
12-13	0/69	0	0
13-14	1/69	0.014492754	0.000241546
14-15	0/69	0	0
15-16	1/69	0.014492754	0.000241546
16-17	0/69	0	0
17-18	0/69	0	0
18-19	0/69	0	0
19-20	0/69	0	0

$$f_{\text{avg}} = 1.09 \times 10^{-4}$$

Date of Experiment : May 31, 1998

Slope, S (%) : 0.115

Flow Depth, H (cm) : 6.4

Pump No.1 Speed (Hz) : 35.4

Gate Configuration (Rods) : 4 (3/10)" , 1 (1/4) " , 2 square rods

Δh (mm) for Air/Water Manometer : 210

Water Discharge, Q (m³/s) : 0.0140

Depth-Averaged Velocity, V (m/s) : 0.362

Bursting Period, T_B (s) : 1.06

Probability of Entrainment, P_E : 1.153×10^{-4}

P_E/P_{Ecrit} : 1.14

Froude Number : 0.46

Densimetric Froude Number : 0.36

Particle Reynolds Number : 218

Dimensionless Critical Shear Stress : 0.00579

Comments : This test should start 3 minutes after the "begin" signal in the video.

Table A.26 Frequency of particle displacements at threshold conditions for experiment G4 (ceramic balls $H/D_{50} = 8$).

Time Period, Δt_i (minutes)	Fraction Displaced N_E/N_T	Fraction Displaced N_E/N_T (decimal)	Frequency of Displacement, f_i (1/s)
0-1	3/61	0.049180328	0.000819672
1-2	0/61	0	0
2-3	0/61	0	0
3-4	1/61	0.016393443	0.000273224
4-5	0/61	0	0
5-6	0/61	0	0
6-7	0/61	0	0
7-8	0/61	0	0
8-9	0/61	0	0
9-10	0/61	0	0
10-11	1/61	0.016393443	0.000273224
11-12	0/61	0	0
12-13	1/61	0.016393443	0.000273224
13-14	2/61	0.032786885	0.000546448
14-15	0/61	0	0
15-16	1/61	0.016393443	0.000273224
16-17	1/61	0.016393443	0.000273224
17-18	0/61	0	0
18-19	0/61	0	0
19-20	0/61	0	0

$$f_{avg} = 1.37 \times 10^{-4}$$

Date of Experiment : May 22, 1998

Slope, S (%) : 0.22

Flow Depth, H (cm) : 6.4

Pump No.1 Speed (Hz) : 44.4

Gate Configuration (Rods) : 3 (3/10)" , 1 (1/4) " , 1 square rods

Δh (mm) for Air/Water Manometer : 405

Water Discharge, Q (m³/s) : 0.0195

Depth-Averaged Velocity, V (m/s) : 0.503

Bursting Period, T_B (s) : 0.764

Probability of Entrainment, P_E : 1.043×10^{-4}

P_E/P_{Ecrit} : 1.03

Froude Number : 0.64

Densimetric Froude Number : 0.38

Particle Reynolds Number : 302

Dimensionless Critical Shear Stress : 0.00629

Comments : none

Table A.27 Frequency of particle displacements at threshold conditions for experiment H3 (glass balls $H/D_{50} = 10$).

Time Period, Δt_i (minutes)	Fraction Displaced N_E/N_T	Fraction Displaced N_E/N_T (decimal)	Frequency of Displacement, f_i (1/s)
0-1	2/68	0.029411765	0.000490196
1-2	0/68	0	0
2-3	0/68	0	0
3-4	1/68	0.014705882	0.000245098
4-5	0/68	0	0
5-6	1/68	0.014705882	0.000245098
6-7	0/68	0	0
7-8	0/68	0	0
8-9	0/68	0	0
9-10	1/68	0.014705882	0.000245098
10-11	0/68	0	0
11-12	0/68	0	0
12-13	0/68	0	0
13-14	0/68	0	0
14-15	0/68	0	0
15-16	0/68	0	0
16-17	1/68	0.014705882	0.000245098
17-18	1/68	0.014705882	0.000245098
18-19	0/68	0	0
19-20	0/68	0	0

$$f_{avg} = 8.58 \times 10^{-5}$$

Date of Experiment : June 5, 1998

Slope, S (%) : 0.09

Flow Depth, H (cm) : 8.0

Pump No.1 Speed (Hz) : 41.4

Gate Configuration (Rods) : 5 (3/10)" , 2 (1/4) " , 1 square rod (tied)

Δh (mm) for Air/Water Manometer : 329

Water Discharge, Q (m³/s) : 0.0176

Depth-Averaged Velocity, V (m/s) : 0.363

Bursting Period, T_B (s) : 1.32

Probability of Entrainment, P_E : 1.135×10^{-4}

P_E/P_{Ecrit} : 1.12

Froude Number : 0.41

Densimetric Froude Number : 0.33

Particle Reynolds Number : 211

Dimensionless Critical Shear Stress : 0.00566

Comments : This test should start 3 minutes after the "begin" signal in the video.

Table A.28 Frequency of particle displacements at threshold conditions for experiment H4 (ceramic balls $H/D_{50} = 10$).

Time Period, Δt_i (minutes)	Fraction Displaced N_E/N_T	Fraction Displaced N_E/N_T (decimal)	Frequency of Displacement, f_i (1/s)
0-1	1/65	0.015384615	0.00025641
1-2	0/65	0	0
2-3	1/65	0.015384615	0.00025641
3-4	0/65	0	0
4-5	0/65	0	0
5-6	0/65	0	0
6-7	0/65	0	0
7-8	2/65	0.030769231	0.000512821
8-9	1/64	0.015625	0.000260417
9-10	0/64	0	0
10-11	0/64	0	0
11-12	1/64	0.015625	0.000260417
12-13	0/64	0	0
13-14	0/64	0	0
14-15	0/64	0	0
15-16	0/64	0	0
16-17	0/64	0	0
17-18	1/64	0.015625	0.000260417
18-19	0/64	0	0
19-20	1/64	0.015625	0.000260417

$$f_{avg} = 1.03 \times 10^{-4}$$

Date of Experiment : June 9, 1998
Slope, S (%) : 0.17
Flow Depth, H (cm) : 8.0
Pump No.1 Speed (Hz) : 54
Gate Configuration (Rods) : 4 (3/10)" , 1 (1/4) "
 Δh (mm) for Air/Water Manometer : 632
Water Discharge, Q (m³/s) : 0.0243
Depth-Averaged Velocity, V (m/s) : 0.503
Bursting Period, T_B (s) : 0.955
Probability of Entrainment, P_E : 9.871×10^{-5}
P_E/P_{Ecrit} : 0.97
Froude Number : 0.57
Densimetric Froude Number : 0.34
Particle Reynolds Number : 291
Dimensionless Critical Shear Stress : 0.00607
Comments : none

Table A.29 Frequency of particle displacements at threshold conditions for experiment I3 (glass balls $H/D_{50} = 12$).

Time Period, Δt_i (minutes)	Fraction Displaced N_E/N_T	Fraction Displaced N_E/N_T (decimal)	Frequency of Displacement, f_i (1/s)
0-1	0/73	0	0
1-2	2/73	0.02739726	0.000456621
2-3	0/73	0	0
3-4	1/73	0.01369863	0.000228311
4-5	0/73	0	0
5-6	1/73	0.01369863	0.000228311
6-7	1/73	0.01369863	0.000228311
7-8	0/73	0	0
8-9	0/73	0	0
9-10	0/73	0	0
10-11	0/73	0	0
11-12	0/73	0	0
12-13	0/73	0	0
13-14	0/73	0	0
14-15	0/73	0	0
15-16	0/73	0	0
16-17	0/73	0	0
17-18	0/73	0	0
18-19	0/73	0	0
19-20	1/73	0.01369863	0.000228311

$$f_{avg} = 6.85 \times 10^{-5}$$

Date of Experiment : June 14, 1998

Slope, S (%) : 0.075

Flow Depth, H (cm) : 9.6

Pump No.1 Speed (Hz) : 45.1

Gate Configuration (Rods) : 5 (3/10)" , 4 (1/4) " , 1 square rod

Δh (mm) for Air/Water Manometer : 443

Water Discharge, Q (m³/s) : 0.0204

Depth-Averaged Velocity, V (m/s) : 0.351

Bursting Period, T_B (s) : 1.64

Probability of Entrainment, P_E : 1.125×10^{-4}

P_E/P_{Ecrit} : 1.11

Froude Number : 0.36

Densimetric Froude Number : 0.29

Particle Reynolds Number : 207

Dimensionless Critical Shear Stress : 0.00566

Comments : none

Table A.30 Frequency of particle displacements at threshold conditions for experiment D3T_B (glass balls $H/D_{50} = 5$ w/o considering the bursting period).

Time Period, Δt_i (minutes)	Fraction Displaced N_E/N_T	Fraction Displaced N_E/N_T (decimal)	Frequency of Displacement, f_i (1/s)
0-1	2/64	0.03125	0.000520833
1-2	1/64	0.015625	0.000260417
2-3	1/64	0.015625	0.000260417
3-4	2/64	0.03125	0.000520833
4-5	1/65	0.015384615	0.00025641
5-6	2/65	0.030769231	0.000512821
6-7	4/65	0.061538462	0.001025641
7-8	2/65	0.030769231	0.000512821
8-9	1/65	0.015384615	0.00025641
9-10	1/65	0.015384615	0.00025641
10-11	0/65	0	0
11-12	1/65	0.015384615	0.00025641
12-13	1/65	0.015384615	0.00025641
13-14	0/65	0	0
14-15	1/65	0.015384615	0.00025641
15-16	0/64	0	0
16-17	0/64	0	0
17-18	0/64	0	0
18-19	1/65	0.015384615	0.00025641
19-20	0/64	0	0

$$f_{avg} = 2.70 \times 10^{-4}$$

Date of Experiment : June 21, 1998

Slope, S (%) : 0.235

Flow Depth, H (cm) : 4.0

Pump No.1 Speed (Hz) : 27.8

Gate Configuration (Rods) : 3 (3/10)" , 1 square rod (tied)

Δh (mm) for Air/Water Manometer : 88

Water Discharge, Q (m³/s) : 0.00908

Depth-Averaged Velocity, V (m/s) : 0.375

Bursting Period, T_B (s) : 0.640

Probability of Entrainment, P_E : 1.730×10^{-4}

P_E/P_{Ecrit} : 1.71

f_{avg}/f_{avg_crit} : 0.93

Froude Number : 0.60

Densimetric Froude Number : 0.48

Particle Reynolds Number : 255

Dimensionless Critical Shear Stress : 0.00739

Comments : none

Table A.31 Frequency of particle displacements at threshold conditions for experiment E3T_B (glass balls H/D₅₀ = 6 w/o considering the bursting period).

Time Period, Δt_i (minutes)	Fraction Displaced N_E/N_T	Fraction Displaced N_E/N_T (decimal)	Frequency of Displacement, f_i (1/s)
0-1	2/72	0.027777778	0.000462963
1-2	2/72	0.027777778	0.000462963
2-3	2/72	0.027777778	0.000462963
3-4	3/72	0.041666667	0.000694444
4-5	1/71	0.014084507	0.000234742
5-6	1/71	0.014084507	0.000234742
6-7	4/71	0.056338028	0.000938967
7-8	0/71	0	0
8-9	1/71	0.014084507	0.000234742
9-10	2/71	0.028169014	0.000469484
10-11	0/71	0	0
11-12	2/72	0.027777778	0.000462963
12-13	2/72	0.027777778	0.000462963
13-14	0/71	0	0
14-15	1/71	0.014084507	0.000234742
15-16	1/71	0.014084507	0.000234742
16-17	2/70	0.028571429	0.00047619
17-18	0/70	0	0
18-19	2/70	0.028571429	0.00047619
19-20	1/70	0.014285714	0.000238095

$$f_{avg} = 3.39 \times 10^{-4}$$

Date of Experiment : October 19, 1998

Slope, S (%) : 0.18

Flow Depth, H (cm) : 4.8

Pump No.1 Speed (Hz) : 31.5

Gate Configuration (Rods) : 3 (3/10)" , 1 (1/4) " , 1 square rod

Δh (mm) for Air/Water Manometer : 130.5

Water Discharge, Q (m³/s) : 0.0111

Depth-Averaged Velocity, V (m/s) : 0.381

Bursting Period, T_B (s) : 0.757

Probability of Entrainment, P_E : 2.566×10^{-4}

P_E/P_{Ecrit} : 2.53

f_{avg}/f_{avg_crit} : 1.17

Froude Number : 0.55

Densimetric Froude Number : 0.44

Particle Reynolds Number : 261

Dimensionless Critical Shear Stress : 0.00679

Comments : none

Table A.32 Frequency of particle displacements at threshold conditions for experiment B2M1 (teflon balls $H/D_{50} = 3$ with M1 profile).

Time Period, Δt_i (minutes)	Fraction Displaced N_E/N_T	Fraction Displaced N_E/N_T (decimal)	Frequency of Displacement, f_i (1/s)
0-1	0/58	0	0
1-2	2/58	0.034482759	0.000574713
2-3	2/58	0.034482759	0.000574713
3-4	1/58	0.017241379	0.000287356
4-5	2/58	0.034482759	0.000574713
5-6	3/58	0.051724138	0.000862069
6-7	0/58	0	0
7-8	0/58	0	0
8-9	1/58	0.017241379	0.000287356
9-10	1/57	0.01754386	0.000292398
10-11	0/57	0	0
11-12	2/57	0.035087719	0.000584795
12-13	0/57	0	0
13-14	0/57	0	0
14-15	1/57	0.01754386	0.000292398
15-16	0/56	0	0
16-17	0/56	0	0
17-18	1/56	0.017857143	0.000297619
18-19	0/56	0	0
19-20	0/56	0	0

$$f_{avg} = 2.31 \times 10^{-4}$$

Date of Experiment : August 8, 1997

Slope, S (%) : 0.4

Flow Depth, H (cm) at Station H_4 : 2.35

Flow Depth, H (cm) at Station H_5 : 2.4

Flow Depth, H (cm) at Station H_6 : 2.4

Pump No.1 Speed (Hz) : 17.5

Gate Configuration (Rods) : 3 (3/10)''

Δh (mm) for Air/Water Manometer : 21.5

Water Discharge, Q (m^3/s) : 0.00449

Depth-Averaged Velocity, V (m/s) : 0.309

Bursting Period, T_B (s) : 0.466

Probability of Entrainment, P_E : 1.080×10^{-4}

P_E/P_{Ecrit} : 1.06

Froude Number : 0.64

Densimetric Froude Number : 0.60

Particle Reynolds Number : 264

Dimensionless Critical Shear Stress : 0.0108

Comments : none

Table A.33 Frequency of particle displacements at threshold conditions for experiment B3M1 (glass balls $H/D_{50} = 3$ with M1 profile).

Time Period, Δt_i (minutes)	Fraction Displaced N_E/N_T	Fraction Displaced N_E/N_T (decimal)	Frequency of Displacement, f_i (1/s)
0-1	2/63	0.031746032	0.000529101
1-2	3/64	0.046875	0.00078125
2-3	1/66	0.015151515	0.000252525
3-4	3/67	0.044776119	0.000746269
4-5	2/67	0.029850746	0.000497512
5-6	1/67	0.014925373	0.000248756
6-7	0/68	0	0
7-8	0/69	0	0
8-9	1/69	0.014492754	0.000241546
9-10	0/69	0	0
10-11	1/69	0.014492754	0.000241546
11-12	1/70	0.014285714	0.000238095
12-13	0/70	0	0
13-14	3/70	0.042857143	0.000714286
14-15	1/70	0.014285714	0.000238095
15-16	1/70	0.014285714	0.000238095
16-17	0/70	0	0
17-18	0/71	0	0
18-19	1/71	0.014084507	0.000234742
19-20	0/71	0	0

$$f_{avg} = 2.60 \times 10^{-4}$$

Date of Experiment : August 4, 1997

Slope, S (%) : 0.6

Flow Depth, H (cm) at Station H_4 : 2.3

Flow Depth, H (cm) at Station H_5 : 2.4

Flow Depth, H (cm) at Station H_6 : 2.4

Pump No.1 Speed (Hz) : 19.1

Gate Configuration (Rods) : 3 (3/10)"

Δh (mm) for Air/Water Manometer : 29.5

Water Discharge, Q (m^3/s) : 0.00526

Depth-Averaged Velocity, V (m/s) : 0.362

Bursting Period, T_B (s) : 0.398

Probability of Entrainment, P_E : 1.03×10^{-4}

P_E/P_{Ecrit} : 1.02

Froude Number : 0.75

Densimetric Froude Number : 0.59

Particle Reynolds Number : 324

Dimensionless Critical Shear Stress : 0.0113

Comments : none

Table A.34 Frequency of particle displacements at threshold conditions for experiment B4M1 (ceramic balls $H/D_{50} = 3$ with M1 profile).

Time Period, Δt_i (minutes)	Fraction Displaced N_E/N_T	Fraction Displaced N_E/N_T (decimal)	Frequency of Displacement, f_i (1/s)
0-1	6/68	0.088235294	0.001470588
1-2	1/68	0.014705882	0.000245098
2-3	3/69	0.043478261	0.000724638
3-4	1/69	0.014492754	0.000241546
4-5	1/72	0.013888889	0.000231481
5-6	1/73	0.01369863	0.000228311
6-7	0/73	0	0
7-8	0/73	0	0
8-9	0/73	0	0
9-10	0/73	0	0
10-11	1/73	0.01369863	0.000228311
11-12	1/73	0.01369863	0.000228311
12-13	1/73	0.01369863	0.000228311
13-14	2/73	0.02739726	0.000456621
14-15	4/75	0.053333333	0.000888889
15-16	0/75	0	0
16-17	1/75	0.013333333	0.000222222
17-18	1/74	0.013513514	0.000225225
18-19	0/73	0	0
19-20	1/73	0.01369863	0.000228311

$$f_{avg} = 2.92 \times 10^{-4}$$

Date of Experiment : August 2, 1997

Slope, S (%) : 1.1

Flow Depth, H (cm) at Station H_4 : 2.3

Flow Depth, H (cm) at Station H_5 : 2.4

Flow Depth, H (cm) at Station H_6 : 2.4

Pump No.1 Speed (Hz) : 23.0

Gate Configuration (Rods) : 3 (3/10)''

Δh (mm) for Air/Water Manometer : 55

Water Discharge, Q (m^3/s) : 0.00718

Depth-Averaged Velocity, V (m/s) : 0.494

Bursting Period, T_B (s) : 0.291

Probability of Entrainment, P_E : 8.519×10^{-5}

P_E/P_{Ecrit} : 0.84

Froude Number : 1.02

Densimetric Froude Number : 0.61

Particle Reynolds Number : 438

Dimensionless Critical Shear Stress : 0.0118

Comments : none

Appendix 2.

This appendix contains several tables and plots. The tables summarize the von Karman constant, integral constant, correlation coefficient and other information for all the experiments in which LDV measurements were taken. Table A.35 is for the case where the velocity profile corresponding to the free surface flow is split into two regions. Table A.36 is for the case where the velocity profile corresponding to the free surface flow is represented by a single equation and the datum is 1mm (0.125k) below the top of the balls in the bed. Tables A.37 and A.38 are similar, but for the pressurized flow. Figures A.1-14a show the velocity profile in arithmetic coordinates for each experiment. Figures A.1-14b show the logarithmic velocity profile split into two regions for each experiment. The datum is at the top of the ball in the bed. Figures A.1-14c show the logarithmic velocity profile for the entire flow depth represented by one equation. The datum is at the top of the balls in the bed. Finally, Figures A.1-14d show the logarithmic velocity profile for the entire flow depth represented by one equation, but the datum is 1mm (0.125k) below the top of the balls in the bed.

Table A.35 Summary of logarithmic velocity profiles for free surface flow: Split into 2 regions (The datum is at the top of the balls in the channel bed).

H/D ₅₀	A (Near-wall region)	B (Near-wall region)	R ²	A (Upper Region)	B (Upper Region)	R ²	z/k _s of slope transition
4	1.59	9.61	0.9786	3.15	9.99	0.9966	0.7
4 (Fr>1)	1.37	8.07	0.9964	2.88	8.51	0.9974	0.7
5	1.39	9.52	0.9901	3.08	10.06	0.9968	0.7
6	1.65	8.81	0.9869	2.89	8.95	0.9971	0.8
6 (Fr>1)	1.42	8.18	0.9946	2.80	8.51	0.9974	0.8
7	1.57	9.19	0.9953	2.98	9.52	0.9978	0.8
8	1.46	9.02	0.9881	2.99	9.30	0.9976	0.8
10	1.48	8.66	0.9785	3.15	8.67	0.9975	0.8
12	1.41	8.76	0.9862	2.81	8.97	0.9954	0.7
Average:	1.48	8.87	-	2.97	9.16	-	-
Std.Dev:	0.0988	0.533	-	0.135	0.593	-	-

Table A.36 Summary of logarithmic velocity profiles for free surface flow: Single region (The datum is 1mm below the top of the balls in the channel bed).

H/D ₅₀	Date of Experiment	Slope (%)	Froude Number	A	von Karman κ	B	R ²
4	9/20/98	0.28	0.62	2.99	0.334	9.90	0.9883
4 (Fr>1)	7/14/98	1	1.17	2.72	0.368	8.46	0.9886
5	9/19/98	0.21	0.56	2.90	0.345	10.08	0.9894
6	7/17/98	0.165	0.50	2.88	0.347	8.84	0.9948
6 (Fr>1)	7/14/98	0.85	1.11	2.74	0.365	8.46	0.9927
7	7/15/98	0.135	0.47	2.94	0.340	9.44	0.9947
8	8/10/98	0.115	0.46	2.92	0.342	9.30	0.993
10	6/23/98	0.09	0.41	2.98	0.336	8.85	0.9896
12	6/22/98	0.075	0.36	2.77	0.361	8.96	0.993
Average:	-	-	-	2.87	0.349	9.14	-
Std.Dev:	-	-	-	0.103	0.0128	0.582	-

Table A.37 Summary of logarithmic velocity profiles for pressurized flow: Split into 2 regions (The datum is at the top of the balls in the channel bed).

H/D ₅₀	A (Near-wall region)	B (Near-wall region)	R ²	A (Upper Region)	B (Upper Region)	R ²	z/k _s of slope transition
3	1.45	9.44	0.9787	3.09	10.51	0.9959	0.5
4.5	1.68	9.52	0.9851	3.84	9.74	0.9961	0.8
5.5	1.32	8.91	0.969	3.49	9.25	0.9949	0.8
6.5	1.34	9.03	0.9718	3.30	9.39	0.9982	0.8
8.5	1.36	9.23	0.9853	3.35	9.44	0.9955	0.8
Average:	1.43	9.23	-	3.41	9.67	-	-
Std.Dev:	0.148	0.260	-	0.278	0.505	-	-

Table A.38 Summary of logarithmic velocity profiles for pressurized flow: Single region (The datum is 1mm below the top of the balls in the channel bed).

H/D ₅₀	Date of Experiment	Slope (%)	A	von Karman κ	B	R ²
3	9/19/98	0.21	3.07	0.326	10.22	0.9895
4.5	9/14/98	0.21	3.31	0.302	9.89	0.9784
5.5	9/13/98	0.21	2.96	0.338	9.54	0.976
6.5	9/9/98	0.21	2.87	0.348	9.60	0.9808
8.5	9/8/98	0.21	2.99	0.334	9.74	0.9823
Average:	-	-	3.04	0.330	9.80	-
Std.Dev:	-	-	0.167	0.0173	0.272	-

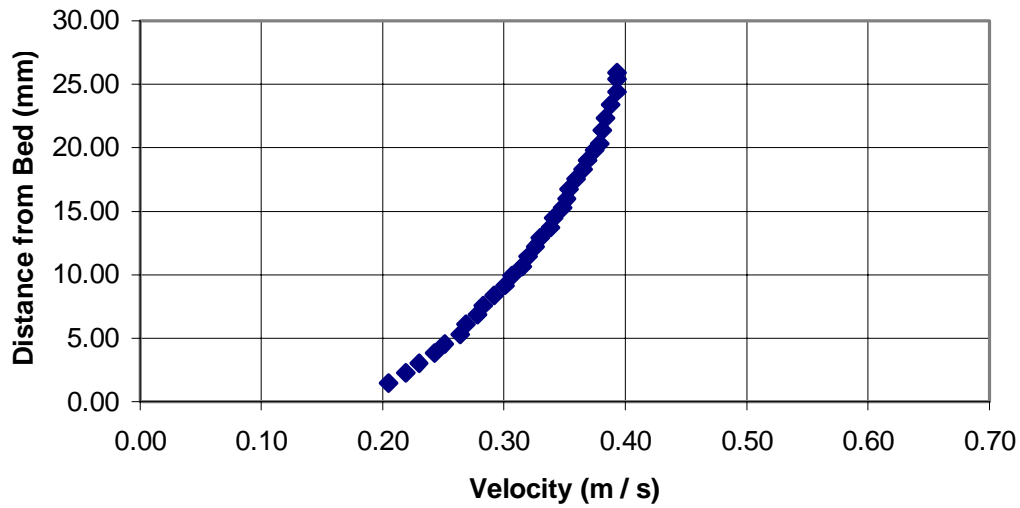


Figure A.1a Velocity profile for experiment C3 ($H/D_{50} = 4$ and $S = 0.28\%$). The datum is at the top of the balls in the channel bed.

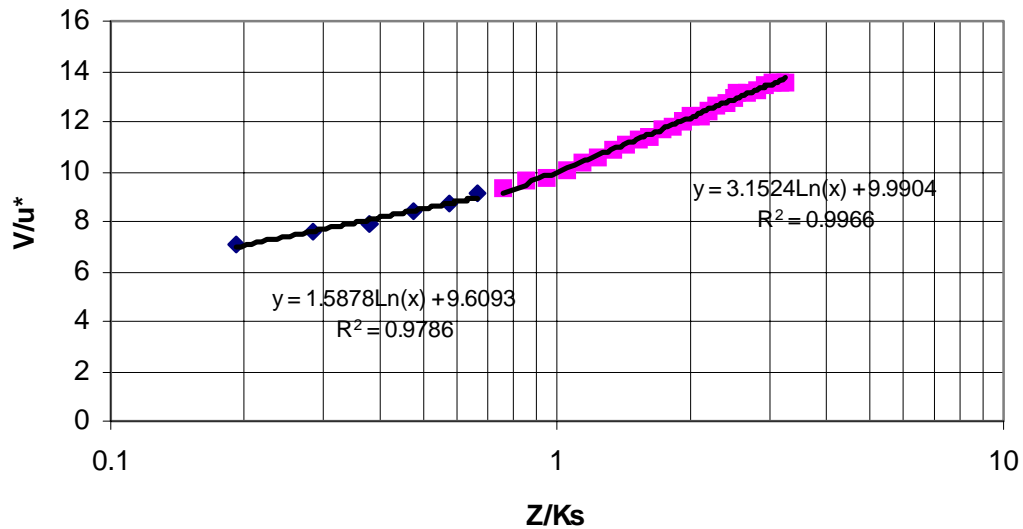


Figure A.1b Logarithmic velocity profile for experiment C3 ($H/D_{50} = 4$ and $S = 0.28\%$) split into two regions. The datum is at the top of the balls in the channel bed.

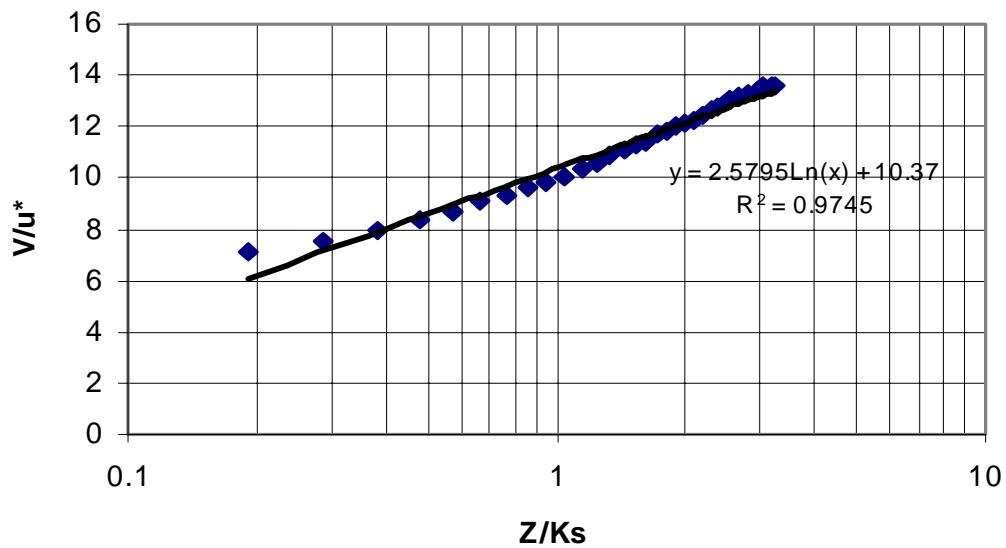


Figure A.1c Logarithmic velocity profile for experiment C3 ($H/D_{50} = 4$ and $S = 0.28\%$) : single region. The datum is at the top of the balls in the channel bed.

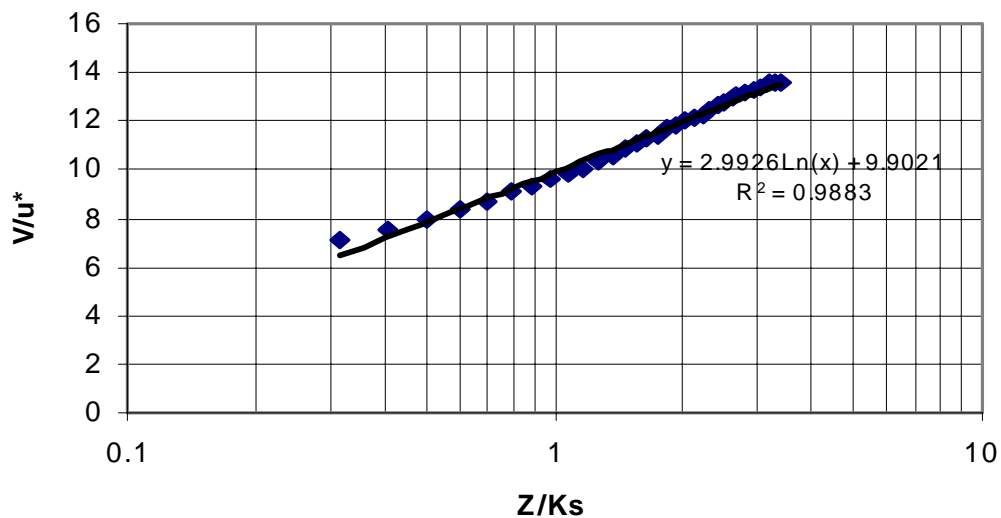


Figure A.1d Logarithmic velocity profile for experiment C3 ($H/D_{50} = 4$ and $S = 0.28\%$): single region. The datum is 1 mm below the top of the balls in the bed.

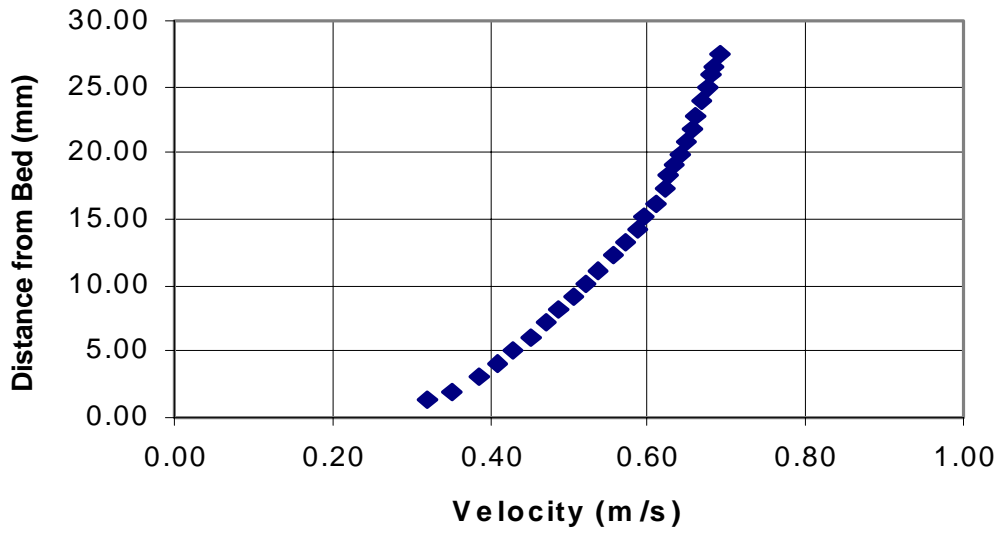


Figure A.2a Velocity profile for $H/D_{50} = 4$ (Supercritical flow, $S = 1\%$). The datum is at the top of the balls in the channel bed.

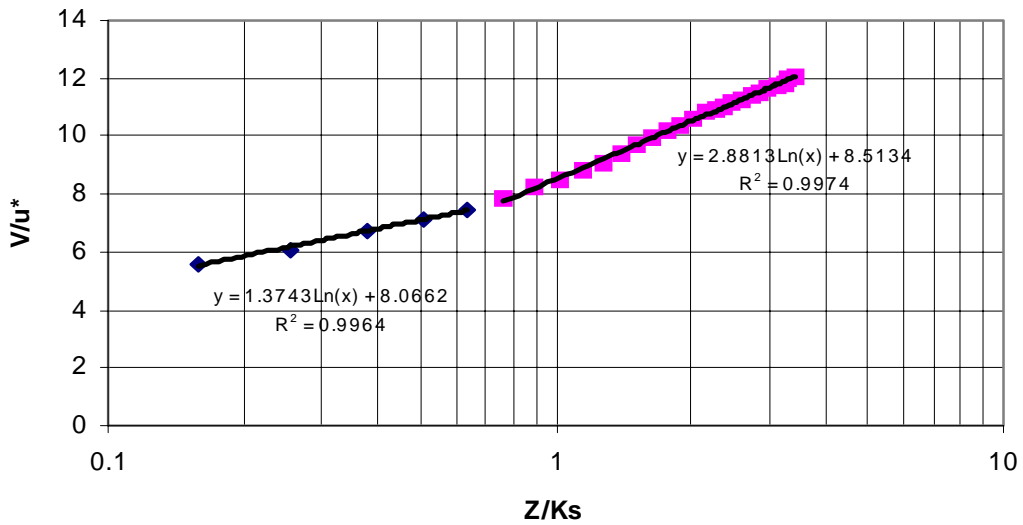


Figure A.2b Logarithmic velocity profile for $H/D_{50} = 4$ (Supercritical flow, $S = 1\%$) split into two regions. The datum is at the top of the balls in the channel bed.

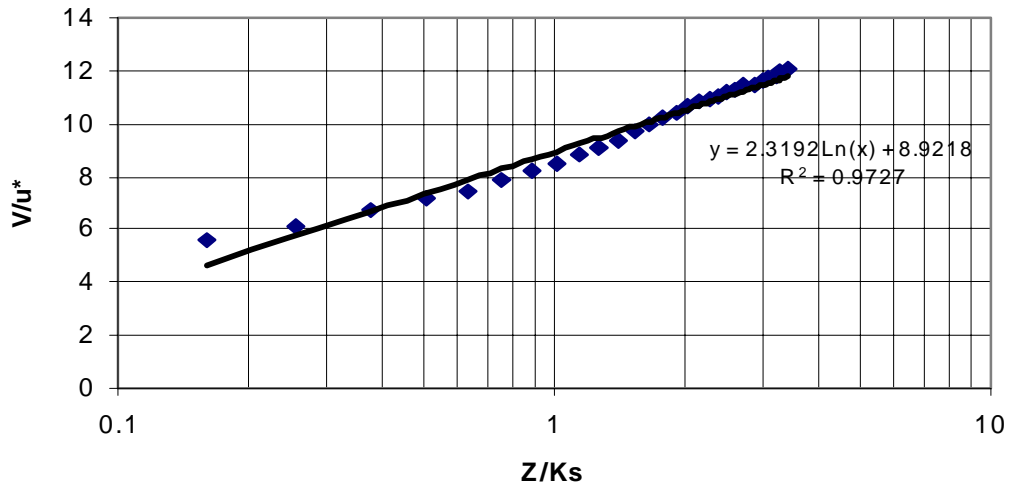


Figure A.2c Logarithmic velocity profile for $H/D_{50} = 4$ (Supercritical flow, $S = 1\%$): single region. The datum is at the top of the balls in the channel bed.

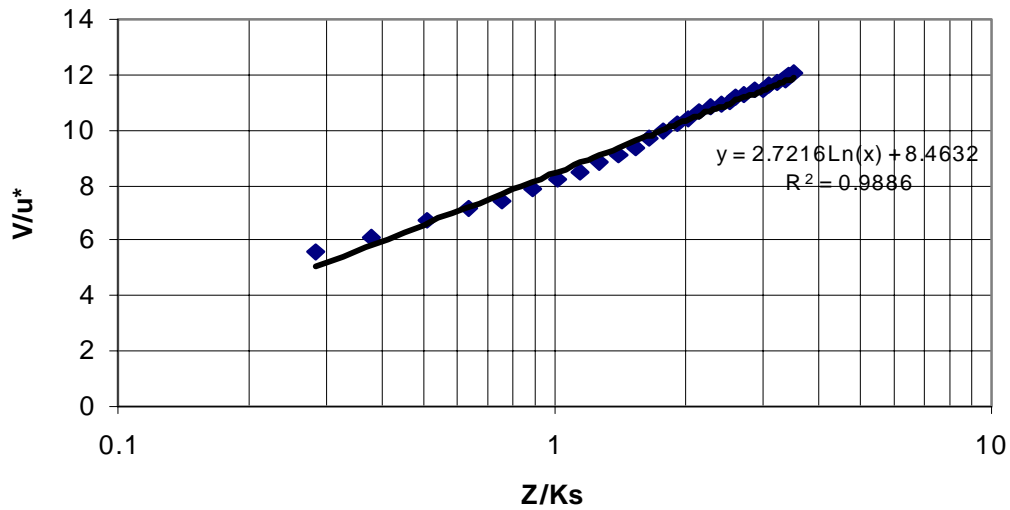


Figure A.2d Logarithmic velocity profile for experiment $H/D_{50} = 4$ (Supercritical flow, $S = 1\%$): single region. The datum is 1mm below the top of the balls in the bed.

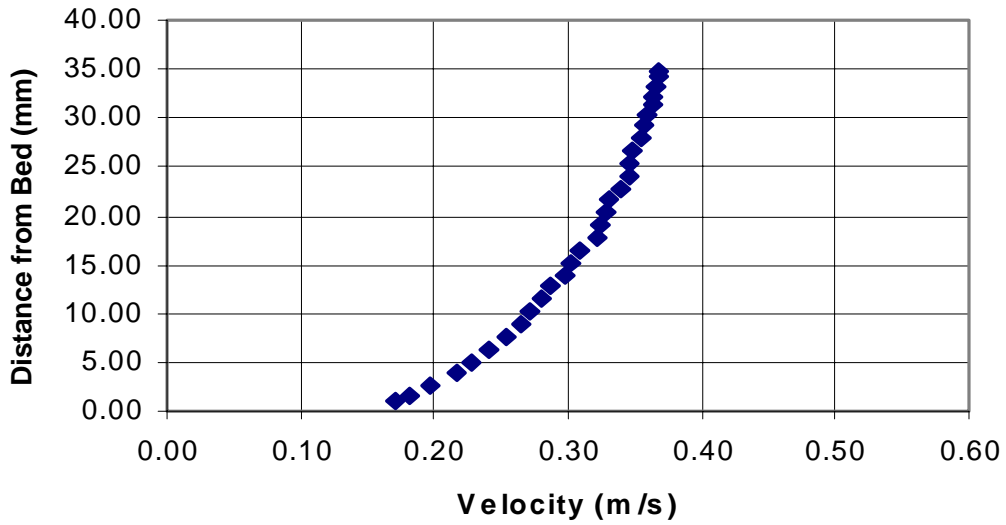


Figure A.3a Velocity profile for experiment D3 ($H/D_{50} = 5$ and $S = 0.21\%$). The datum is at the top of the balls in the channel bed.

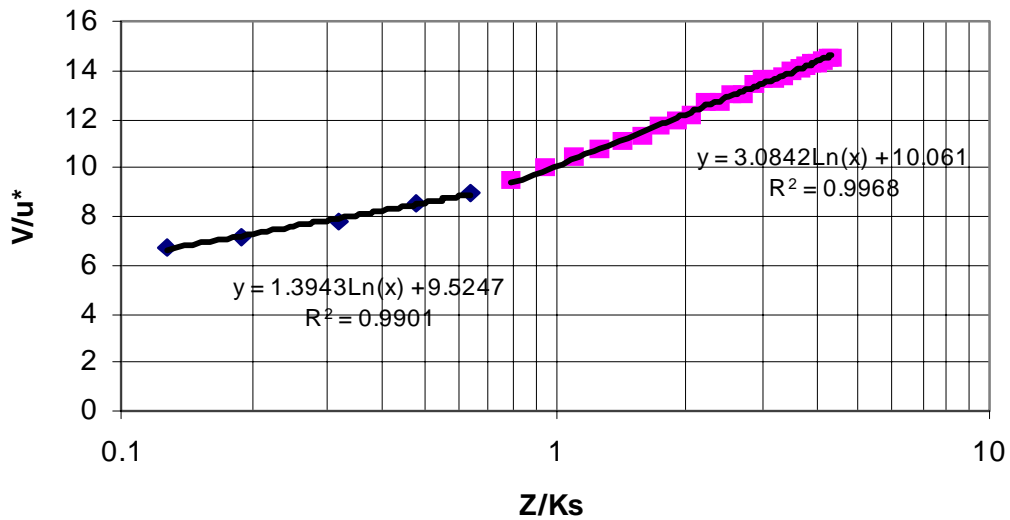


Figure A.3b Logarithmic velocity profile for experiment D3 ($H/D_{50} = 5$ and $S = 0.21\%$) split into two regions. The datum is at the top of the balls in the channel bed.

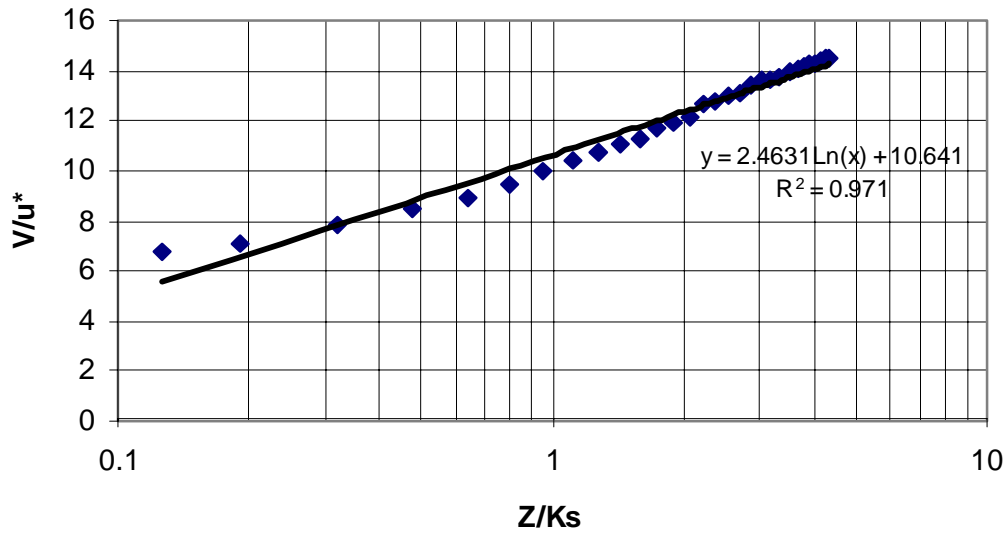


Figure A.3c Logarithmic velocity profile for experiment D3 ($H/D_{50} = 5$ and $S = 0.21\%$): single region. The datum is at the top of the balls in the channel bed.

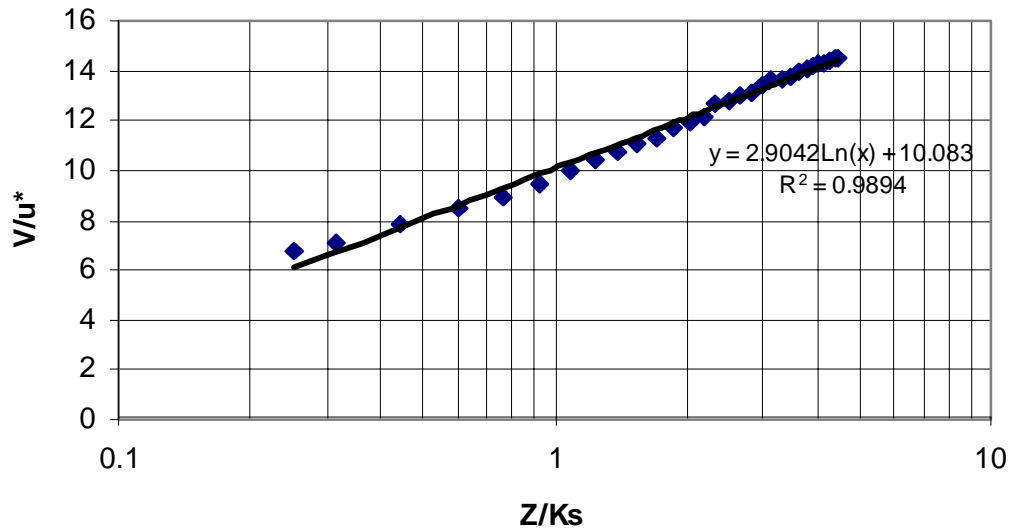


Figure A.3d Logarithmic velocity profile for experiment D3 ($H/D_{50} = 5$ and $S = 0.21\%$): single region. The datum is 1 mm below the top of the balls in the bed.

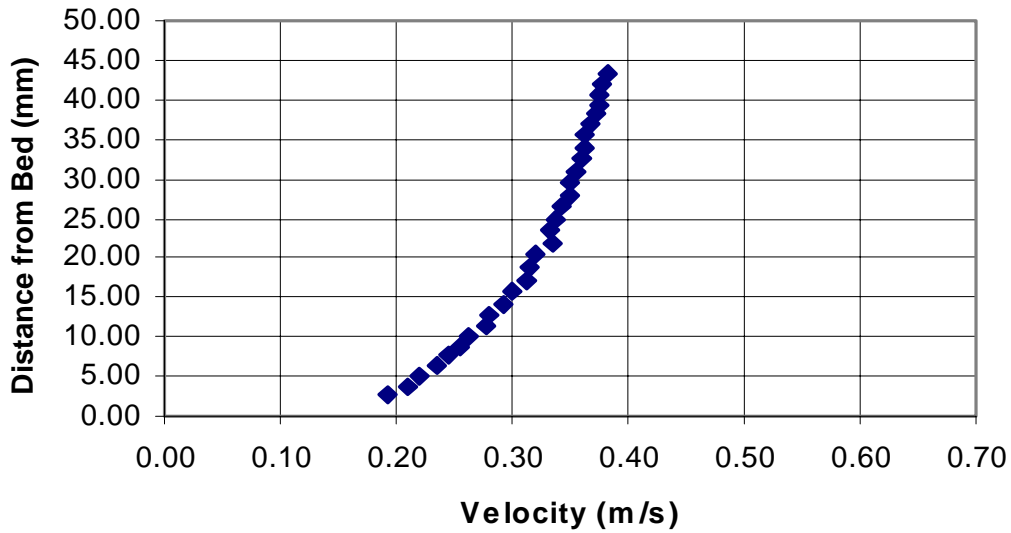


Figure A.4a Velocity profile for experiment E3 ($H/D_{50} = 6$ and $S = 0.165\%$). The datum is at the top of the balls in the channel bed.

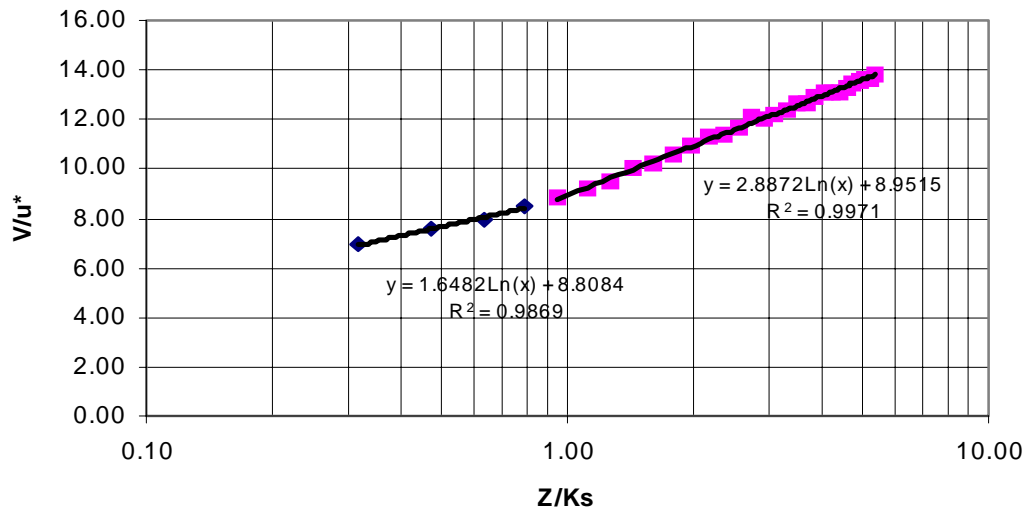


Figure A.4b Logarithmic velocity profile for experiment E3 ($H/D_{50} = 6$ and $S = 0.165\%$) split into two regions. The datum is at the top of the balls in the bed.

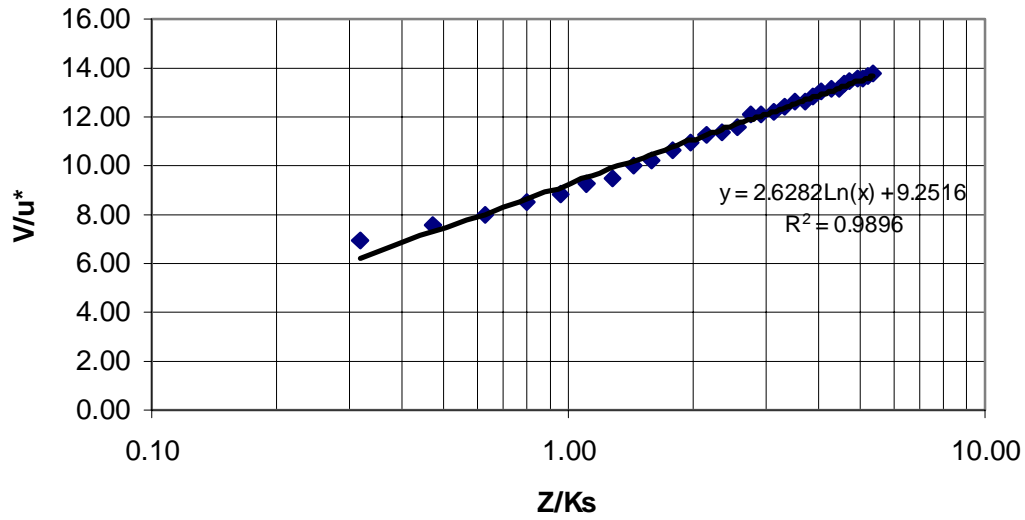


Figure A.4c Logarithmic velocity profile for experiment E3 ($H/D_{50} = 6$ and $S = 0.165\%$): single region. The datum is at the top of the balls in the channel bed.

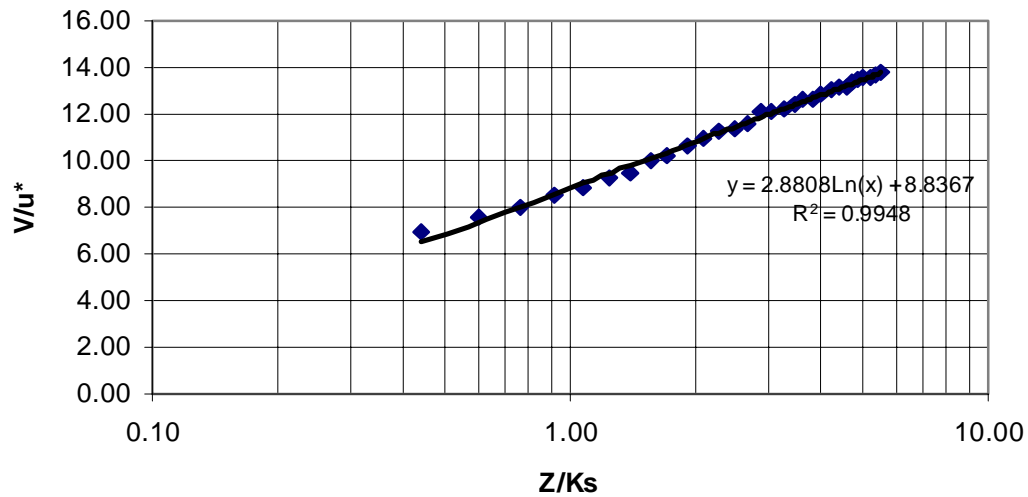


Figure A.4d Logarithmic velocity profile for experiment E3 ($H/D_{50} = 6$ and $S = 0.165\%$): single region. The datum is 1 mm below the top of the balls in the bed.

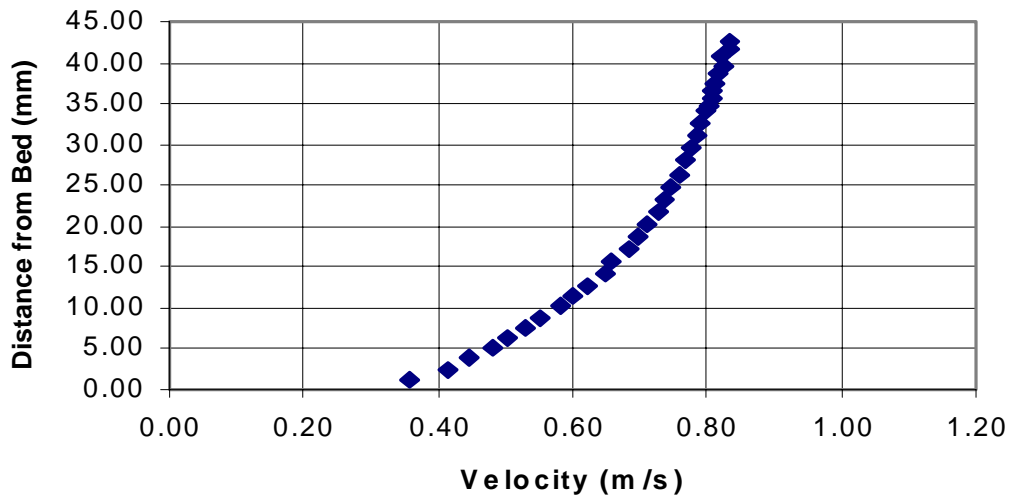


Figure A.5a Velocity profile for $H/D_{50} = 6$ (Supercritical flow, $S = 0.85\%$). The datum is at the top of the balls in the channel bed.

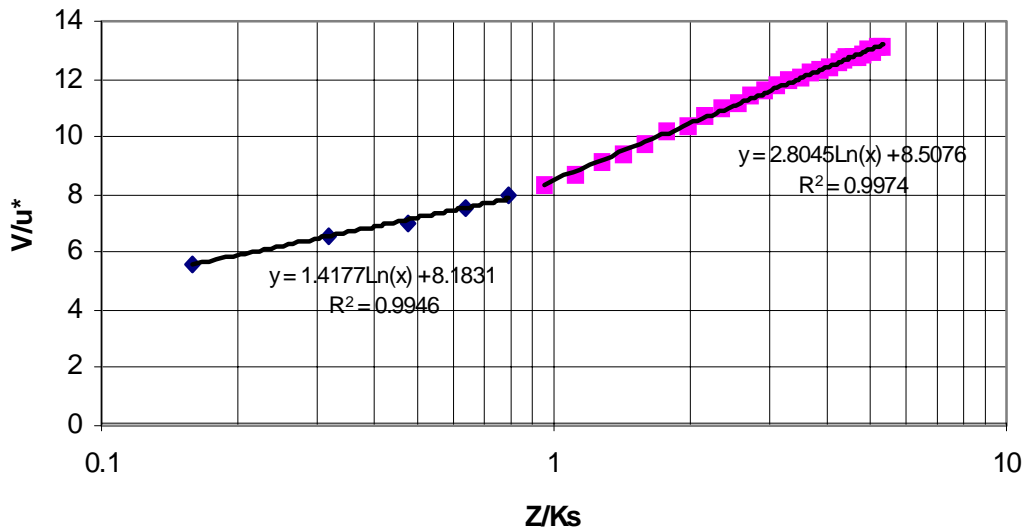


Figure A.5b Logarithmic velocity profile for $H/D_{50} = 6$ (Supercritical flow, $S = 0.85\%$) split into two regions. The datum is at the top of the balls in the channel bed.

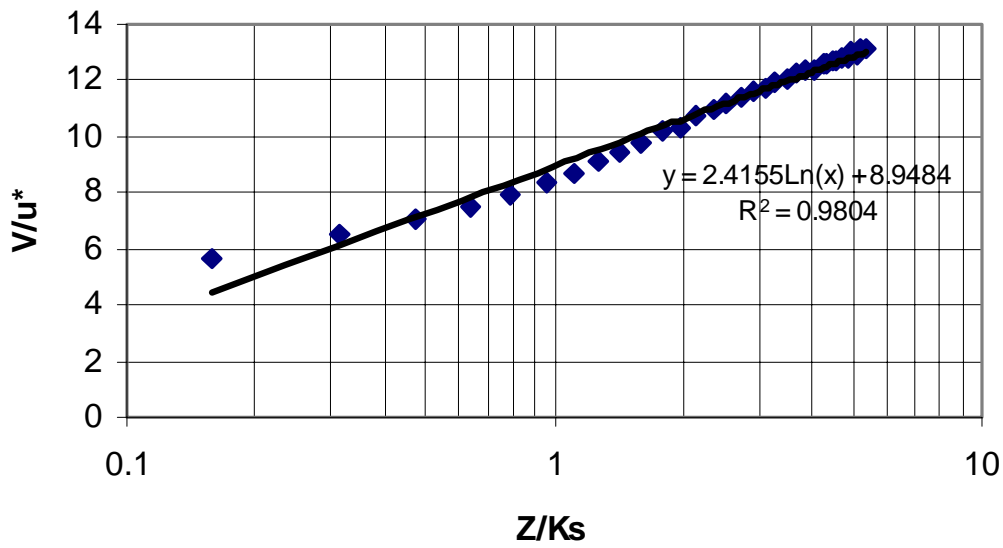


Figure A.5c Logarithmic velocity profile for experiment $H/D_{50} = 6$ (Supercritical flow, $S = 0.85\%$): single region. The datum is at the top of the balls in the bed.

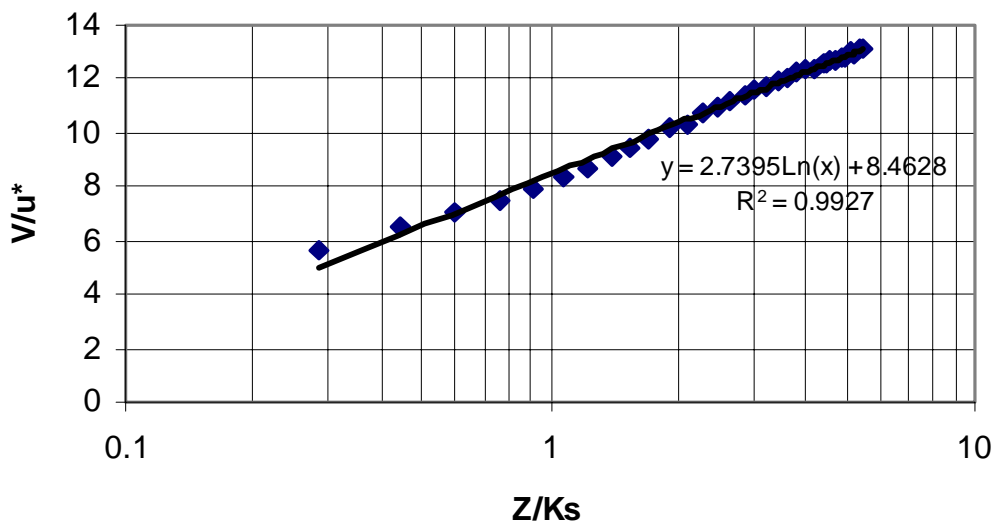


Figure A.5d Logarithmic velocity profile for experiment $H/D_{50} = 6$ (Supercritical flow, $S = 0.85\%$): single region. The datum is 1mm below the top of the balls in the channel bed.

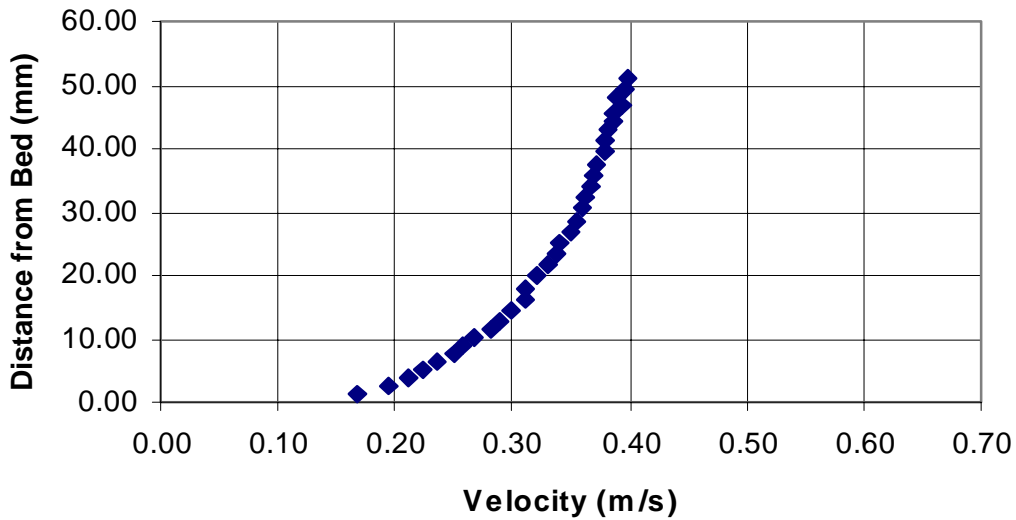


Figure A.6a Velocity profile for experiment F3 ($H/D_{50} = 7$ and $S = 0.135\%$). The datum is at the top of the balls in the channel bed.

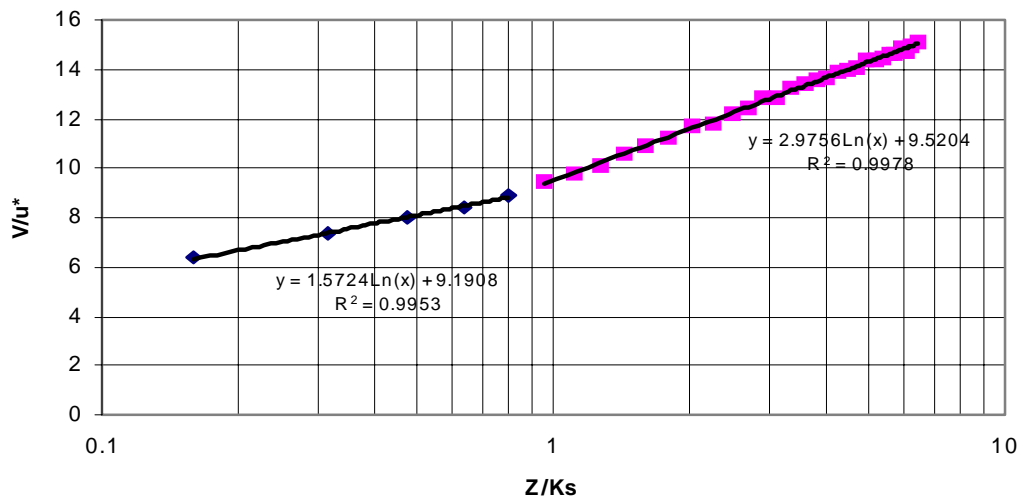


Figure A.6b Logarithmic velocity profile for experiment F3 ($H/D_{50} = 7$ and $S = 0.135\%$) split into two regions. The datum is at the top of the balls in the channel bed.

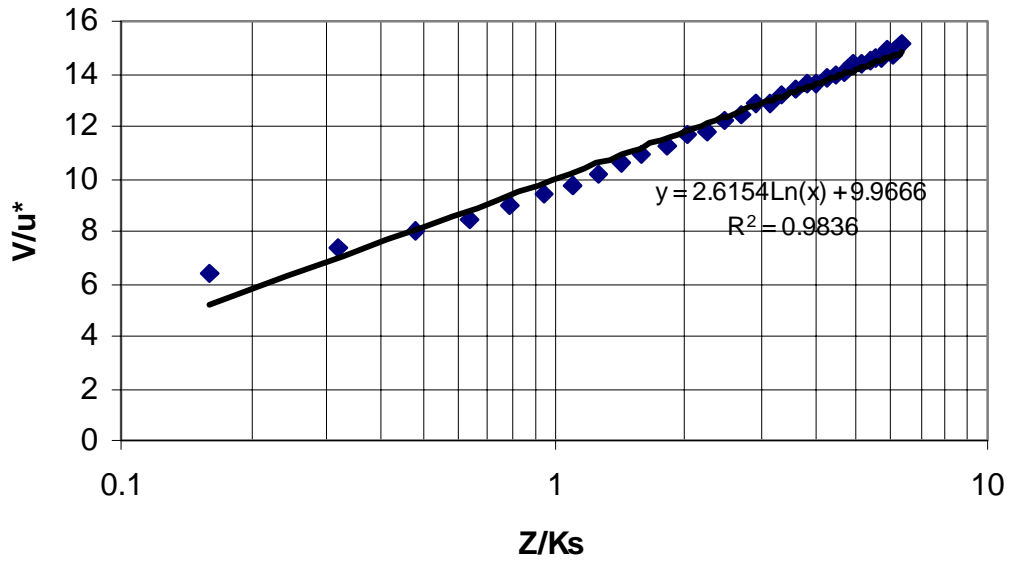


Figure A.6c Logarithmic velocity profile for experiment F3 ($H/D_{50} = 7$ and $S = 0.135\%$): single region. The datum is at the top of the balls in the channel bed.

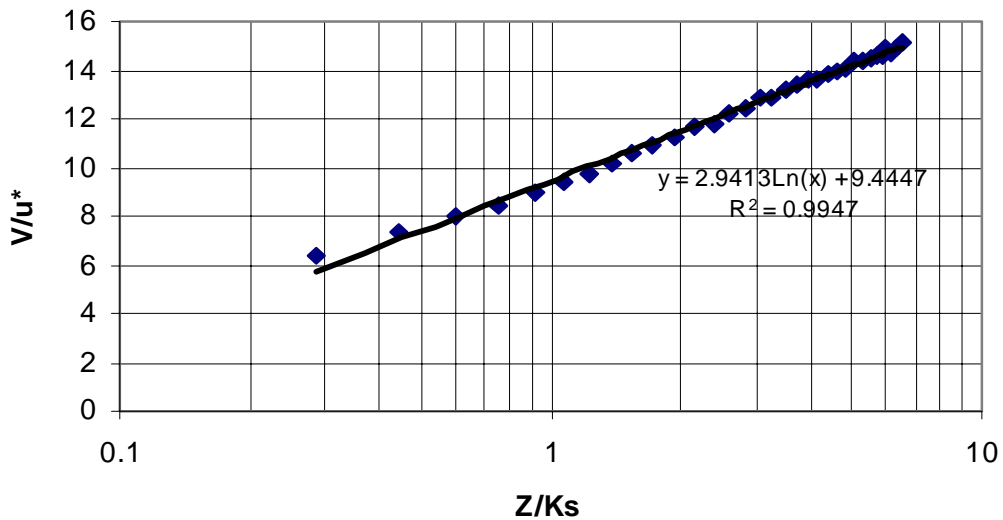


Figure A.6d Logarithmic velocity profile for experiment F3 ($H/D_{50} = 7$ and $S = 0.135\%$): single region. The datum is 1 mm below the top of the balls in the bed.

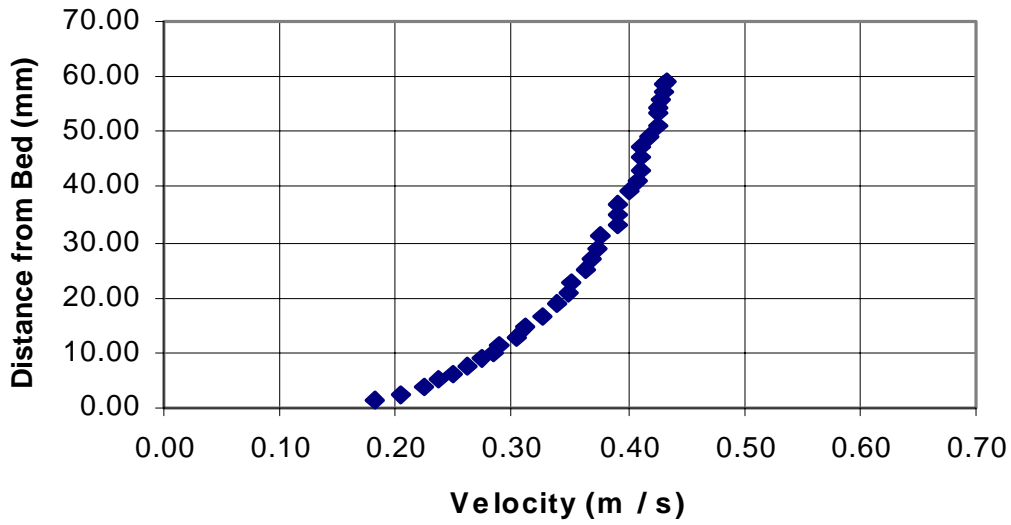


Figure A.7a Velocity profile for experiment G3 ($H/D_{50} = 8$ and $S = 0.115\%$). The datum is at the top of the balls in the channel bed.

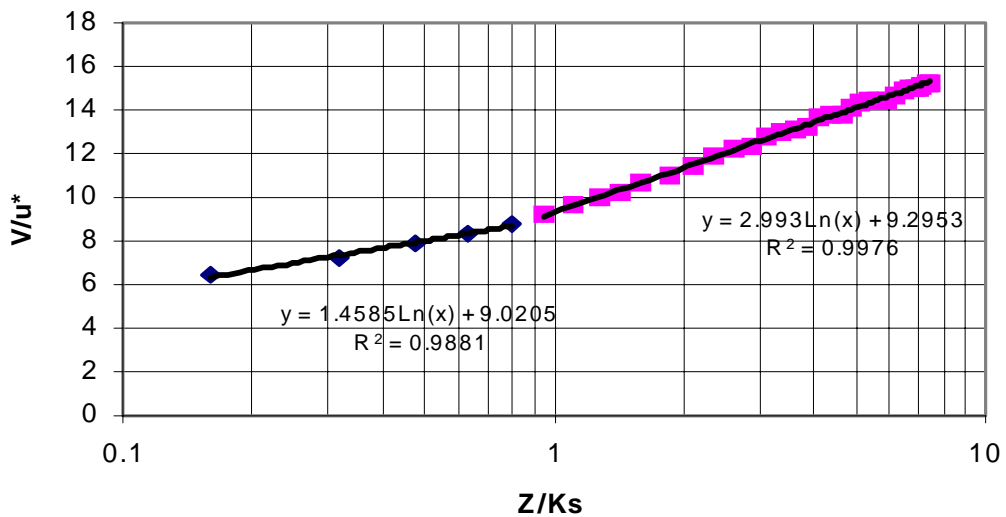


Figure A.7b Logarithmic velocity profile for experiment G3 ($H/D_{50} = 8$ and $S = 0.115\%$) split into two regions. The datum is at the top of the balls in the channel bed.

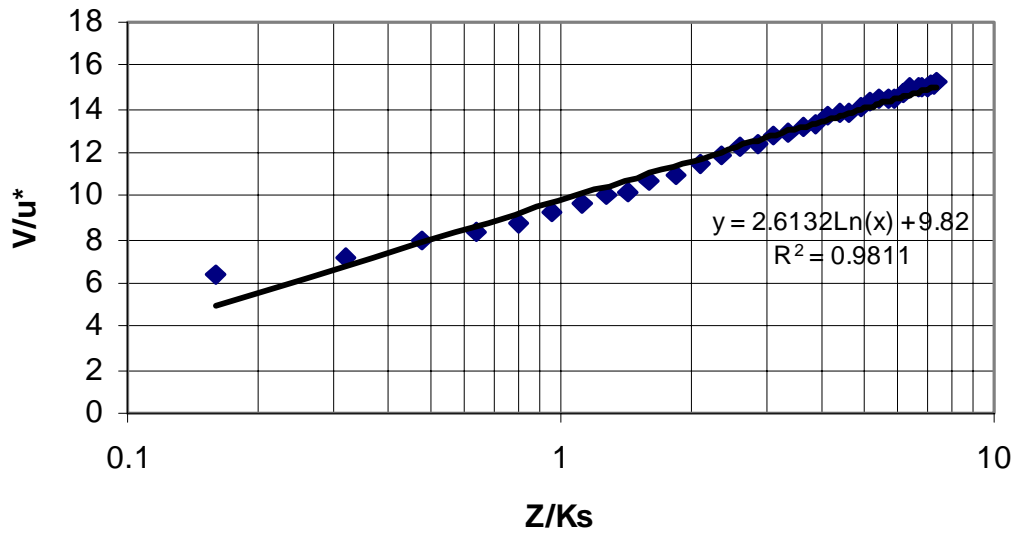


Figure A.7c Logarithmic velocity profile for experiment G3 ($H/D_{50} = 8$ and $S = 0.115\%$): single region. The datum is at the top of the balls in the channel bed.

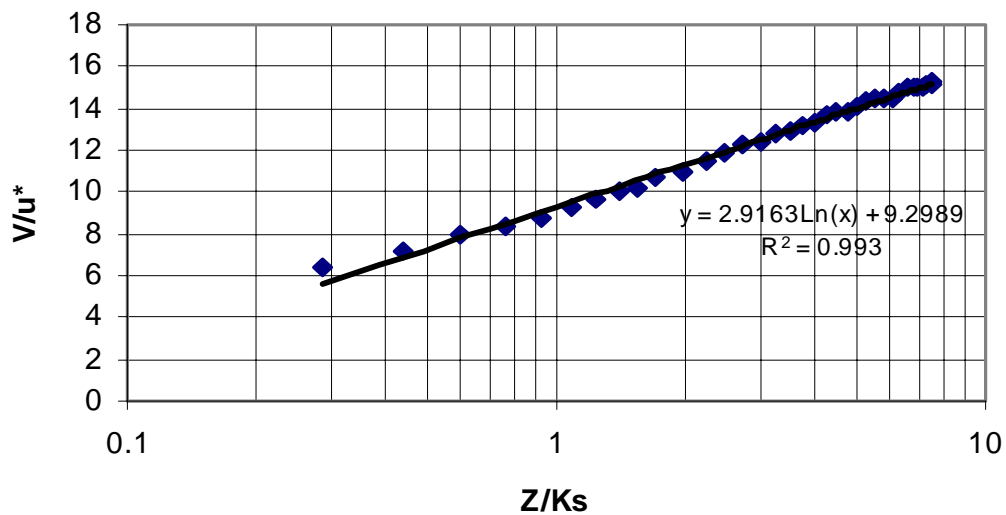


Figure A.7d Logarithmic velocity profile for experiment G3 ($H/D_{50} = 8$ and $S = 0.115\%$): single region. The datum is 1 mm below the top of the balls in the bed.

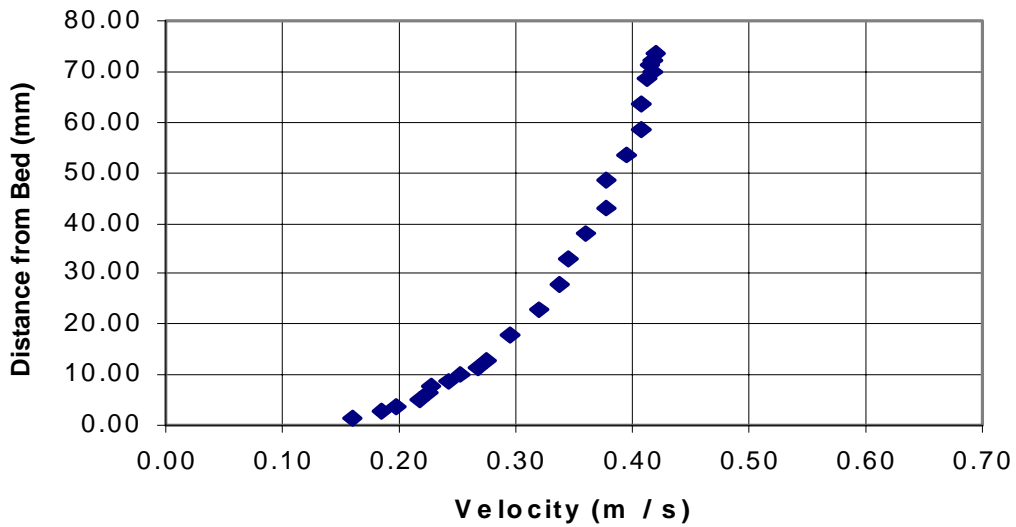


Figure A.8a Velocity profile for experiment H3 ($H/D_{50} = 10$ and $S = 0.09\%$). The datum is at the top of the balls in the channel bed.

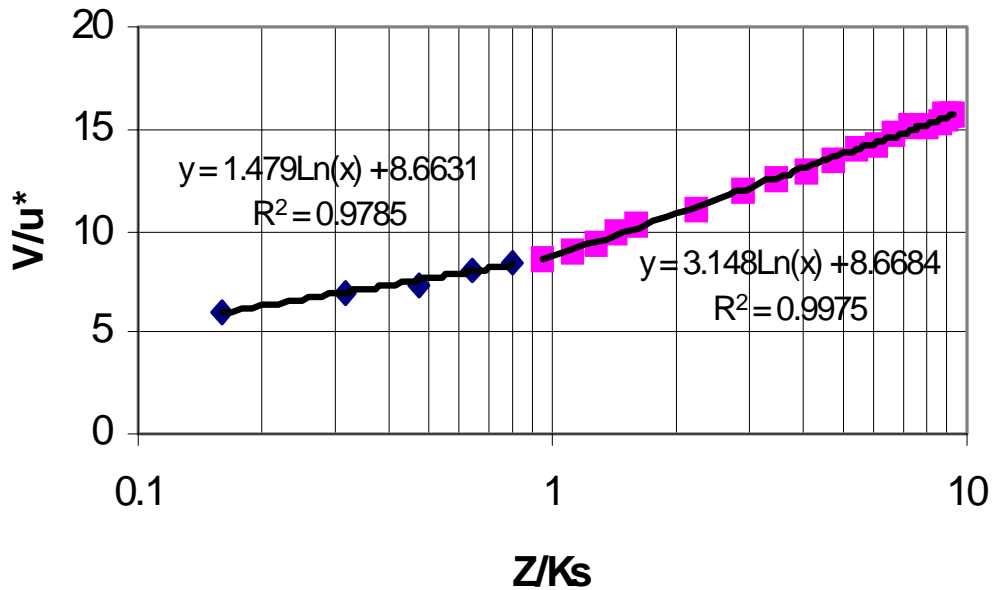


Figure A.8b Logarithmic velocity profile for experiment H3 ($H/D_{50} = 10$ and $S = 0.09\%$) split into two regions. The datum is at the top of the balls in the channel bed.

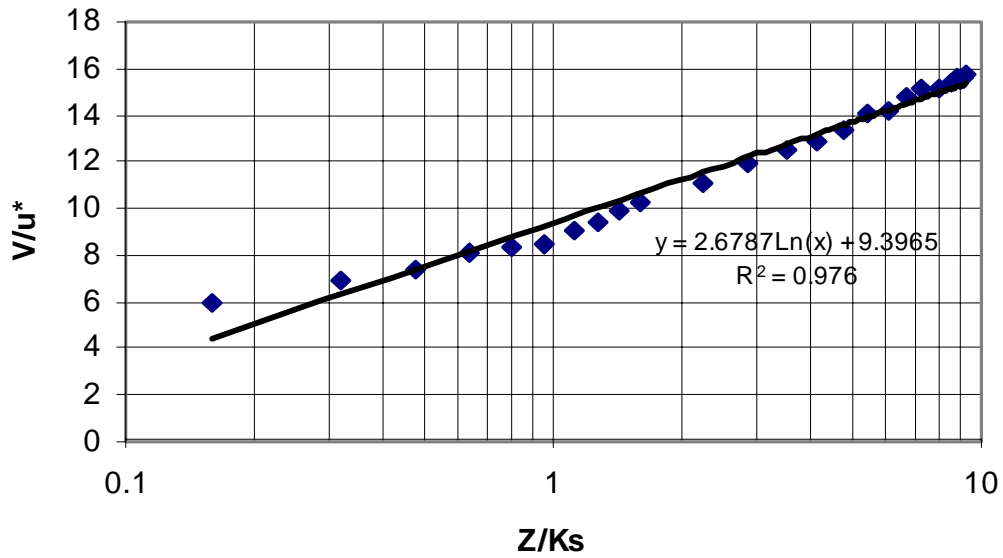


Figure A.8c Logarithmic velocity profile for experiment H3 ($H/D_{50} = 10$ and $S = 0.09\%$): single region. The datum is at the top of the balls in the channel bed.

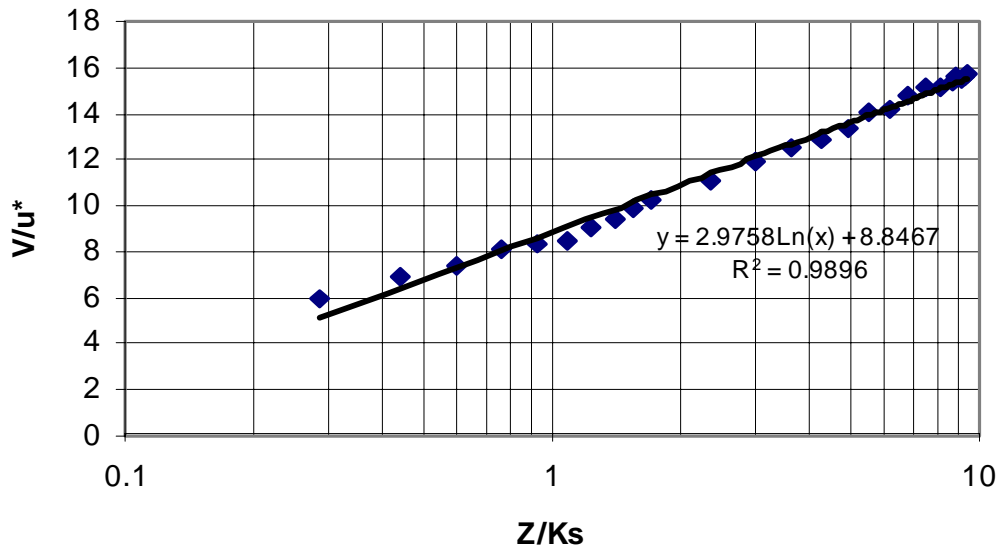


Figure A.8d Logarithmic velocity profile for experiment H3 ($H/D_{50} = 10$ and $S = 0.09\%$): single region. The datum is 1 mm below the top of the balls in the bed.

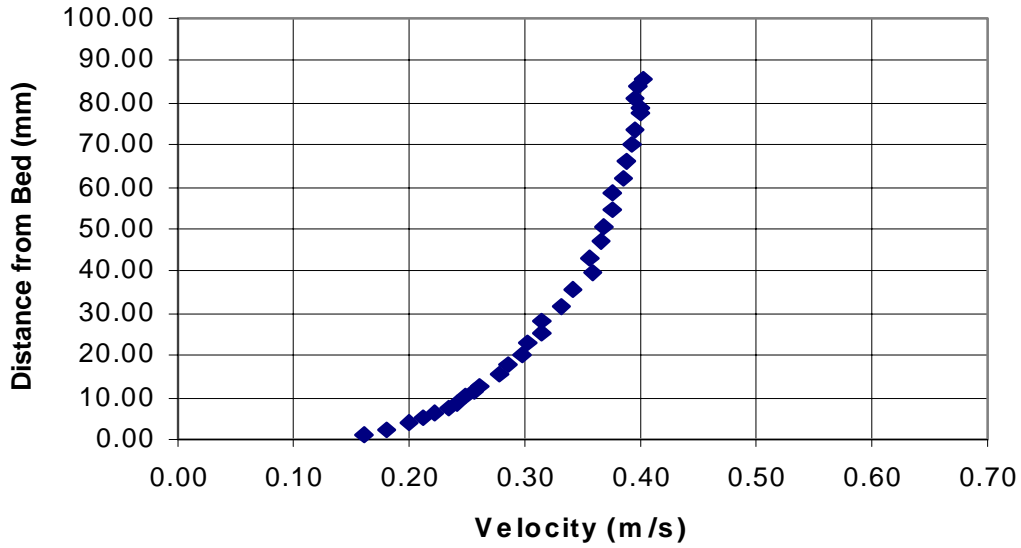


Figure A.9a Velocity profile for experiment I3 ($H/D_{50} = 12$ and $S = 0.075\%$). The datum is at the top of the balls in the channel bed.

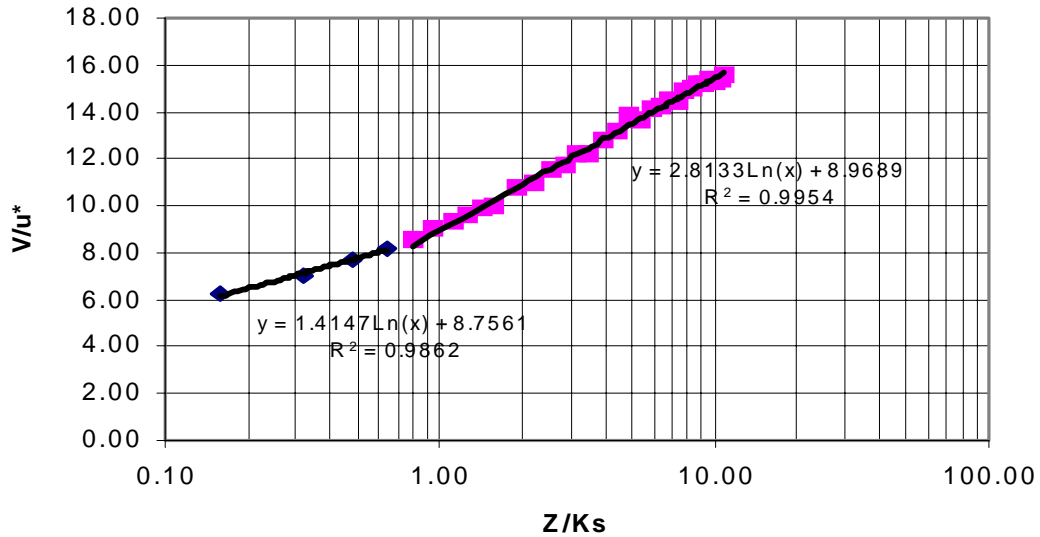


Figure A.9b Logarithmic velocity profile for experiment I3 ($H/D_{50} = 12$ and $S = 0.075\%$) split into two regions. The datum is at the top of the balls in the channel bed.

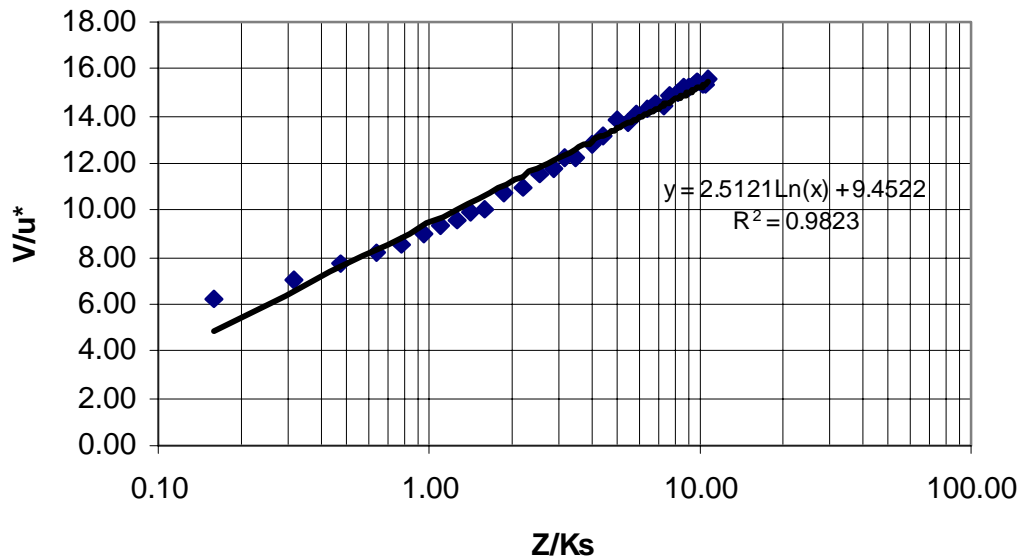


Figure A.9c Logarithmic velocity profile for experiment I3 ($H/D_{50} = 12$ and $S = 0.075\%$): single region. The datum is at the top of the balls in the channel bed.

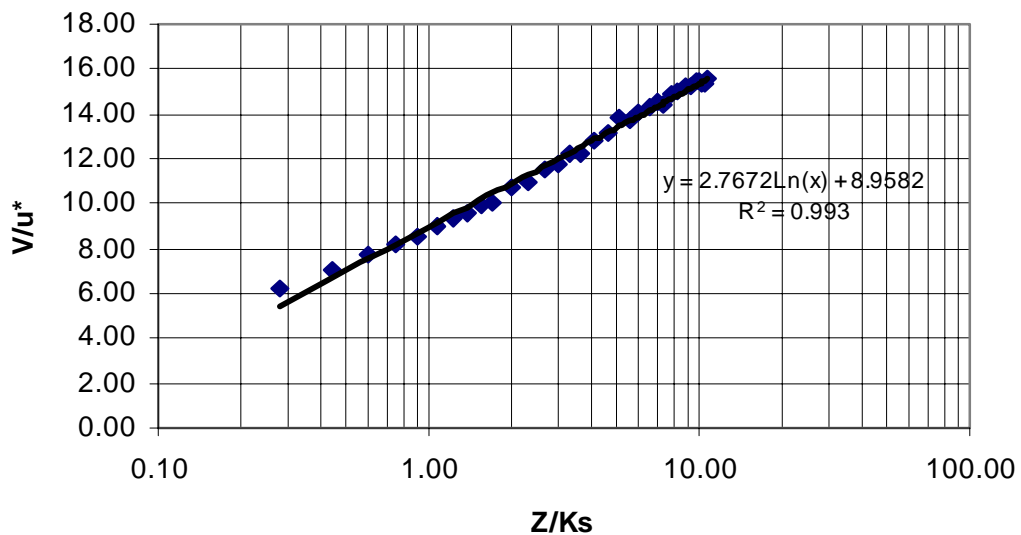


Figure A.9d Logarithmic velocity profile for experiment I3 ($H/D_{50} = 12$ and $S = 0.075\%$): single region. The datum is 1 mm below the top of the balls in the bed.

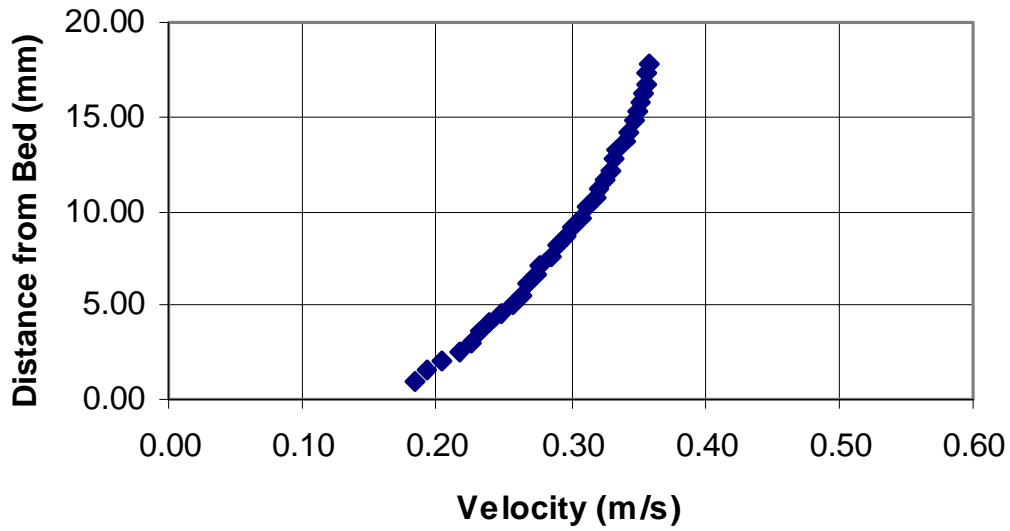


Figure A.10a Velocity profile for $H/D_{50} = 3$ and $S = 0.21\%$ (pressurized). The datum is at the top of the balls in the channel bed.

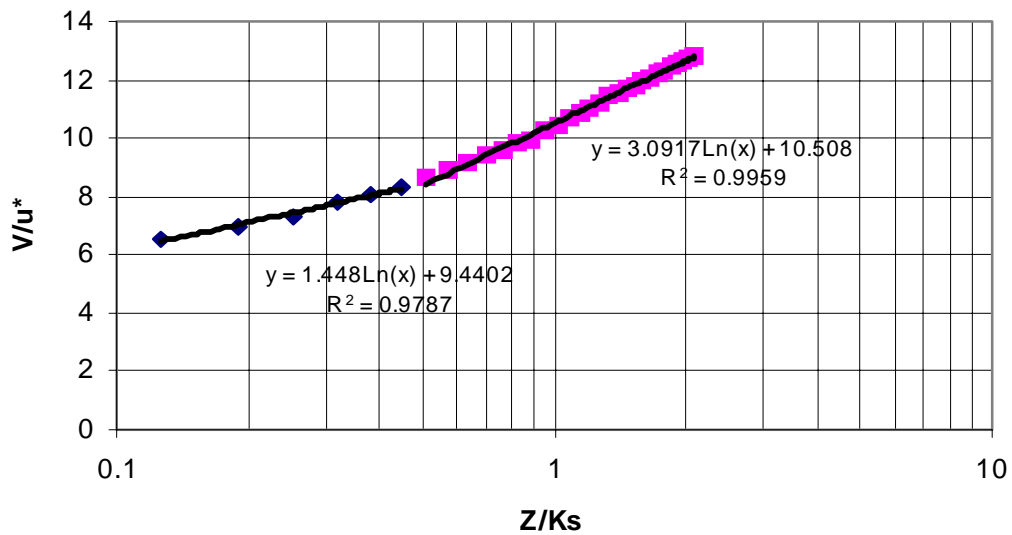


Figure A.10b Logarithmic velocity profile for $H/D_{50} = 3$ and $S = 0.21\%$ (pressurized) split into two regions. The datum is at the top of the balls in the channel bed.

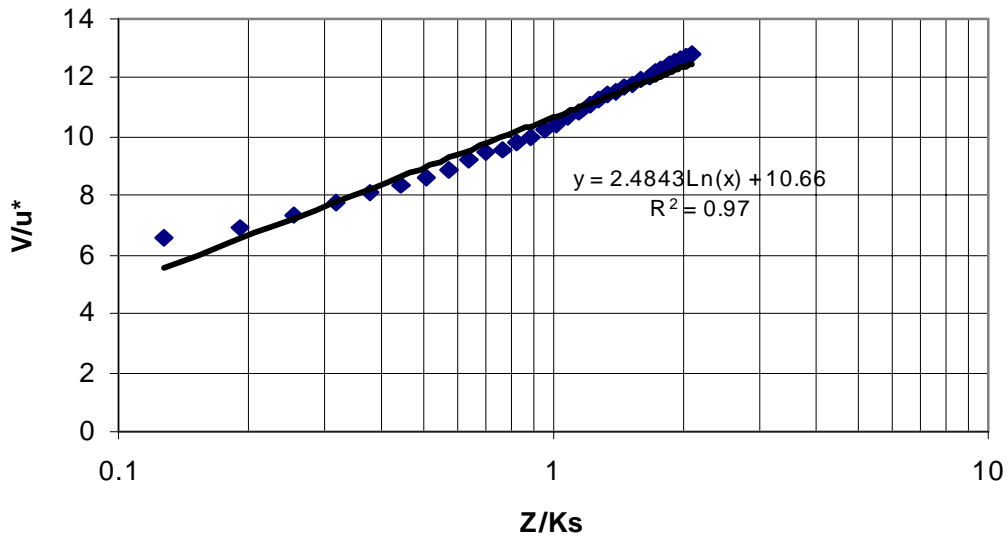


Figure A.10c Logarithmic velocity profile for $H/D_{50} = 3$ and $S = 0.21\%$ (pressurized): single region. The datum is at the top of the balls in the channel bed.

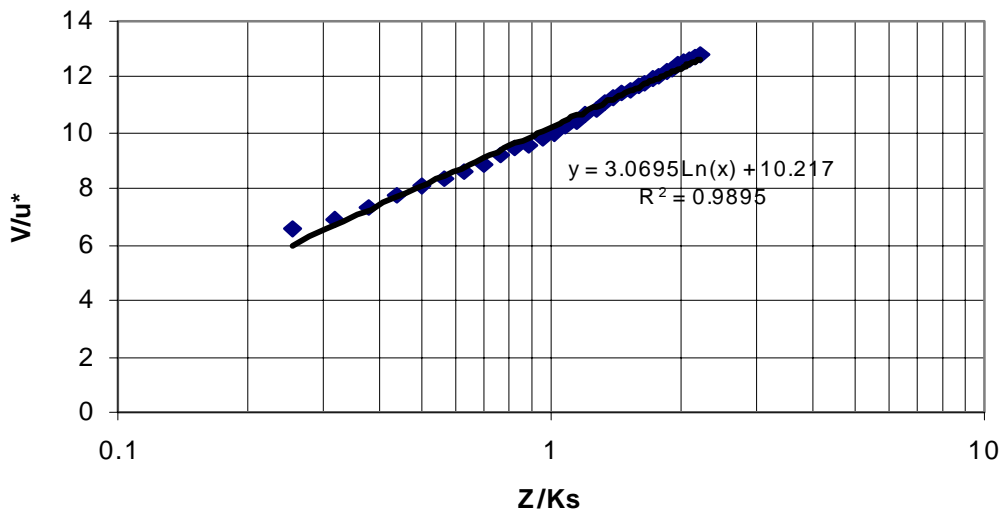


Figure A.10d Logarithmic velocity profile for $H/D_{50} = 3$ and $S = 0.21\%$ (pressurized): single region. The datum is 1 mm below the top of the balls in the bed.

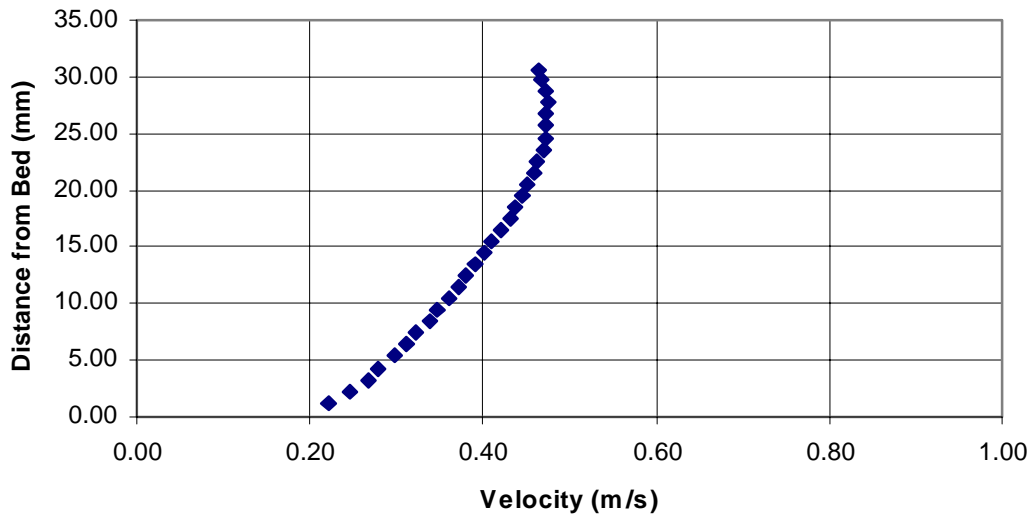


Figure A.11a Velocity profile for $H/D_{50} = 4.5$ and $S = 0.21\%$ (pressurized). The datum is at the top of the balls in the channel bed.

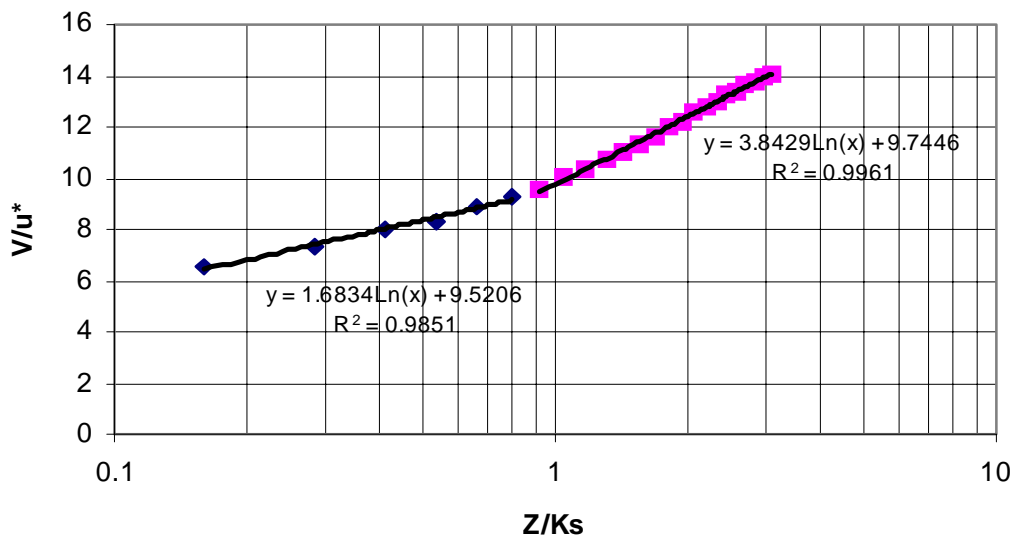


Figure A.11b Logarithmic velocity profile for $H/D_{50} = 4.5$ and $S = 0.21\%$ (pressurized) split into two regions. The datum is at the top of the balls in the bed.

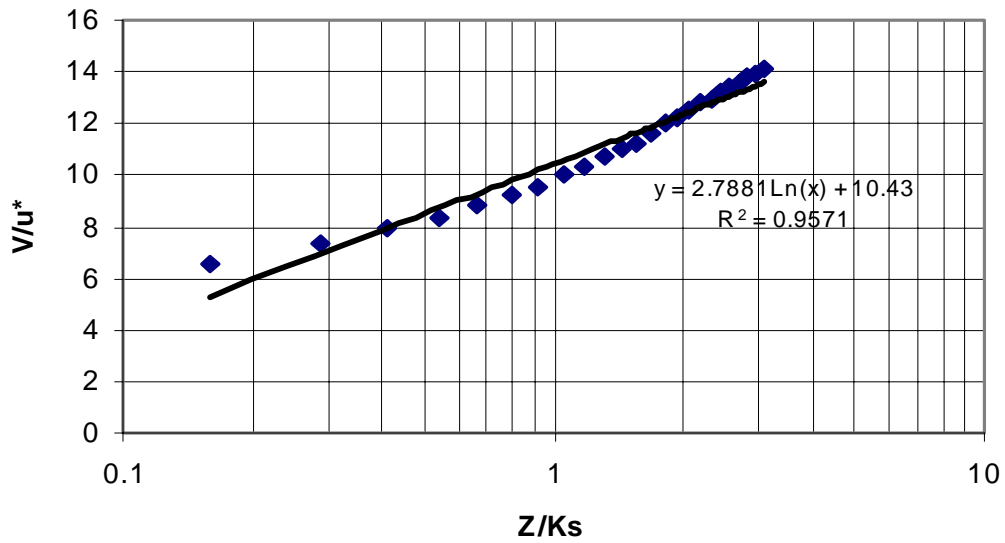


Figure A.11c Logarithmic velocity profile for $H/D_{50} = 4.5$ and $S = 0.21\%$ (pressurized): single region. The datum is at the top of the balls in the channel bed.

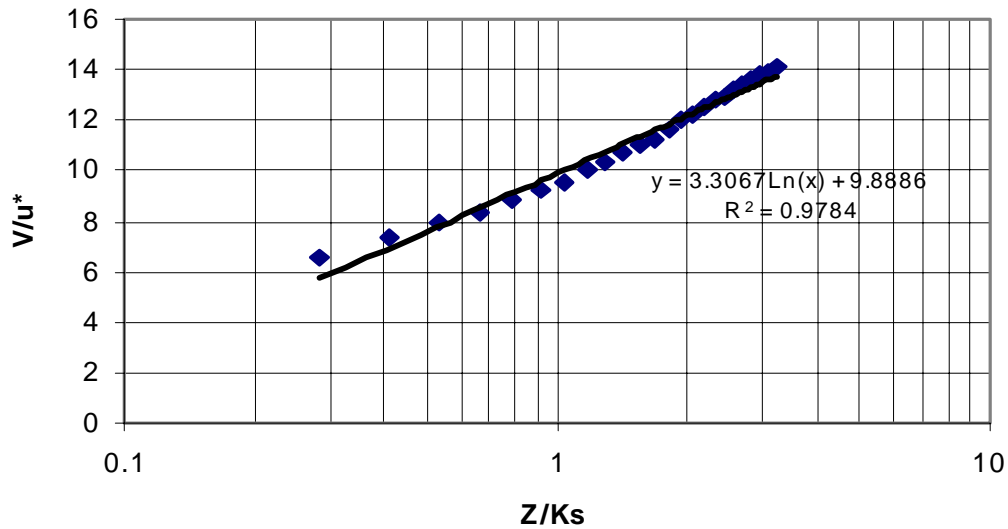


Figure A.11d Logarithmic velocity profile for $H/D_{50} = 4.5$ and $S = 0.21\%$ (pressurized): single region. The datum is 1 mm below the top of the balls in the bed.

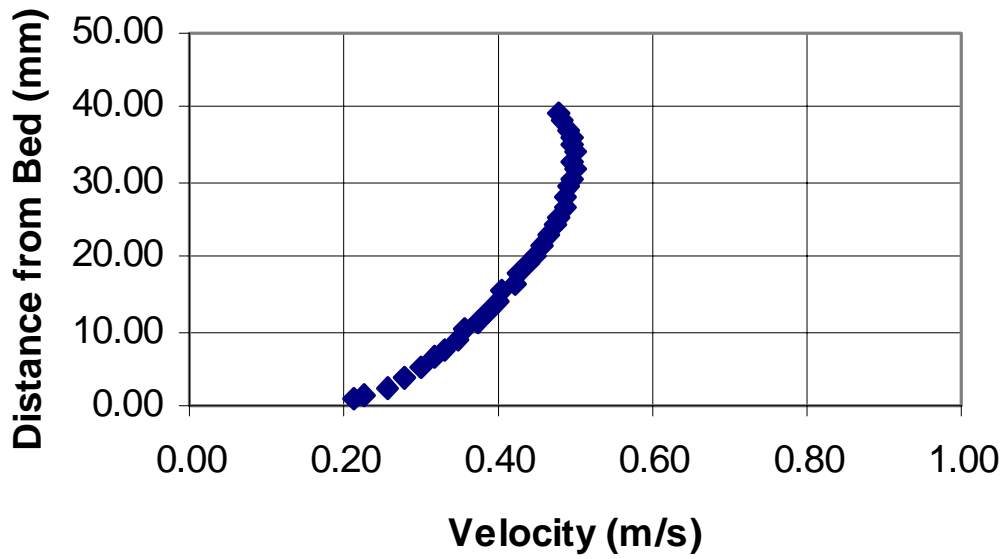


Figure A.12a Velocity profile for $H/D_{50} = 5.5$ and $S = 0.21\%$ (pressurized). The datum is at the top of the balls in the channel bed.

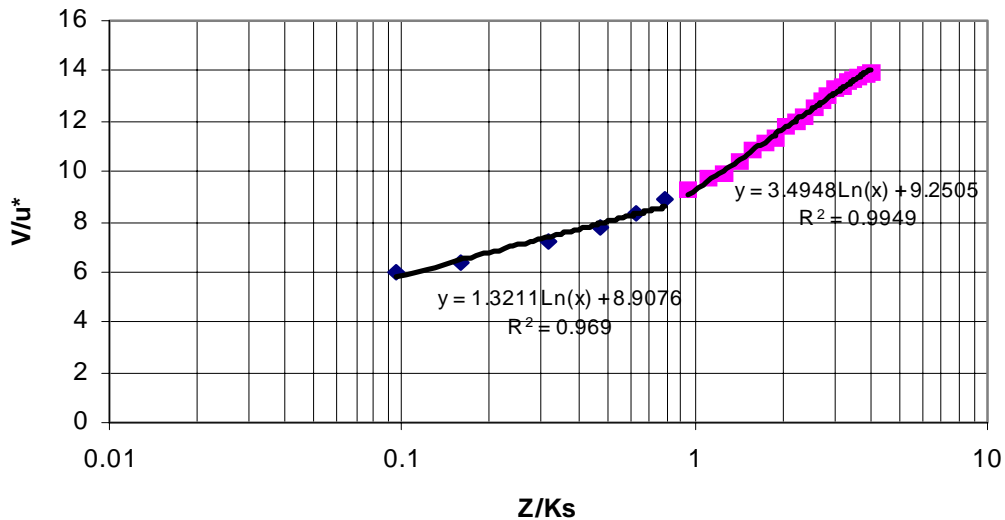


Figure A.12b Logarithmic velocity profile for $H/D_{50} = 5.5$ and $S = 0.21\%$ (pressurized) split into two regions. The datum is at the top of the balls in the bed.

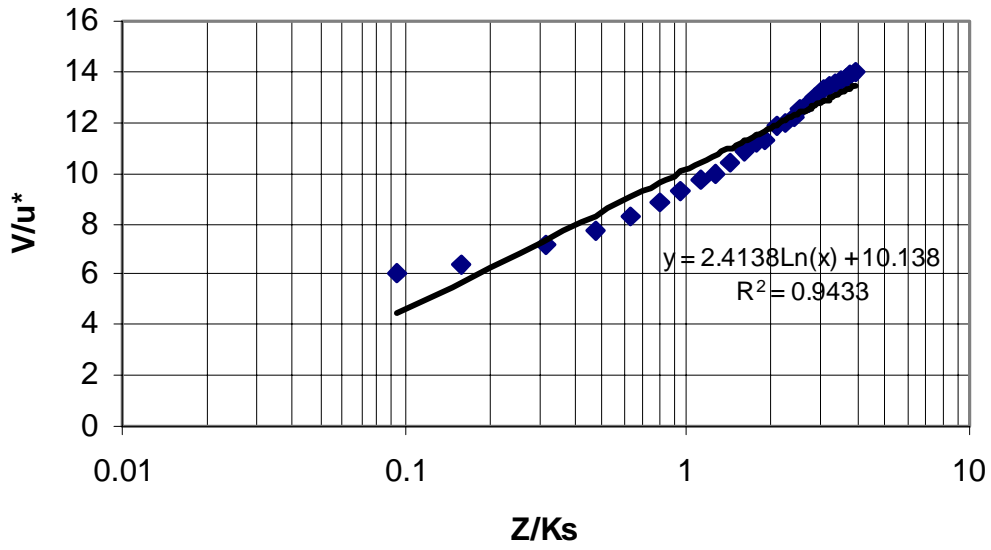


Figure A.12c Logarithmic velocity profile for $H/D_{50} = 5.5$ and $S = 0.21\%$ (pressurized): single region. The datum is at the top of the balls in the channel bed.

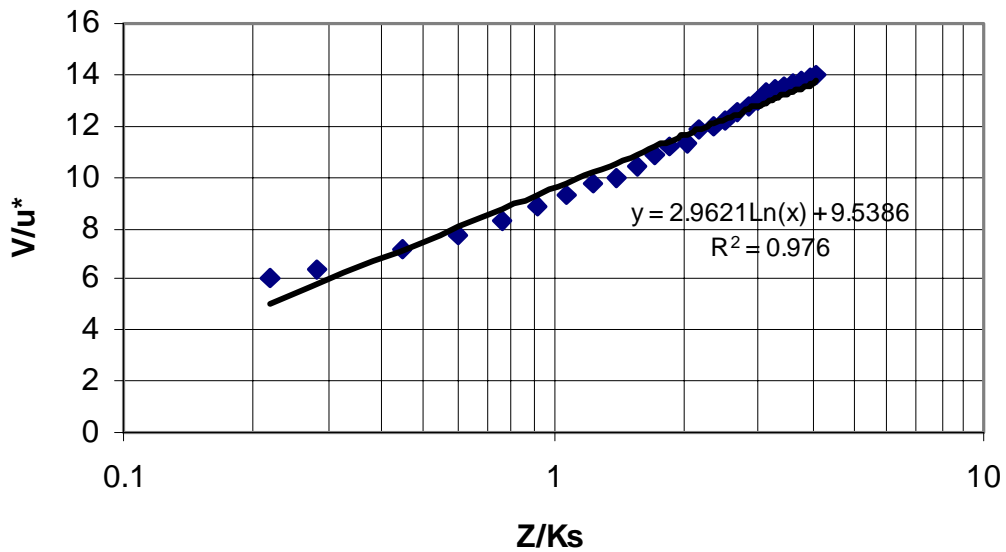


Figure A.12d Logarithmic velocity profile for $H/D_{50} = 5.5$ and $S = 0.21\%$ (pressurized): single region. The datum is 1 mm below the top of the balls in the bed.

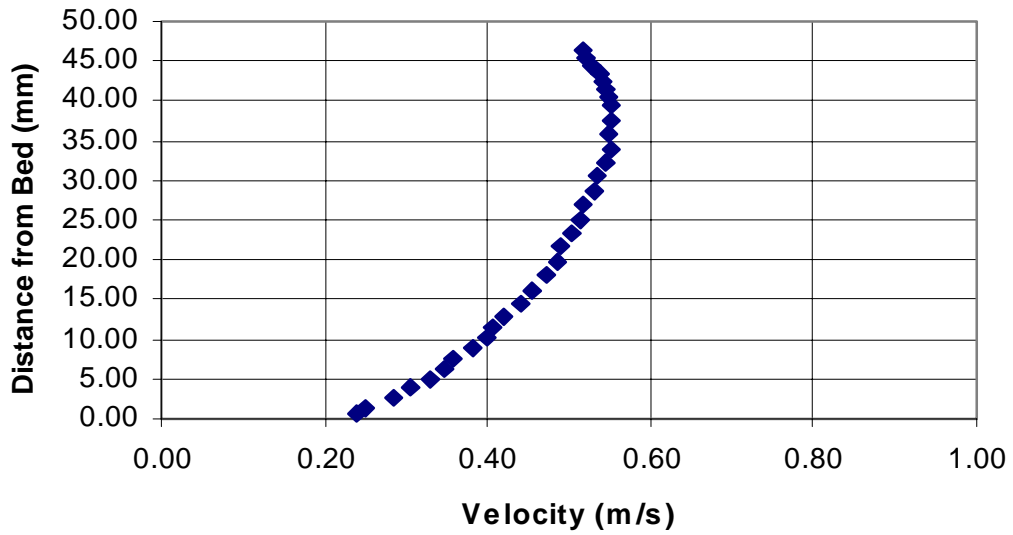


Figure A.13a Velocity profile for $H/D_{50} = 6.5$ and $S = 0.21\%$ (pressurized). The datum is at the top of the balls in the channel bed.

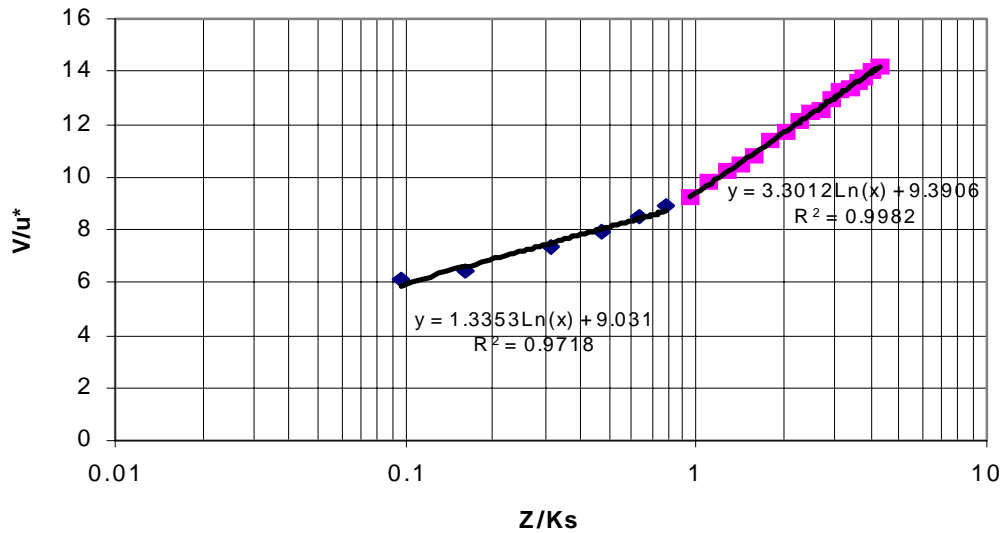


Figure A.13b Logarithmic velocity profile for $H/D_{50} = 6.5$ and $S = 0.21\%$ (pressurized) split into two regions. The datum is at the top of the balls in the bed.

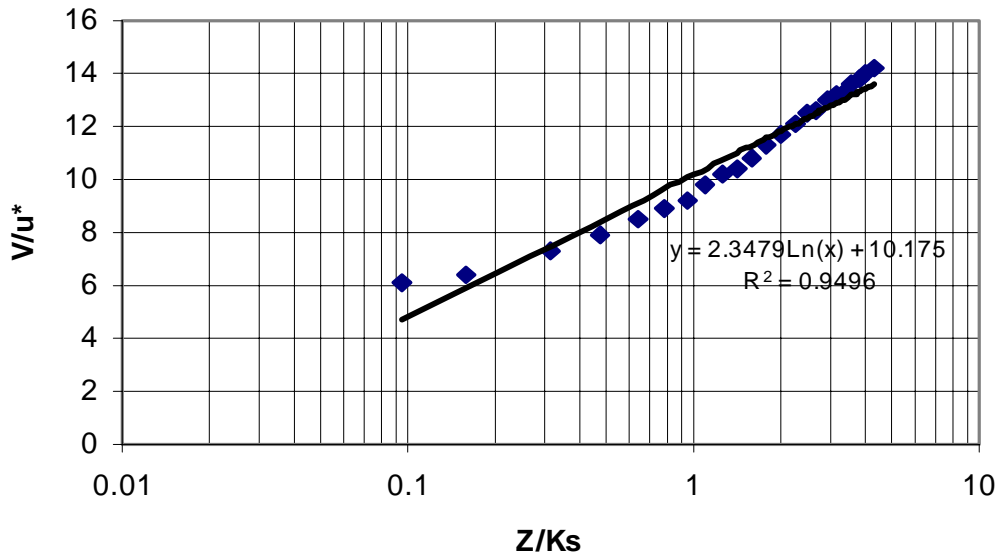


Figure A.13c Logarithmic velocity profile for $H/D_{50} = 6.5$ and $S = 0.21\%$ (pressurized): single region. The datum is at the top of the balls in the channel bed.

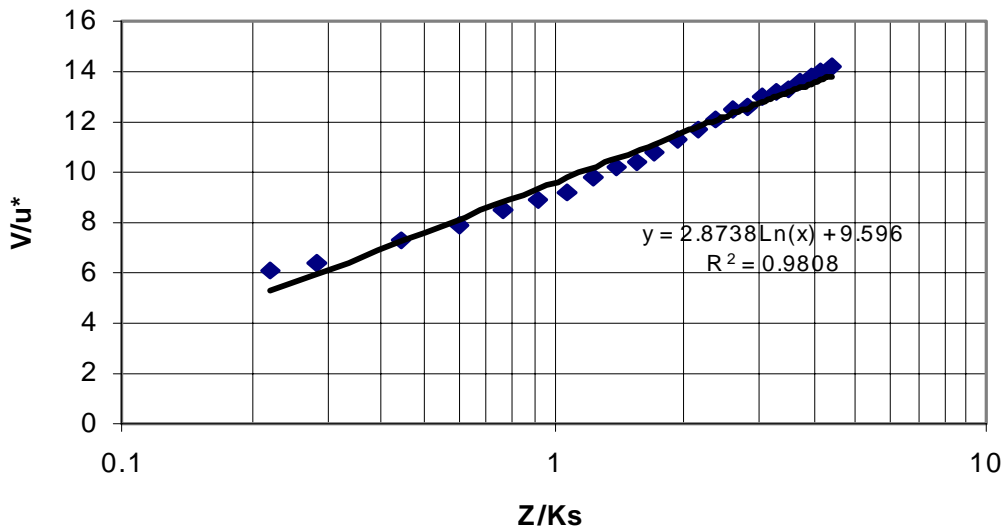


Figure A.13d Logarithmic velocity profile for $H/D_{50} = 6.5$ and $S = 0.21\%$ (pressurized): single region. The datum is 1 mm below the top of the balls in the bed.

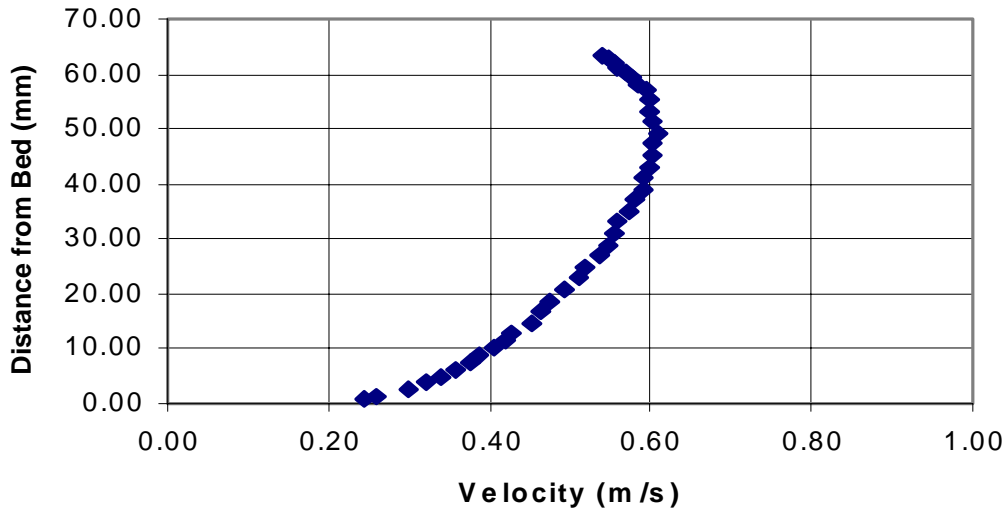


Figure A.14a Velocity profile for $H/D_{50} = 8.5$ and $S = 0.21\%$ (pressurized). The datum is at the top of the balls in the channel bed.

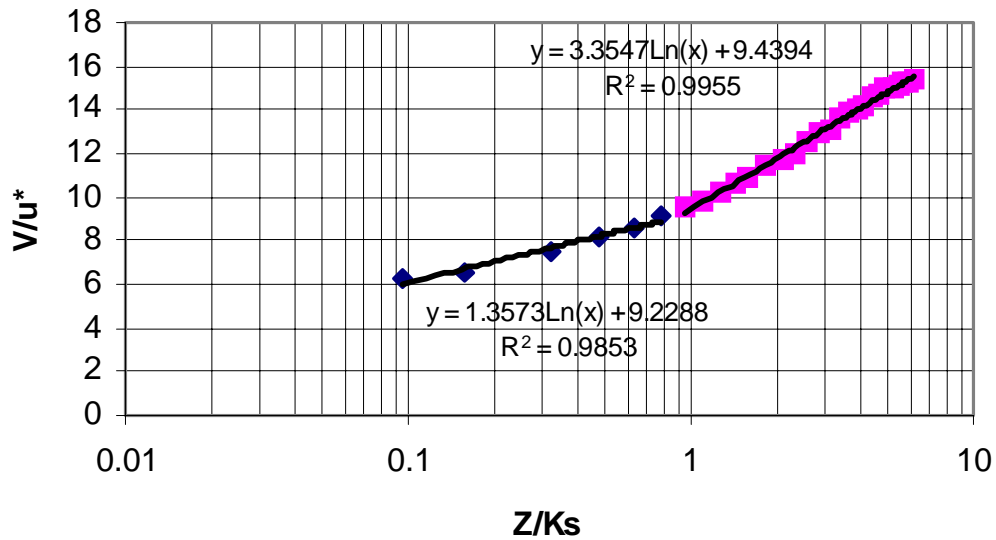


Figure A.14b Logarithmic velocity profile for $H/D_{50} = 8.5$ and $S = 0.21\%$ (pressurized) split into two regions. The datum is at the top of the balls in the bed.

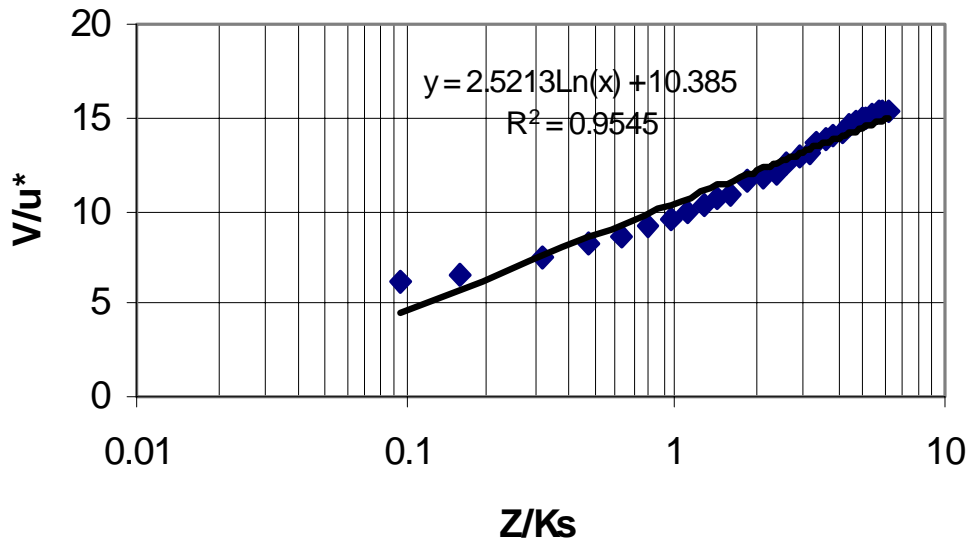


Figure A.14c Logarithmic velocity profile for $H/D_{50} = 8.5$ and $S = 0.21\%$ (pressurized): single region. The datum is at the top of the balls in the channel bed.

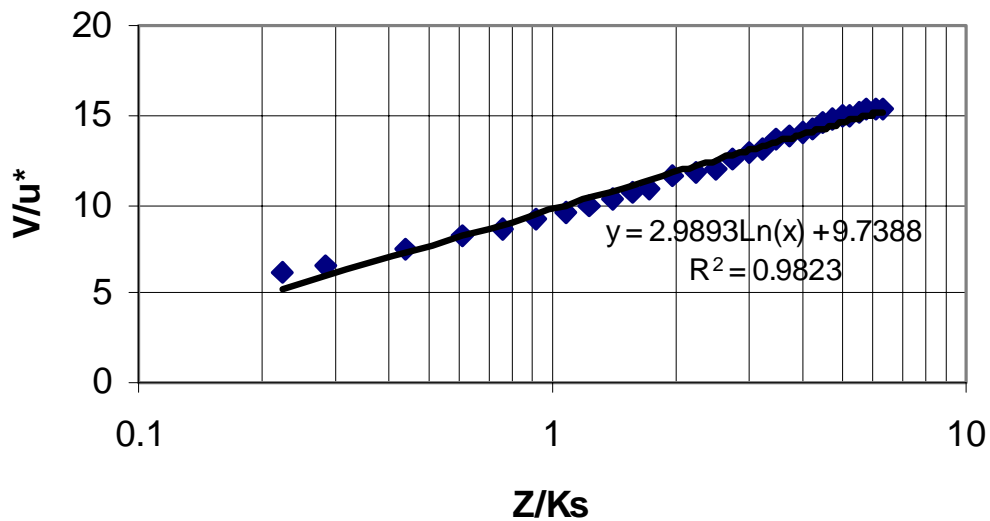


Figure A.14d Logarithmic velocity profile for $H/D_{50} = 8.5$ and $S = 0.21\%$ (pressurized): single region. The datum is 1 mm below the top of the balls in the bed.

Vita

Paul M. Kanellopoulos was born on December 15, 1972 near Chicago, Illinois and was raised in Caracas, Venezuela. He graduated from the Virginia Polytechnic Institute and State University in 1996 with a Bachelor of Science in civil engineering. In 1998 he received his Master of Science in civil engineering from the same university. He is interested in the design of storm sewers, flood control, stable channel design, reservoir restoration and management, and the design of small dams.